Charge Carrier Dynamics
in Thin Film Solar Cells

Christian Strothkämper

2013

Diese Arbeit entstand am Helmholtz-Zentrum Berlin für Materialien und Energie, größtenteils im Institut E-I5 unter Leitung von Prof. Dr. Thomas Hannappel.

1 Introduction

The harvesting of solar energy by use of photovoltaics (PV) is continuously attracting the interest of researchers worldwide. This may on the one hand be due to the richness of physical processes involved in many PV technologies. On the other hand, the importance of PV goes much beyond a merely academic interest. Research in PV is routinely motivated by its potentially huge significance for modern society. PV bears a huge potential for decentralized power generation and becomes increasingly appealing economically because of the growing return of investment. Ecologically, the importance of PV roots in its sustainability: The demand for photovoltaics is growing because unlike oil, gas, coal, or uranium solar energy is practically unlimited. Moreover, regarding the debate on manmade global warming, PV is free of carbon dioxide emissions during operation. The warming 'greenhouse gas' effect of atmospheric CO_2 has been described by Arrhenius over 100 years ago.[1] Man-made global warming is currently regarded as a negative effect[I] and means of avoiding the dramatic increase of atmospheric CO_2 (Keeling curve), which is a cause of huge concern, are under constant debate. Hence, low CO_2 emission technologies such as PV may be an important part of the solution to this problem.

Except for its ecological and economic significance, PV offers the scientist a wide variety of interesting physics. The different technological approaches of second (thin film) and third (thin film, high efficiency) generation photovoltaics cover a broad range of topics in nano-, surface- and interface physics and include very advanced concepts, such as multiple exciton generation and hot carrier cells. The dynamics of charge carriers, i.e. transport, energetic relaxation and recombination, are the fundamental processes in every photovoltaic device. Optical-pump terahertz-probe (OPTP) spectroscopy, which allows for measuring the photoconductivity with a sub-ps time resolution, has turned out to be a very suitable technique to study these processes. Despite being a new technique, OPTP has gained much interest in the PV communities worldwide, and is at the very heart of this thesis. When necessary, other spectroscopic techniques like transient absorp-

---

[I] Amusingly, Arrhenius' notion about manmade global warming through carbon dioxide emissions was completely different from the present consensus:[2]

"We often hear lamentations that the coal stored up in the earth is wasted by the present generation without any thought of the future, and we are terrified by the awful destruction of life and property which has followed the volcanic eruptions of our days. We may find a kind of consolation in the consideration that here, as in every other case, there is good mixed with the evil. By the influence of the increasing percentage of carbonic acid in the atmosphere, we may hope to enjoy ages with more equable and better climates, especially as regards the colder regions of the earth, ages when the earth will bring forth much more abundant crops than at present, for the benefit of rapidly propagating mankind."

tion (TA) and two-photon photoemission (2PPE) were used to complement the insights obtained from OPTP.

The thesis is organized in the following scheme: In chapter 2, theoretical aspects necessary for the interpretation of the measurements are presented. Chapter 3 details the experimental setups used in the present thesis. In the following three chapters 4-6, the charge carrier dynamics results obtained with these techniques on three different thin-film solar cell technologies are presented and discussed:

I Chapter 4 of this thesis will focus on electrode-core/absorber-shell nanorods. These materials belong to a class of thin film photovoltaics that is commonly referred to as semiconductor-sensitized solar cells (SSSC) or extremely thin absorber (ETA) cells. The idea behind this approach is to effectively separate the optical absorption length from the charge carrier diffusion length. For this purpose, the absorber is not deposited as a planar thin film but rather applied onto a nanostructured electrode, such as TiO_2 nanoparticles[3] or ZnO nanorods.[4] In that sense, this architecture allows using low-quality (i.e. low diffusion lengths) absorber materials, which could in principle be low-cost.

The material under study here are ZnO/In_2S_3 core/shell nanorods. Solar cells based on these radial heterojunctions (RHJ) have recently shown promising solar conversion efficiencies.[4] Key processes that determine the device behavior are charge carrier relaxation and separation following photo-excitation. OPTP spectroscopy is employed examining samples with systematically varied local absorber thicknesses. To evaluate the OPTP data quantitatively and to estimate injection yields the Bruggemann effective medium approach is extended to cylindrical core-shell structures. A peculiarly slow charge separation is observed which can be explained on the basis of multiple trapping (MT) transport.

II Dye-sensitized-solar cells (DSCs) bear the potential for low-cost and efficient thin film solar cells. Solar light absorbing dyes are chemisorbed to a semiconductor surface. Inspired by the famous Grätzel cell,[5] most studies in the past have focused on Ruthenium-based metal-organic dyes and TiO_2 colloidal electrodes. However, metal-free dyes and electrode materials with higher mobilities or optimized geometries have potential benefits. The system investigated in chapter 5 comprises ZnO nanorods with metal-free model perylene dyes. Due to the practically unlimited supply of hydrocarbons purely organic dyes do not suffer from the abundance constraint of Ru based dyes. Additionally, the synthesis of the organic dyes may imply a significant price advantage compared to metal-organic complexes. ZnO nanorods are intensively studied as future electron acceptors and electrode materials in hybrid organic-inorganic solar cells. ZnO has a higher bulk mobility than TiO_2 and can easily be grown as well-aligned and crystalline nanorods with direct contact to the back electrode. In theory, this should facilitate the collection of photogener-

ated carriers compared to the randomly organized percolation networks in colloidal TiO_2 structures.

However, ZnO has so far shown inferior performance over e.g. TiO_2 electrodes. In chapter 5, a peculiarity about the injection mechanism in ZnO/dye-molecule hybrid systems is clarified: the delayed formation of free electrons. This can lead to losses connected to low injection efficiencies and higher recombination rates. In a broader context, unraveling this delay mechanism is also of great significance in (photo-) electrochemistry and catalysis. To unveil the delay physics, a joint spectroscopic approach with TA, OPTP and 2PPE is employed on a series of five model dyes which consist of the same perylene chromophore and carboxylic anchor group, but differ by the systematically extended bridge unit. In this way, the influence of the Coulomb attraction between the cation and the injected electron on the injection process can be evaluated.

III Solar cells based on thin film chalcopyrite semiconductors are a promising technology that has already entered the stage of mass production. The best cells are based on $CuInSe_2$ (CIS) which for optimization is alloyed with Ga (located on the In sublattice) and grown with a slightly Cu deficient composition. The 20.3 % efficiency record for $Cu(In,Ga)Se_2$ (CIGS) based solar cells[6] is outstanding for thin film solar cells. Significant progress in CIGS technology has been achieved by trial and error rather than by 'knowledge-based technological design'.[7] For the latter purpose, a good knowledge of the material properties such as the transport and recombination physics is a prerequisite. It is shown in chapter 6, that the understanding of these processes in CIS can be enhanced by means of OPTP.

Until now, only limited understanding could be gathered concerning the detrimental effects which narrow the efficiency when the absorber is grown with a stoichiometric instead of a Cu-poor composition. The superiority of the Cu-poor material is surprising, since it has an extraordinary high defect density on the order of several $10^{20}\,cm^{-3}$ with many of the defects being electrically charged. Here, OPTP is used to gain new insights into the recombination of photocarriers and to reveal the impact of deviation from stoichiometry on the charge carrier lifetime. Also OPTP allows determining the momentum relaxation time (MRT) and it is concluded to what extent grain boundary and bulk scattering processes limit the mobility. A special point of interest is the question how the charge carrier transport is altered in the solar cell grade Cu-poor CIS. Can the transport in this highly defective material still be described in the picture of free electrons whose motions is hindered by scattering

2 Theoretical Background

This chapter presents a general background on theoretical aspects that are necessary for the understanding of the work in this thesis. It starts by briefly presenting light-matter interaction in the framework of continuum electrodynamics, introducing important quantities such as the conductivity or the permittivity, which are relevant for the understanding of photonic pump-probe experiments such as TA or OPTP. Thereafter, the scattering of charge carriers, which is the major limitation of charge transport, is reviewed. It is detailed how this scattering influences the mobility a fundamental quantity of charge carrier transport. The chapter ends with a brief assessment of the interaction of molecular adsorbates with semiconductor electrodes, focusing on the electron transfer reaction, which is the basic mechanism of the DSC.

2.1 Probing Charge Carrier Dynamics

In vacuum the propagation of light is fully described by Maxwell's equations. In matter this description needs to be modified because of the interaction of the electromagnetic wave with the charges in the material. An isolated metal or semiconductor usually displays no macroscopic electromagnetic field. However, if an electromagnetic field acts on the material, microscopic dipole moments are induced which are the source of a macroscopic electric field. The density of the induced dipole moments is called the polarization $\mathbf{P}$ and it is proportional to the total macroscopic electric field $\mathbf{E}$, i.e. to the applied and the induced electric field[8]

$$\mathbf{P}(\omega) = \epsilon_0 (\epsilon_r(\omega) - 1)\mathbf{E}(\omega). \tag{2.1}$$

Here, $\epsilon_0 \approx 8.854 \cdot 10^{12}\,\mathrm{Fm}^{-1}$ is the vacuum permittivity and ϵ_r is a material parameter known as the relative permittivity.[I] The role of the permittivity for the description of light-matter interaction gets clear by regarding the basic solution of Maxwell's equations for the electric field in homogenous media[8]

$$\mathbf{E} = \mathbf{E}_0 e^{i(n\mathbf{k}_0\mathbf{r} - \omega t)} e^{-\kappa \mathbf{k}_0 \mathbf{r}}. \tag{2.2}$$

The speed of light in matter is reduced by the real part of the complex refractive index $n + i\kappa \equiv \sqrt{\epsilon_r \mu_r}$. In addition electromagnetic waves are attenuated which is described by the imaginary part κ of the refractive index: Eq. (2.2) states that the intensity decays on a length scale

---

[I] In the special case of an isotropic medium, which is adopted here for simplicity, ϵ_r is a scalar. In the general case of an anisotropic medium such as many crystals, ϵ_r is a matrix.

$\lambda / (4\pi\kappa)$. In many materials $\mu_r \approx 1$, and the refractive index is determined by the permittivity alone. Thus the propagation of light through (excited) media then allows drawing conclusions on (changes of) the permittivity. For example it is detailed in section 3.2 how the increase of a semi-conductors' conductivity by absorbed photons (the photoconductivity) can be measured by OPTP spectroscopy.

To gain knowledge about the microscopic charge carrier dynamics, it is necessary to know how these enter the permittivity, or equivalently the conductivity $\sigma = -i\omega\varepsilon_0 (\varepsilon_r - 1)$. The conductivity bears the same amount of information as the permittivity but is more convenient with regard to charge transport as it directly relates the electric current density $\mathbf{j}$ with the electric field

$$\mathbf{j} = \sigma \cdot \mathbf{E}. \tag{2.3}$$

An easy access to the microscopic origin of the conductivity can be achieved by a classical description of the charge carriers. The equation of motion for a charged particle under the influence of an electric field $\mathbf{E}$ is[9]

$$m\frac{\partial^2}{\partial t^2}\mathbf{r} + m\Gamma\frac{\partial}{\partial t}\mathbf{r} + m\omega_0^2\mathbf{r} = q\mathbf{E} \tag{2.4}$$

In the context of classical mechanics the second term on the lhs is a phenomenological friction force and the third term is a restoring force. In the harmonic approximation ω_0 is the eigenfrequency of the bound electron and $\hbar\omega_0$ corresponds to the spacing of the quantum mechanical energy eigenvalues. To describe free charge carriers ω_0 can be set to zero later. Eq. (2.4) is directly solved by applying a Fourier transformation[II] and yields

$$\mathbf{r} = \frac{q/m}{\omega_0^2 - \omega^2 - i\Gamma\omega}\mathbf{E}(\omega). \tag{2.5}$$

The electric current density $\mathbf{j} = qn\dot{\mathbf{r}}$ depends on the density n of charge carriers, their charge q, and their velocity $\dot{\mathbf{r}}$. Hence, it follows from eqs. (2.3) and (2.5) that the conductivity reads

$$\sigma = -i\omega\frac{nq^2/m}{\omega_0^2 - \omega^2 - i\Gamma\omega}. \tag{2.6}$$

The case of a vanishing restoring force ($\omega_0 = 0$) describes free charge carriers. Then the conductivity takes a form which is known as the Drude conductivity

$$\sigma = \frac{nq^2\tau}{m}\cdot\frac{1}{1-i\omega\tau} \tag{2.7}$$

with $\tau = 1/\Gamma$. Conductivity spectra of bound and free charge carriers are depicted in Figure 2-1. Above the resonance frequency ω_0 the frequency dependence of the bound spectrum is reminis-

---

[II] Throughout the thesis the physical convention $\int \mathrm{d}t\, e^{i\omega t}$ of the Fourier transformation is adopted.

cent to that of free carriers. Below the resonance frequency, the photon energy deceeds the excitation energy of the bound electron. In this case the progression of the spectrum motivates why it is generally regarded as a sign of carrier localization when the real part of the conductivity increases with frequency and the imaginary part is negative.[10]
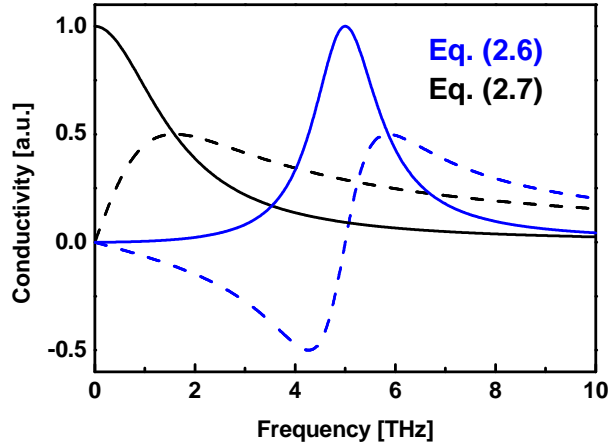
Figure 2-1 Real (solid) and imaginary (broken) part of the conductivity spectra of bound (blue) and free (black) charge carriers, plotted with $\Gamma = 100\,\mathrm{fs}^{-1}$ and $\omega_0 \,/\, 2\pi = 5\,\mathrm{THz}$.

The meaning of the parameter τ, which controls the friction of the electrons, becomes clear when the Drude conductivity is transformed back into the time domain and the action of an electric pulse $E_0 \delta(t)$ is regarded:[11] The created current which is proportional to the carrier momentum decays as $\mathbf{j}(t) = \mathbf{j}_0 \cdot e^{-t/\tau}$. Hence, τ is known as the momentum relaxation time and its microscopic origin is the scattering of electrons with e.g. lattice vibrations or lattice defects. A more detailed description of the conductivity which includes quantum effects and allows for a modeling of the microscopic charge carrier scattering is presented in section 2.2. It turns out that eq. (2.7) remains essentially unchanged when the mass m is replaced by the effective band mass m^*.

The conductivity describes the ability of the electron ensemble to carry a current. However, often one is rather interested in how much a single electron (on average) can contribute to the current. Expressing the current density $\mathbf{j} = nq\langle \mathbf{v}_D \rangle = \sigma \mathbf{E}$ in terms of the mean electron drift velocity $\langle \mathbf{v}_D \rangle$ yields for the conductivity

$$\sigma = nq\frac{\langle \mathbf{v}_D \rangle \mathbf{E}}{E^2} =: nq\mu. \tag{2.8}$$

The dependence of the drift velocity on the electric field and equivalently the conductivity normalized by the charge density defines the charge carrier mobility $\mu = v_D \,/\, E$. It will be shown in section 2.2.3 how the mobility can be calculated from the Boltzmann transport equation.

2.2 Charge Transport in Crystals

The electronic states in the periodic potential of an idealized crystal are Bloch functions, which (omitting the band index) can be written as $|\mathbf{k}\rangle = u_{\mathbf{k}}(\mathbf{r}) e^{i\mathbf{kr}}$, where $\mathbf{k}$ lies in the first Brillouin zone (FBZ) and $u_{\mathbf{k}}(\mathbf{r})$ has the same periodicity as the direct lattice. Any real crystal does not have a perfectly periodic potential because of chemical or compositional defects and thermal fluctuations of the lattice (phonons). These intrinsic perturbations lead to transitions between Bloch states as do extrinsic perturbations like an applied electric field. Under the influence of the intrinsic perturbations alone, a dynamic equilibrium is established where the distribution function is determined by Fermi-Dirac statistics. The effect of an applied electric field $\mathbf{E}$ is to shift the charge carrier distribution into the direction of the field, as stated by the semiclassical equation

$$\hbar\dot{\mathbf{k}} = q_c \mathbf{E},\tag{2.9}$$

leading to a non-zero and growing mean carrier velocity. The intrinsic scattering tends to oppose the growth of the crystal momentum in a way that a constant drift velocity is established. In the following, the derivation of several important scattering rates is presented,[12–14] and it is shown how the conductivity and the mobility can be derived from these scattering rates with the Boltzmann transport equation.

2.2.1 Methodology

The dynamics in a crystal due to the interaction of the charge carriers with intrinsic perturbations can be described in the framework of time-dependent perturbation theory. The transition probability per unit time from an electronic state $|\mathbf{k}\rangle$ to a state $|\mathbf{k}'\rangle$ is given by Fermi's golden rule as

$$P(\mathbf{k}',\mathbf{k};c',c) = \tfrac{2\pi}{\hbar} \left| \langle \mathbf{k}',c' | H_p | \mathbf{k},c \rangle \right|^2 \delta\big(E(\mathbf{k}',c') - E(\mathbf{k},c)\big),\tag{2.10}$$

where H_p is the perturbation Hamiltonian of a specific perturbation, e.g. phonons or chemical impurities. The states $|c\rangle$ and $|c'\rangle$ of the lattice crystal lattice before and after the scattering event are included as parameters in eq. (2.10). The Hamilton operator of impurity scattering does not include phonons, therefore $|c\rangle = |c'\rangle$ in this case. Using the Fourier transform of the scattering potential,

$$H_p = \tfrac{1}{\sqrt{V}} \sum_q \mathbf{A}(\mathbf{q},\mathbf{y}) e^{i\mathbf{qr}} + \mathbf{A}^\dagger(\mathbf{q},\mathbf{y}) e^{-i\mathbf{qr}}\tag{2.11}$$

(2.10) can be rewritten as[12]

$$P(\mathbf{k}',\mathbf{k};c',c) = \frac{2\pi}{\hbar}\frac{N}{V}\delta\big(E(\mathbf{k}',c') - E(\mathbf{k},c)\big)\cdot$$

$$\left|\sum_{\mathbf{q}}\langle c'|\mathbf{A}(\mathbf{q},\mathbf{y})|c\rangle G(\mathbf{k}',\mathbf{k},\mathbf{G})\delta_{\mathbf{G},\mathbf{k}\text{-}\mathbf{k}'+\mathbf{q}} + \langle c'|\mathbf{A}^\dagger(\mathbf{q},\mathbf{y})|c\rangle G(\mathbf{k}',\mathbf{k},\mathbf{K})\delta_{\mathbf{K},\mathbf{k}\text{-}\mathbf{k}'-\mathbf{q}}\right|^2, \tag{2.12}$$

where $\mathbf{G}$ and $\mathbf{K}$ are any vectors of the reciprocal lattice and

$$G(\mathbf{k}',\mathbf{k},\mathbf{G}) = \int_{\text{unit cell}} u_{\mathbf{k}'}^*(\mathbf{r})u_{\mathbf{k}}(\mathbf{r})e^{i\mathbf{G}\mathbf{r}}\mathrm{d}\mathbf{r} \tag{2.13}$$

is the so called overlap integral. The Kronecker deltas in eq. (2.12) guarantee the conservation of the crystal momentum by a vector of the reciprocal lattice. Depending on the reciprocal lattice vector that occurs in the overlap integral, scattering processes are classified as umklapp ($\mathbf{G} \neq \mathbf{0}$) or normal processes ($\mathbf{G} = \mathbf{0}$).

The scattering rate of charge carriers by charged point defects can already be evaluated with the above formalism. In the Thomas-Fermi approximation, the potential energy $U(\mathbf{r})$ of a charge carrier with charge q_c in the Yukawa potential of an ionized impurity with charge q_i is[12]

$$U(\mathbf{r}) = \frac{q_c q_i}{4\pi\epsilon r}e^{-q_0 r} = \frac{q_c q_i}{(2\pi)^3\epsilon}\int\frac{e^{i\mathbf{q}\mathbf{r}}}{q_0^2 + q^2}\mathrm{d}\mathbf{q}, \tag{2.14}$$

where by applying a Fourier transform in the second step the potential is directly expressed in the form of eq. (2.11). Here, $q_0 = (4\pi^2/\epsilon\cdot\partial n/\partial E_F)^{1/2}$ denotes the Thomas-Fermi wave vector, E_F the chemical potential, and $\epsilon = \epsilon_0\cdot\epsilon_r$ the permittivity. The scattering rate is proportional to the density n_i of ionized impurities, so neglecting umklapp processes the transition rate according to eq. (2.12) follows as

$$P(\mathbf{k}',\mathbf{k}) = n_i\frac{2\pi q_c^2 q_i^2}{\hbar\epsilon^2 V}\frac{1}{(q_0^2 + q^2)^2}G(\mathbf{k}',\mathbf{k},\mathbf{0})\delta(E_{\mathbf{k}'} - E_{\mathbf{k}}) \quad\text{with}\quad \mathbf{q} := \mathbf{k} - \mathbf{k}'. \tag{2.15}$$

If the transition rate strongly drops with increasing q as in eq. (2.15) for charged impurity scattering, neglecting umklapp processes can be justified for carriers in the Γ-valley because a large $\mathbf{q}$ on the order of a reciprocal vector implies a very small transition rate.

2.2.2   Electron-Phonon Scattering

The influence of phonons on the charge transport in semiconductors is special in a way that it cannot be reduced below the influence of the zero-point lattice oscillations. Because it is usually the dominating scattering mechanism under ambient conditions, electron-phonon scattering is great importance for charge transport. Before addressing various electron-phonon interaction mechanisms, the terminology of lattice vibrations as it is usually presented in textbooks on solid

state physics is briefly reviewed.[15,16] The common Hamiltonian of lattice vibrations in the harmonic approximation is

$$H = \frac{1}{2}\sum_{m,\nu}\frac{\mathbf{p}_{m,\nu}}{m_\nu} + \frac{1}{2}\sum_{m,\nu,\alpha,m',\nu',\alpha'}\frac{\partial^2 U\left(R_{m,\nu,\alpha},R_{m',\nu',\alpha'}\right)}{\partial R_{m,\nu,\alpha}\partial R_{m',\nu',\alpha'}}u_{m,\nu,\alpha}u_{m',\nu',\alpha'},$$

(2.16)

where the indices m, ν and α serve to address the unit cells of the crystal, the basis atoms in the basis, and the Cartesian coordinates, respectively. $\mathbf{R}$ denotes the position of lattice points, $\mathbf{p}$ is the momentum operator, $\mathbf{u}$ denotes the displacement of atoms from their equilibrium position, and U is the potential energy of the lattice atoms. This Hamiltonian can be diagonalized by a unitary transformation to normal coordinates $u_{\mathbf{q},j}$ and $p_{\mathbf{q},j}$ with

$$u_{\mathbf{q},j} = \frac{1}{\sqrt{N}}\sum_{n,\nu,\alpha}m_\nu \mathbf{e}^*_{j,\nu}\left(\mathbf{q}\right)\mathbf{u}_{n,\nu}e^{i\mathbf{q}\cdot\mathbf{R}_n}$$

$$p_{\mathbf{q},j} = \frac{1}{\sqrt{N}}\sum_{n,\nu,\alpha}m_\nu \mathbf{e}^*_{j,\nu}\left(\mathbf{q}\right)\mathbf{p}_{n,\nu}e^{i\mathbf{q}\cdot\mathbf{R}_n}.$$

(2.17)

It then reads

$$H = \frac{1}{2}\sum_{\mathbf{q},j}p^2_{\mathbf{q},j} + \omega_j\left(\mathbf{q}\right)^2 u^2_{\mathbf{q},j} = \sum_{\mathbf{q},j}\hbar\omega_j\left(\mathbf{q}\right)\left(b^\dagger_{\mathbf{q},j}b_{\mathbf{q},j} + \frac{1}{2}\right)$$

(2.18)

where the wavevector $\mathbf{q}$ lies in the first Brillouin zone and j denotes the phonon mode. On the rhs of eq. (2.18) the phonon annihilation operator and its adjoint, the creation operator, are introduced:

$$b_{\mathbf{q},j} = \sqrt{\frac{\omega_j(\mathbf{q})}{2\hbar}}u_{\mathbf{q},j} + \frac{i}{\sqrt{2\hbar\omega_j(\mathbf{q})}}p_{\mathbf{q},j}$$

$$b^\dagger_{\mathbf{q},j} = \sqrt{\frac{\omega_j(\mathbf{q})}{2\hbar}}u_{\mathbf{q},j} - \frac{i}{\sqrt{2\hbar\omega_j(\mathbf{q})}}p_{\mathbf{q},j}.$$

(2.19)

For future use it is necessary to know the expression for the core displacement in terms of normal modes:[16]

$$\mathbf{u}_{m,\nu} = \frac{1}{\sqrt{Nm_\nu}}\sum_{\mathbf{q},j}e^{i\mathbf{q}\cdot\mathbf{R}_m}\mathbf{e}_{\nu,j}u_{\mathbf{q},j} = \sqrt{\frac{\hbar}{Nm_\nu\omega_j(\mathbf{q})}}\sum_{\mathbf{q},j}e^{i\mathbf{q}\cdot\mathbf{R}_m}\mathbf{e}_{\nu,j}\left(b_{\mathbf{q},j} + b^\dagger_{\mathbf{q},j}\right).$$

(2.20)

Here, N is the number of unit cells that form the crystal, and $\mathbf{e}_{\nu,j}$ is the displacement eigenvector for the basis atom ν with mass m_ν of the lattice normal mode j. An important distinction between acoustical and optical normal modes is that the displacement of the different atoms in a unit cell is usually in the same direction for acoustical modes but not for optical modes. The normal modes are further classified into longitudinal (exactly one for acoustical phonons) and transverse modes for which $\mathbf{e}_\nu \parallel \mathbf{q}$ respectively $\mathbf{e}_\nu \perp \mathbf{q}$ (approximately) holds.

A very basic description of the electron-phonon interaction can be achieved by a first order expansion of the electron-lattice interaction energy in the lattice atom coordinates:

$$H_{ep} = \sum_{m,\nu} \nabla_{\mathbf{R}} U \left(\mathbf{r} - \mathbf{R}_{m,\nu} \right) \mathbf{u}_{m,\nu} . \tag{2.21}$$

With a Fourier transform of the electron potential energy $U \left(\mathbf{r} - \mathbf{R}_{m,\nu} \right)$ and eq. (2.20) for the $\mathbf{u}_{m,\nu}$, the interaction energy in eq. (2.21) directly takes the form of eq. (2.11).[15] While this approach is principally exact for small displacements, it is not useful for practical considerations unless $U \left(\mathbf{r} - \mathbf{R}_{m,\nu} \right)$ is known from calculations. Hence, the electron-phonon interaction is often described at a less fundamental level, relying on a small set of material parameters. This approach is detailed in the following for several electron-phonon interaction mechanisms.

When a crystal is dilated the energetic positions of the band extrema shift, i.e. a *deformation potential* is created. This form of interaction appears in all crystals in contrast to scattering with macroscopic electric fields arising from polar optical phonons, which are only relevant in compound semiconductors. For acoustic phonons the displacement of different basis atoms is in the same direction. The dilation and thus the deformation potential are therefore proportional to the spatial change of the atom displacement $\mathbf{u}_{m,\nu}$ created by the longitudinal acoustic phonons (transverse modes exhibit significantly less dilation). In the long wavelength limit, the displacement vectors $\mathbf{u}_{m,\nu}$ can be regarded as a continuous displacement field $\mathbf{u}(\mathbf{r})$ by allowing any value $\mathbf{r}$ for the set of lattice points $\mathbf{R}_m$ in eq. (2.20). Hence, the perturbation Hamiltonian can be arranged as

$$H_p = D_{ac} \left(\mathbf{e}_u \nabla \right) \mathbf{u}(\mathbf{r}) \cdot \mathbf{e}_u \underset{(2.20)}{=} D_{ac} \mathbf{q} \mathbf{u}(\mathbf{r}), \tag{2.22}$$

where $\mathbf{e}_u$ is a unit vector in the direction of $\mathbf{u}$. In optical phonons different atoms in the basis vibrate against each other. Therefore the dilation is directly proportional to the displacement[III]

$$H_p = D_{npo} \mathbf{u}(\mathbf{r}). \tag{2.23}$$

With eq. (2.20) the Hamiltonians (2.22) and (2.23) take the form of eq. (2.11) without further ado, so the transition rate for normal processes follows directly from eq. (2.12) as

---

[III] For concrete applications, the question arises how a continuous displacement field can be created that takes the different displacements of different basis atoms into account. Even in specialized books (e.g. ref. 12,17) this problem is often circumvented by dropping the basis index ν beforehand. For the use here one may think of the continuous field $\mathbf{u}(\mathbf{r})$ as being constructed of some linear combination of the $\mathbf{u}_{m,\nu}$:

$$\mathbf{u}_j(\mathbf{r}) \propto \sum_{\nu} A_{\nu,j} \mathbf{e}_{\nu,j}$$

$$P(\mathbf{k}',\mathbf{k}) = \frac{\pi}{\rho V \omega_j(\mathbf{q})} G(\mathbf{k}',\mathbf{k},\mathbf{0}) D \cdot \begin{bmatrix} n_{\mathbf{q}j}\delta(E_{\mathbf{k}'} - E_{\mathbf{k}} - \hbar\omega_j(\mathbf{q})) \\ (n_{\mathbf{q}j}+1)\delta(E_{\mathbf{k}'} - E_{\mathbf{k}} + \hbar\omega_j(\mathbf{q})) \end{bmatrix}, \tag{2.24}$$

with $D = D_{ac}^2 \mathbf{q}^2$ and $D = D_{npo}^2$ for acoustic and optic modes, respectively. The factors with $n_{\mathbf{q}j}$ and $(n_{\mathbf{q}j}+1)$ correspond to transitions that go along with phonon absorption and emission, respectively. It can already be concluded from eq. (2.24) electron-phonon scattering increases strongly with the temperature of the lattice T_l because of growing phonon population.

In compound semiconductors, the different sorts of atoms generally have different ionic charges, so phonons can displace the differently charged ions against each other in a way that a macroscopic polarization is created, which interacts with the electrons. In case of acoustic phonons this mechanism is termed *piezoelectric scattering*, whereas it is known as *polar interaction* for polar optical phonons. The former mechanism only occurs in semiconductors without inversion symmetry and is therefore not taken into account here. The polarization field of the optical phonons is proportional to the ion displacement field

$$\mathbf{P}(\mathbf{r}) \propto \mathbf{u}(\mathbf{r}). \tag{2.25}$$

This polarization field induces an electric field $\mathbf{E}(\mathbf{r})$ and thus an electric potential $\phi(\mathbf{r})$. Denoting the charge carrier density with ρ the interaction Hamiltonian accordingly reads

$$H_p = \int \rho_c(\mathbf{r})\phi(\mathbf{r})\mathrm{dr}. \tag{2.26}$$

As outlined in ref. 12, the transition rate can be derived from eq. (2.26) and eq. (2.25) giving

$$P(\mathbf{k}',\mathbf{k}) = \frac{\pi e^2 \omega_{op}}{V}\left(\frac{1}{\epsilon(\infty)} - \frac{1}{\epsilon(0)}\right) G(\mathbf{k}',\mathbf{k},\mathbf{0})\left(\frac{q}{q^2 + q_0^2}\right)^2 \begin{bmatrix} n_{\mathbf{q}}\delta(E_{\mathbf{k}'} - E_{\mathbf{k}} - \hbar\omega_{op}) \\ (n_{\mathbf{q}}+1)\delta(E_{\mathbf{k}'} - E_{\mathbf{k}} + \hbar\omega_{op}) \end{bmatrix}, \tag{2.27}$$

where ω_{op} denotes the optical phonon frequency.[IV]

2.2.3   Mobilities

The purpose of this section is to show how the mobility $\mu = |\mathbf{v}_D|/|\mathbf{E}|$ can be derived on the basis of the microscopic transition rates $P(\mathbf{k}',\mathbf{k})$. Under the influence of an applied field $\mathbf{E}$ the charge carriers gain energy and the charge carrier distribution changes. The magnitude of this change depends on the strength of the field and the restoring power of the intrinsic scattering mechanisms,

---

[IV] The momentum relaxation time and the mobility that are derived from (2.27) are often used in practice. However, the proportionality parameter in eq. (2.25), which also enters eq. (2.27), was originally derived for the special case of a lattice consisting of two sorts of atoms and having a single longitudinal optical mode using the concept of an effective ionic charge.[18–21] A strict generalization for lattices with several longitudinal phonon branches can hardly be found in the literature.

which dissipate the energy gained by the field and tend to establish a Fermi-Dirac occupation probability. For a small perturbing field strength, the resulting charge carrier distribution $f(\mathbf{k})$ will not be very different from the distribution $f_0(\mathbf{k})$ without an applied field, so

$$f(\mathbf{k}) = f_0(\mathbf{k}) + f_1(\mathbf{k}) \tag{2.28}$$

with $f_1 \ll f_0$. Because $f_0(\mathbf{k}) = f_0(-\mathbf{k})$ (in the parabolic approximation) the drift velocity is only determined by the nonequilibrium term $f_1(\mathbf{k})$:[12]

$$v_D = \frac{2}{n(2\pi)^3} \int \mathbf{v}(\mathbf{k}) f_1(\mathbf{k}) d\mathbf{k}. \tag{2.29}$$

To solve this integral, $f_1(\mathbf{k})$ must be determined. The starting point for this task is the Boltzmann transport equation[15]

$$\frac{\partial}{\partial t} f + \nabla_{\mathbf{r}} f \cdot \dot{\mathbf{r}} + \nabla_{\mathbf{k}} f \cdot \dot{\mathbf{k}} = \frac{V}{(2\pi)^3} \int f_{\mathbf{k}'} P(\mathbf{k}, \mathbf{k}')(1 - f_{\mathbf{k}}) - f_{\mathbf{k}} P(\mathbf{k}', \mathbf{k})(1 - f_{\mathbf{k}'}) d\mathbf{k}'. \tag{2.30}$$

The Boltzmann equation states that the total change of the distribution function $f(\mathbf{r}, \mathbf{k}, t)$ is given by scattering in and out of the microscopic Bloch states $|\mathbf{k}\rangle$. By analyzing the properties of the transition rates $P(\mathbf{k}', \mathbf{k})$, it can be shown that in case of velocity randomizing (deformation potential) and elastic (charged impurity) scattering processes the rhs of eq. (2.30) can be written as[12]

$$-\frac{f_1(\mathbf{k})}{\tau(\mathbf{k})}. \tag{2.31}$$

This is commonly referred to as the relaxation time approximation (RTA). Here, $\tau(\mathbf{k})$ is the so called momentum relaxation time (MRT), which depends on an integral of the $P(\mathbf{k}', \mathbf{k})$.[12] Setting the overlap integral $G(\mathbf{k}', \mathbf{k}, 0) = 1$, the MRTs due to acoustic and optical deformation potential scattering and ionized impurity scattering can be calculated as[12,22]

$$\tau_{ac} = \frac{\pi \hbar^4 \rho c_l^2}{\sqrt{2m^3} D_{ac}^2 k T_l} \cdot \varepsilon^{-1/2} \tag{2.32}$$

$$\tau_{npo} = \frac{\sqrt{2}\pi \hbar^3 \rho \omega_{op}}{m^{*3/2} D_{npo}^2} \left(\frac{\sqrt{\varepsilon + \hbar \omega_{op}}}{e^{x_0} - 1} + \frac{e^{x_0}\sqrt{\varepsilon - \hbar \omega_{op}}}{e^{x_0} - 1} \cdot \Theta(\varepsilon - \hbar \omega_{op}) \right)^{-1} \tag{2.33}$$

$$\tau_{ion} = \frac{16\sqrt{2m^*}\pi(\epsilon_r \epsilon_0)^2}{n_i e^4} \varepsilon^{3/2} \left(\log(1 + 4\varepsilon/\varepsilon_0) - \frac{\varepsilon}{\varepsilon + \varepsilon_0/4} \right)^{-1} \tag{2.34}$$

The meaning of the symbols is explained in Table 1.

Table 1 Physical parameters that are relevant for charge transport.

ρ	mass density
c_l	velocity of sound (longitudinal acoustic branch)
$\mathcal{E}$	electron energy
T_e	charge carrier temperature
T_l	lattice temperature
D_{ac}	acoustic deformation potential
D_{npo}	optical deformation potential
$\mathcal{E}_0$	$\hbar^2 q_0^2 / 2m$ with the Thomas-Fermi screening wavevector $q_0 = (4\pi^2 / \epsilon \cdot \partial n / \partial E_F)^{1/2}$
n_i	charged defect concentration
$n(x_0)$	optical phonon occupation number
x_e	$\hbar\omega_l / kT_e$
x_0	$\hbar\omega_l / kT_l$
D_{po}	electron-polar optical phonon coupling $(1 / \epsilon(\infty) - 1 / \epsilon(0)) \cdot me\hbar\omega_l / (4\pi\hbar^2)$
K_n	modified Bessel functions of the second kind.

The contributions of different scattering mechanisms are combined into the total momentum relaxation rate according to the Matthiessen rule

$$\frac{1}{\tau} = \frac{1}{\tau_1} + \frac{1}{\tau_2} + \frac{1}{\tau_3} + \dots \qquad (2.35)$$

In a homogeneous material the spatial derivative $\nabla_\mathbf{r}$ in eq. (2.30) vanishes. Denoting the charge carrier energy with ε, it follows

$$\frac{\partial}{\partial t} f_1 + \frac{\partial f}{\partial \varepsilon} \underbrace{\nabla_\mathbf{k}\varepsilon \cdot \dot{\mathbf{k}}}_{q\mathbf{vE}} = -\frac{f_1}{\tau(\mathbf{k})} \qquad (2.36)$$

The solution of eq. (2.36) for a field of the form $\mathbf{E} = \mathbf{E}_0 \exp(-i\omega t)$ is

$$f_1 = -\frac{q\tau\mathbf{v}\mathbf{E}_0}{1 - i\omega\tau}\frac{\partial f_0(\varepsilon)}{\partial \varepsilon}. \qquad (2.37)$$

Putting this into eq. (2.29) yields for the drift velocity

$$v_D = -\frac{2}{n(2\pi)^3}\int \mathbf{v}\frac{q\tau\mathbf{v}\mathbf{E}_0}{1 - i\omega\tau}\cdot\frac{\partial f_0}{\partial \varepsilon}\,\mathrm{d}\mathbf{k}. \qquad (2.38)$$

For a spherical parabolic band, i.e. with $\varepsilon(\mathbf{k}) = \hbar^2 k^2 / 2m^*$, this can be simplified to[12]

$$v_D = -\frac{4qE}{n(2\pi)^3 3m^*}\int \varepsilon \frac{\tau}{1 - i\omega\tau}\cdot\frac{\partial f_0}{\partial \varepsilon}\,\mathrm{d}\mathbf{k}. \qquad (2.39)$$

Hence, the mobility $\mu = |\mathbf{v}_D| / |\mathbf{E}|$ follows as

$$\mu = \frac{e}{m^*} \frac{(2m^*)^{3/2}}{3\pi^2 \hbar^3 n} \cdot \int \varepsilon^{3/2} \frac{\tau}{1-i\omega\tau} \cdot \frac{\partial f_0}{\partial \varepsilon} d\varepsilon \tag{2.40}$$

$$\approx \frac{e}{m^*} \frac{1}{1-i\omega\langle\tau\rangle} \underbrace{\frac{(2m^*)^{3/2}}{3\pi^2 \hbar^3 n} \cdot \int \varepsilon^{3/2} \tau \cdot \frac{\partial f_0}{\partial \varepsilon} d\varepsilon}_{:=\langle\tau\rangle} \tag{2.41}$$

With the approximation in eq. (2.41), the mobility exhibits the functional form of the classical free electron model (2.7).[V] Assuming non-degenerate statistics[VI] analytic mobilities can be derived from (2.40) for ionized impurity and acoustic deformation potential scattering, which exhibit characteristic temperature dependencies of approximately $T_e^{3/2}$ respectively $T_l^{-1} T_e^{-1/2}$. In the general case, however, the mobility has to be evaluated numerically taking eq. (2.35) into account.

For electron scattering with polar optical phonons, a MRT in terms of the RTA does not exist.[VII] Only in the high temperature limit, when the collisions with optical phonons can be approximated as being elastic, can the momentum loss rate parallel to the applied field[13]

$$\frac{1}{\tau_{po}} = \frac{eD_{po}}{\sqrt{2m\varepsilon}} \left(n(x_0)\sqrt{1+\hbar\omega_{op}/\varepsilon} + (n(x_0)+1)\Re\left(\sqrt{1-\hbar\omega_{op}/\varepsilon}\right) + \right.$$
$$\left. \frac{\hbar\omega_{op}}{E} \left[(n(x_0)+1)\mathrm{asinh}\left(\Re\left(\sqrt{\varepsilon/\hbar\omega_{op}-1}\right)\right) - n(x_0)\mathrm{asinh}\left(\sqrt{\varepsilon/\hbar\omega_{op}}\right) \right] \right) \tag{2.42}$$

be taken as a MRT within the meaning of eq. (2.31).

2.3 Charge Transport across Hetero-Interfaces

The transport of an electron or a hole across a hetero-interface between a molecular species and a solid state electrode is the fundamental process in technological applications such as catalysis, electrochemistry, or hybrid photovoltaics. In dye solar cells the heterogeneous electron transfer (HET) takes place between a photoexcited molecule and a semiconductor to which the molecule is chemisorbed. The transition usually occurs from a localized molecular orbital into the dense man-

---

[V] The approximation in eq. (2.41) becomes exact when the MRT does not depend on the energy, when the temperature is very low so that the derivative of the distribution function is $-\delta(\varepsilon - \mu)$, or for $\omega \to 0$.

[VI] Non-degenerate statistics means the Fermi level lies so deep in the band gap that the Fermi distribution function can be approximated by a Boltzmann distribution.

[VII] An analytic approximation for the mobility due to electron scattering with polar optical phonons has been derived by E. M. Conwell using a different methodology.[14]

ifold of semiconductor states.[VIII] Physical models of HET usually differentiate between adiabatic and non-adiabatic (NA) electron transfer. The latter is a quantum mechanical tunneling process, whereas in the former the nuclear motion induces a shift of an electronic state from the molecule to the semiconductor. Both pictures of electron transfer can be coherently understood by a formal approach that is based on a quantum-classical Born-Oppenheimer separation.[23,24]

The Born-Oppenheimer approximation is based on the notion that the electrons move much faster than the cores. Therefore, the core positions $\mathbf{R}$ can be approximated as being fixed for the electron-core interaction. So the quasi-stationary Hamiltonian for the electrons can be written as

$$H_e\left(\mathbf{R}\right) = T_e + V_{ee}\left(\mathbf{r}\right) + V_{ec}\left(\mathbf{r};\mathbf{R}\right). \tag{2.43}$$

Here, the first, second, and last term on the rhs describe the electron's kinetic energy, the electron-electron, and the electron-core interaction, respectively. The eigenfunctions $\varphi_n\left(\mathbf{r};\mathbf{R}\right)$ of this Hamiltonian depend parametrically on the core positions $\mathbf{R}$. The same applies to the energy eigenvalue $E_e\left(\mathbf{R}\right)$ which becomes a function of the nuclear coordinates. Including the kinetic energy of the cores T_c and the core-core interaction energy V_{cc} the full Hamiltonian is given as

$$H = H_e + T_c + V_{cc}. \tag{2.44}$$

An ansatz to the solution of eq. (2.44) is a series $\sum_n c_n \cdot \chi_n\left(\mathbf{R}\right)\varphi_n\left(\mathbf{r};\mathbf{R}\right)$[IX] which yields a conditional equation for the χ_n:[25]

$$\sum_n \left((T_c + \underbrace{E_n\left(\mathbf{R}\right) + V_{cc} + \theta_{nn}}_{U_n\left(\mathbf{R}\right)})\delta_{mn} + \sum_{m \neq nn} \theta_{mn}(1-\delta_{mn}) \right)\chi_n\left(\mathbf{R}\right) = E\chi_m\left(\mathbf{R}\right). \tag{2.45}$$

Here, θ_{mn} denotes the so-called nonadiabacity operator. The Born-Oppenheimer separation consists of neglecting the off-diagonal part of this operator, i.e. the last term on the lhs of eq. (2.45), so that the solutions can be expressed as $\chi\left(\mathbf{R}\right)\varphi\left(\mathbf{r};\mathbf{R}\right)$. A further simplification is to neglect the quantum mechanical nature of the cores and to describe their dynamics with a classical trajectory $\mathbf{R}(t)$. In this case, the electronic wavefunction $\varphi_n\left(\mathbf{r};\mathbf{R}(t)\right)$ becomes directly time-dependent through the motion of the cores. The adiabatic basis set $\varphi_n\left(\mathbf{r};\mathbf{R}(t)\right)$ can be used to describe the excited electronic state of a molecule in HET[X]

$$\psi\left(\mathbf{r},t\right) = \sum_n c_n\left(t\right)\cdot\varphi_n\left(\mathbf{r};\mathbf{R}\left(t\right)\right). \tag{2.46}$$

[VIII] In certain strongly coupled hybrids the excitation directly transfers the electron to the semiconductor.

[IX] Another possibility would be to use two uncoupled basis sets $\chi_n\left(\mathbf{R}\right)$ and $\varphi_m\left(\mathbf{r}\right)$. In this case the general solution could be expressed as $\sum_{n,m} c_{mn}\chi_n\left(\mathbf{R}\right)\varphi_m\left(\mathbf{r}\right)$.

[X] To describe the change of $\psi\left(\mathbf{r},t\right)$, (2.43) has of course to be adapted to incorporate the interaction of the molecule with the electrode.

The time-dependent probability p_D that the electron is localized at the donor molecule is the integral of $\left|\psi\left(\mathbf{r},t\right)\right|^2$ over the spatial region occupied by the donor

$$p_D = \sum_{n,m} c_n\left(t\right)^* \cdot c_m\left(t\right) \int_{Donor} \varphi_n\left(\mathbf{r};\mathbf{R}\right)^* \varphi_m\left(\mathbf{r};\mathbf{R}\right) \mathrm{d}^3\mathbf{r}. \tag{2.47}$$

Hence, the transfer rate follows from the time derivative of (2.47) as[24]

$$\frac{d}{dt}p_D = \sum_{n,m} \frac{d\left(c_n\left(t\right)^* \cdot c_m\left(t\right)\right)}{dt} \int_{Donor} \varphi_n^* \varphi_m \, \mathrm{d}^3\mathbf{r} + \sum_{n,m} c_n^* \cdot c_m \int_{Donor} \frac{d\left(\varphi_n^*\left(\mathbf{r},\mathbf{R}(t)\right)\varphi_m\left(\mathbf{r},\mathbf{R}(t)\right)\right)}{dt} \mathrm{d}^3\mathbf{r}. \tag{2.48}$$

The first term on the rhs of eq. (2.48) can be interpreted as the NA electron transfer contribution because it arises from a change of the adiabatic state population. Hence, the NA component can be described by Fermi's golden rule, which specifically describes quantum transitions by changes in the occupation probability of otherwise stationary states. Within the golden rule approximation, the NA transfer rate between the localized molecular donor D and an acceptor state A is given as[26]

$$k = \frac{2\pi}{\hbar}\left|V_{DA}\right|^2 FCWD, \tag{2.49}$$

where V_{DA} is the transition matrix element that describes the electronic coupling between donor and acceptor, and *FCWD* is the density of acceptor states weighted by the Franck Condon factors of the vibrational transitions that accompany the electronic transition.[XI] Due to this change of the molecule's vibrational state, the electronic donor level is generally not isoenergetic with the semiconductor acceptor states: Energy conservation demands that the vibrational energy that a molecule gains (looses) by the injection process lowers (raises) the energetic position of the injected electron. The second term in (2.48) describes the transfer rate that arises from an adiabatic change of the basis wavefunctions due to the nuclear motion. Therefore, it describes the adiabatic electron transfer component. Since the adiabatic transfer is induced solely by the nuclear motion, coherent vibrations of the atom cores can also lead to a periodic modulation of the electron transfer rate.[24,27] Except for altering the adiabatic wavefunctions, the nuclear motion also modifies the electronic energy levels (2.43) and therefore affects the energetic position of the injected electron.

[XI] The probability of NA electron transfer involving a vibrational transition $\chi_n\left(\mathbf{R}\right) \to \chi_m\left(\mathbf{R}\right)$ transfer depends on the overlap of the nuclear wave functions $\left|\left\langle\chi_n\left(\mathbf{R}\right)\middle|\chi_m\left(\mathbf{R}\right)\right\rangle\right|^2$, the so called Franck-Condon factor.

3 Experimental Details

This chapter gives a survey on spectroscopic techniques that are employed in this thesis. The experiments rely strongly on pump-probe techniques: Optical-pump terahertz-probe (OPTP), transient absorption (TA), and time-resolved two photon-photoemission (2PPE) spectroscopy. The basic principle of the different techniques is the same: A laser pulse deposits energy in the system under study, and this excess energy changes the occupation probabilities of electron, hole, and phonon states, which results in different macroscopic properties such as changes in the transmittance and absorbance. These macroscopic changes can be measured with OPTP spectroscopy in the far infrared (IR) range, or with TA in the visible to mid-IR range. Direct access to the time-dependent non-equilibrium distribution of photoexcited electrons can be achieved with 2PPE.

The fundamental laser pulses which drive the various pump-probe experiments stem from a commercial laser system. Femtosecond p-polarized laser pulses with a central wavelength of 800 nm and a typical energy of 12 nJ are emitted from a Ti:sapphire oscillator (Mira, Coherent Inc.) at a rate of 80 MHz. These pulses are expanded by a grating stretcher and then used to seed the amplifier (RegA, Coherent Inc.). The amplifier delivers 10 µJ pulses with a center wavelength of 800 nm at a repetition rate of 150 kHz. After running through a grating compressor, the amplifier pulses have a typical autocorrelation length of 70-80 fs (fwhm).

If not stated otherwise, all measurements are performed at room temperature and high or ultra-high vacuum conditions.

3.1 OPTP Spectroscopy

OPTP spectroscopy is very well suited to study low energy excitations such as free or weakly bound charge carriers due to the low probe photon energy of a few meV only. To perform OPTP experiments the 800 nm output of the amplifier is split into three branches. The first branch is used to generate THz radiation, the second to generate the pump pulses and the third to sample the THz pulses (Figure 3-1). THz radiation is created by focusing the fundamental 800 nm pulses in a [110] oriented ZnTe crystal.[28] This process is known as optical rectification, i.e. difference frequency generation and results in multi-cycle electromagnetic pulses with a broad spectrum from about 0.5 THz to 2.5 THz that are collected and collimated with a parabolic mirror and focused to a spot of about 1 mm (fwhm field amplitude) at the sample position by a second parabolic mirror. The size of the THz pulses can be estimated by the rise of the voltage signal of a pyroe-

lectric LiTaO$_3$ THz detector (SPH-62, Spectrum Detector Inc.[I]) while it is driven into the THz beam path. A high-density polyethylene (HDPE) filter behind the first parabolic mirror, which is transparent to THz radiation, screens any remaining 800 nm or fluorescence light from the sample. A second HDPE filter prevents remaining pump light from reaching and thus exciting the Si-wafer. After travelling through the sample a third and fourth parabolic mirror recollimate respectively focus the THz radiation into another [110] oriented ZnTe crystal. In this crystal the THz pulses are electro-optically sampled[28,29] using the 800 nm laser pulses of the third branch. For this purpose, the 800 nm beam is collinearly superimposed with the THz radiation in the crystal by using a high resistivity Si wafer, which is transparent to THz radiation but not to the 800 nm light. The ZnTe crystal is aligned with the [001] axis perpendicular to the optical table. Hence, the p-polarized THz pulses induce a birefringence in the crystal with refractive indices of $n \pm \Delta n$ along the $[1\bar{1}\sqrt{2}]$ and the $[\bar{1}1\sqrt{2}]$ axis of the crystal, with Δn being proportional to the field strength E of the p-polarized THz-pulses (Pockels effect).[28] Because of the induced birefringence, the linearly polarized optical sampling pulses (s-polarized after the $\lambda/2$ plate) become elliptically polarized in the ZnTe crystal. After passing through a $\lambda/4$ plate, which is aligned with the fast axis parallel to the s-direction, the sampling pulses become linearly polarized with the polarization axis slightly turned out of the s-direction.[30] A Wollaston prism splits the sampling pulses into s- and p-polarized components, which are each focused onto a different photodiode. The differential voltage of these photodiodes is proportional to the THz pulse electric field strength E in the ZnTe crystal.[30]
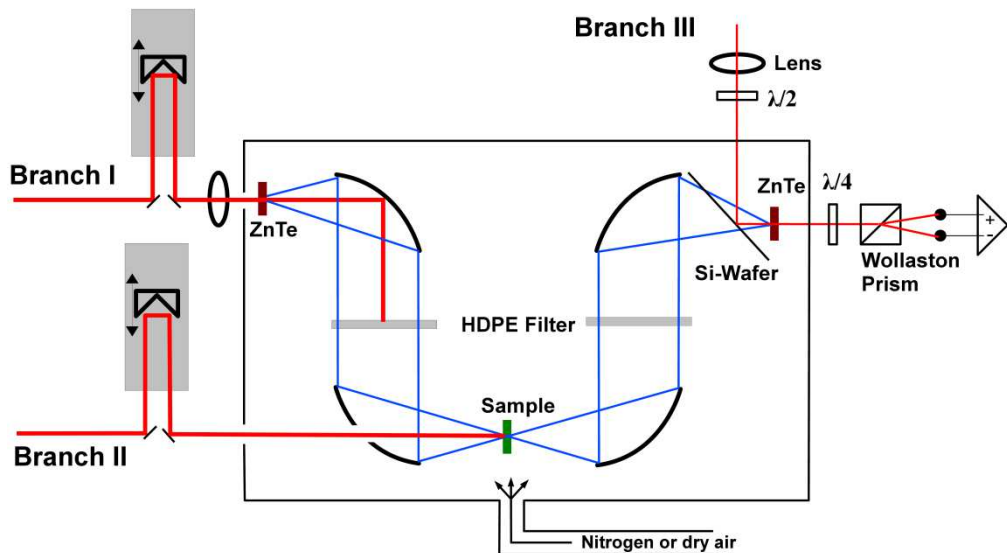

Figure 3-1 Scheme of the OPTP setup.

Depending on the specific sample, the pump pulses (branch II) can be chosen as either the fundamental 800 nm laser light, frequency doubled 400 nm light, or the output of a non-collinear optical parametric amplifier (NOPA). For second harmonic generation (SHG), the 800 nm pulses are focused into a 300 μm thick β-BaB$_2$O$_4$ crystal yielding 400 nm pulses with a maximum energy of 0.5 μJ. The NOPA is based on a scheme presented by Piel et al.[31] that is detailed in the PhD theses of R. Ernstorfer[32] and L. Gundlach.[33] In brief: The fundamental 800 nm pulses are split into two beams. One is focused into a 3 mm thick sapphire crystal to generate a white-light continuum (WLC), and the other beam is used to create 400 nm pulses by SHG in a 300 μm thick β-BaB$_2$O$_4$ crystal. Both beams are then superimposed under a certain angle in another β-BaB$_2$O$_4$ crystal where the 400 nm pump pulses amplify the WLC seed. For the experiments in this thesis the NOPA output was tuned to about 500 nm center wavelength with a pulse energy up to 130 nJ.

The OPTP setup comprises two different delay stages, which delay branch I and II. The pump-probe delay t is introduced by delaying the pump pulse with respect to the sampling pulse. Another delay stage changes the arrival time t' of the THz pulse relative to the optical sampling pulse. This way each sampled part of the THz waveform interacts with the sample at the same pump-probe delay. As inferred from the fastest observed signal rise, the OPTP spectrometer has a time resolution of ≤ 500 fs.

During the measurements, the samples are usually kept in a vacuum chamber with quartz windows, which has been manufactured at the HZB. This homemade chamber guarantees a vacuum better than $5 \cdot 10^{-4}$ mbar. For temperature-dependent measurements, a commercial cryostat system based on a modified ST-100-FTIR cryostat from Janis Research Inc. is employed. The cryostat has an elongated cold finger on which three samples can be mounted simultaneously. The cold finger is surrounded by a radiation shield and enclosed by the cryostat housing, which has quartz entrance and exit windows. Under operation the sample chamber which contains the cold finger is evacuated. Resistive heating wires and two Si-diode temperature sensors are attached to the cold finger, which is in thermal contact with a liquid helium reservoir. Temperature control is realized by regulating the cooling power via the liquid helium flow-through and the power of the resistive heater (LakeShore, Model 331).

3.2 Interpreting OPTP Measurements

The pump pulse changes the properties of the sample, which results in a different probe pulse transmission after the sample. For a thin film, the pump-induced relative transmission change $\Delta E(\omega)/E(\omega)$ is proportional to the photoconductivity:[34,35]

$$\Delta \tilde{\sigma}(\omega, t, z) = \Delta \sigma(\omega, t) \cdot e^{-\alpha z} = -\frac{\Delta E(\omega)}{E(\omega)} \cdot \frac{\epsilon_0 c (n_1 + n_3) \alpha}{1 - e^{-\alpha d}} \cdot e^{-\alpha z}, \tag{3.1}$$

where $n_1 = 1$ and $n_3 = 1$ denote the terahertz refractive indices of the medium before (vacuum) and after the sample (quartz or sapphire substrate), and c, d, α, and ϵ_0 are the speed of light, layer thickness, optical absorption coefficient, and vacuum permittivity, respectively.[II] The term $e^{-\alpha z}$ in eq. (3.1) describes the spatial variation of the photoconductivity within the photoexcited film due to an exponential optical absorption profile. With the scanned THz waveform $E(t')$ and its pump-induced change $\Delta E(t')$ for different pump-probe delays t and a subsequent Fourier transformation, the photoconductivity $\Delta\sigma(\omega, t)$ can be retrieved from eq. (3.1).[III]
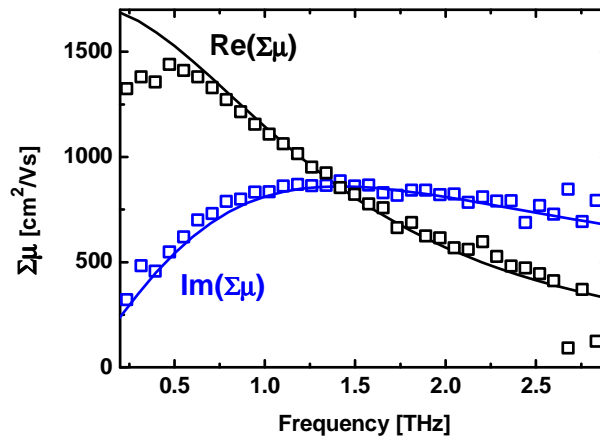

Figure 3-2 Spectrum of the combined electron and hole mobility $\Sigma\mu$ of an InP single crystal. The solid lines are a fit of the simple Drude model eq. (2.7) giving a momentum relaxation time of 110 fs. The scatter of the data above 2.7 THz and the mismatch of the data with the fit below about 0.5 THz exemplify the reliable frequency range.

An important parameter for the measurement of a reliable frequency dependence is the ratio of probe and pump spot size. If this ratio is too high, frequency dependent artifacts are introduced because the frequencies are not uniformly distributed along the beam waist. High frequency components are typically more tightly focused than lower frequencies.[38,39] The bigger the pump spot is, compared to the probe spot, the more homogenously the probed region is excited. However, the bigger the pump spot is, the smaller is the maximum attainable excitation density. Hence, homogeneity and excitation density have to be balanced. Wherever frequency resolved

---

[II] Additional care must be taken when the sample is inhomogeneous on length scales comparable to or smaller than the probe wavelengths. In this case, an effective medium approach (EMA) must be taken into account for an analysis of the photoconductivity. This is demonstrated in section 4.4.2 where the EMA is applied to nanostructured samples

[III] Eq. (3.1) is only a good approximation when $\Delta\sigma(\omega, t)$ is quasi-constant on the timescale of the THz spectrometer time resolution.[36,37] Otherwise artifacts are introduced because the sample changes its properties during the probing process.

data is presented in this thesis, care was taken to use a big enough pump-spot. A simple criterion is applied for this purpose: If the photoconductivity spectrum of an InP single crystal exhibits a Drude-like behavior, the pump spot is considered big enough. Agreement with the Drude model is typically achieved within a frequency range of about 0.5 to 2.7 THz (Figure 3-2). Below 0.5 THz the measured mobility deviates from the theoretical Drude behavior. This happens because these long wavelengths (0.25 THz corresponds to 1.2 mm wavelength) are not focused so tight that the pump intensity appears spatially homogenous. Above around 2.7 THz the data gets unreliable because of the high frequency cut-off of the THz pulse spectrum.

A measurement of $\Delta\sigma(\omega,t)$ means sampling the THz probe-pulse for each pump-probe delay t, which is inconvenient when the signal to noise ratio (SNR) is low because of a small photoconductivity

$$\Delta\sigma = en_{eh}(\mu_e + \mu_h) = en_{eh}\Sigma\mu \qquad (3.2)$$

Here, n_{eh} denotes the density of photoexcited electron-hole pairs and $\Sigma\mu$ is the sum of the electron and hole mobility (μ_e and μ_h). In this case, a simpler but approximate mode is often used: The pump-probe delay is scanned for a fixed position at the THz waveform, typically the maximum amplitude.[36] When this simplified method is used in this thesis, it was checked beforehand that it yields the same results as sampling the whole probe-pulses.[IV]

Absorption of photons in a semiconductor generally creates electron-hole pairs if the photon energy is higher than the band gap. If the dilution of the charge carrier density due to recombination and diffusion is negligible over about 500 fs (the time resolution), the excess electron-hole pair can be estimated as

$$n_{eh}(z) = F\cdot(1-R)\alpha e^{-\alpha z}. \qquad (3.3)$$

Here, F denotes the pump-photon fluence and R is the reflectivity of the sample. Hence, the combined mobility $\Sigma\mu = \mu_e + \mu_h$ can be calculated from the maximum conductivity $\Delta\sigma(t_0)$ just after the excitation at time t_0 using eq. (3.1), (3.2) and (3.3):

$$\Sigma\mu = -\frac{\Delta E(\omega)}{E(\omega)}\cdot\frac{\epsilon_0 c(n_1+n_3)}{e(1-e^{-\alpha d})F(1-R)}. \qquad (3.4)$$

However, if the material exhibits a fast initial decay of the photoconductivity, this would lead to artifacts in the frequency domain.[36,37] To estimate the mobility in such materials, $\Delta E(\omega)/E(\omega)$

[IV] Materials with a relatively low mobility, e.g. the nanorods in this thesis, often exhibit a photoconductivity spectrum $\Delta\sigma(\omega)$ that can be roughly approximated as a constant real number over the spectral range of $E(\omega)$. In this case, the shapes of $\Delta E(t')$ and $E(t')$ in the time domain are essentially identical except for the difference in amplitude and it holds $\Delta E(\omega)/E(\omega) \approx \Delta E(t')/E(t')$.

can be measured at a time t_1 where the decay dynamics have slowed down. After scaling this quantity up by $\Delta\sigma(t_0)/\Delta\sigma(t_1)$ to account for the decay in amplitude, eq. (3.4) can be applied yielding an approximate mobility.

Generally, the time-dependent contribution of photocarrier density and mobility to the photo-conductivity cannot be separated. However, if the photoconductivity spectrum can be analyzed in terms of the Drude model (2.7), the contribution of the mobility can be independently determined from the frequency dispersion. If the mobility cannot be reliably modeled, the influence of mobility changes is usually neglected in practice (though this is somewhat arbitrary).

Throughout this thesis, the THz kinetics are presented as the real part of the photoconductivity (averaged over the reliable frequency range for a better signal to noise ratio), which determines the THz absorption.

3.3 Transient Absorption

Optical TA spectroscopy is very well suited to study the dynamics of molecular systems since electronic transitions within molecules typically occur on an eV scale, so that TA is strongly relied on in the study of the semiconductor/molecule hybrid systems presented in chapter 5. The TA setup that was employed for this thesis has been described in detail in previous work.[32,33,40] Briefly, the fundamental 800 nm beam is split into a pump and a probe branch. Probe pulses are derived from a white light continuum, which is generated by focusing the fundamental 800 nm pulses into a sapphire crystal. Optical pump pulses are generated in either of two NOPA's. The first NOPA yields near infrared (NIR) pulses which are frequency doubled in a BBO crystal to give pump pulses around 425-450 nm wavelength, which comprises the center of the ground state absorption of the molecular absorbers in chapter 5. The output of the other NOPA can be tuned in the visible range and was set to 500 nm center wavelength. For autocorrelation measurements of the pump pulses, the two-photon photoconductivity of a SiC photodiode is utilized.

The measured signal in TA is the pump-induced probe-intensity transmission change ΔT. As long as the excitation is weak ($\Delta T/T \ll 1$), the absorption and the transmission change are proportional to the number of photoexcited species. The transmitted probe light and the differential absorption are measured with a monochromator, a photodiode, and a lock-in amplifier by chopping the probe and the pump light, respectively. To acquire the differential absorption as a function of wavelength and pump-probe delay, the whole WLC is used as the probe. In this case, the cross correlation of the NOPA pump pulses and the WLC, as measured on a rutile single crystal, is generally < 100 fs. The rutile crystal is also used to measure the wavelength-dependent temporal dispersion of the WLC, which is necessary to calibrate the origin of the pump-probe delay at different wavelengths. For certain chosen wavelengths, the time dependence of the differential ab-

sorption is probed with a better time resolution of less than 50 fs which is achieved by cutting out a part of the WLC and compressing with a pair of prisms.

All TA experiments are conducted in a UHV chamber with a base pressure of about 10^{-9} mbar.

3.4 Photoelectron Spectroscopy

Photoelectron spectroscopy is a technique where electrons are removed from the surface region of a material by photons and their kinetic energy is measured. From the kinetic energy spectra and the pump photon energy, it can be concluded on the binding energy of the states from which the electron is removed. If these states are core states, it can also be concluded on the chemical element.
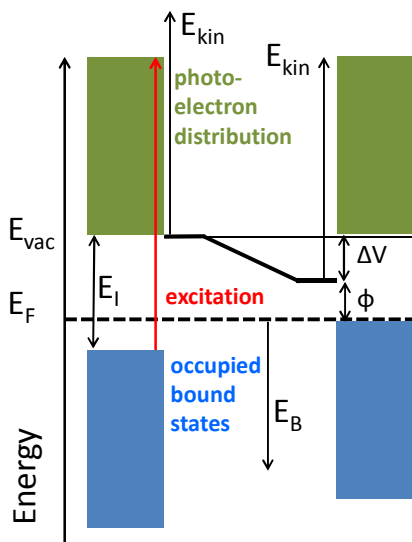

Figure 3-3 Energetic scheme of a photoelectron experiment on a semiconductor. The chemical potential is indicated by the dashed line. The vacuum level, i.e. the zero of the kinetic energy scale of unbound electrons is indicated by the thick line. The difference of the vacuum levels at the sample and at the detector is denoted with ΔV and ϕ refers to the detector work function. The Fermi level is the same for sample and (electrically connected) detector and represents a reference point for the kinetic energy scale.

The principle of photoelectron spectroscopy is depicted in Figure 3-3. Photon absorption invokes electronic transitions from bound states into unbound states outside of the material. Depending on the photon energy, one distinguishes between ultraviolet (UPS) and x-ray photoelectron spectroscopy (XPS). Owing to the photon energy, UPS is limited to the valence states, while XPS can also probe deeper lying core states.

The maximum kinetic energy E_{kin} of photoelectrons just outside of the sample is the difference between the pump photon energy $\hbar\omega$ and the ionization energy E_I. The energy of electrons with zero kinetic energy is the so called vacuum level, which is just the position dependent potential energy of an electron. The vacuum level is generally different at the sample and at the detector due to several effects: The vacuum level depends on the sample surface and is also influenced by

adsorbants.[41] Also, charge is transferred between sample and detector upon electrical contact in order to equilibrate the Fermi levels. The resulting contact potential relatively shifts the vacuum levels. In principle, the vacuum level at the sample may be lower than at the detector. However, one usually applies a voltage to shift the vacuum level at the sample above the detector vacuum level, so that photoelectrons are driven to the detector by the electric field. This guarantees that all photoelectrons reach the detector and at the same time, separates the kinetic energy spectrum of the photoelectrons from secondary electrons generated in the detector. The kinetic energy spectrum at the detector is shifted to higher energies relative to the (hypothetical) spectrum just outside of the sample by the difference in the vacuum levels. Since the Fermi level of the detector is a fixed reference point with respect to the measured kinetic energy, the binding energy E_B can be calculated as

$$E_B = \hbar\omega - E_{kin} - \phi. \tag{3.5}$$

The absolute value of the detector work function ϕ can be inferred from a calibration measurement with a metal sample.

Details on the UPS/XPS apparatus can be found in ref. 42. Briefly: UPS measurements are conducted using the 21.22 eV photons from helium discharge (HE I line). The detector work function is calibrated with a gold sample. For the measurement of the work function, a bias voltage of 2 V is applied, raising the sample vacuum level by 2 eV relative to the detector vacuum level. Hence, using (3.5) the detector work function follows from the binding energy of the secondary electron cutoff as $\phi = \hbar\omega - 2\text{eV} - E_{B,\text{cutoff}}$. XPS measurements are performed with the 1486.6 eV photons from a Al K$_\alpha$ source. All UPS and XPS experiments are conducted in a UHV chamber at pressures of about $2\cdot10^{-8}$ mbar and $3\cdot10^{-10}$ mbar, respectively.

3.4.1   Time Resolved 2PPE

In 2PPE, two optical pulses hit a sample with a certain time delay and the kinetic energy spectrum of photoemitted electrons is analysed. The optical pulses can have different center wavelengths, but it is required that the photon energy of each pulse does not exceed the work function. Ideally, electrons are not emitted when only one pulse hits the sample. In practice, a stationary background signal due to unintended one photon photoemission (1PPE) needs to be discarded. Apart from this 1PPE signal, electrons are excited from initially populated states into empty final states above the vacuum level either through virtual states[43] or through real interstages,[v] which are temporarily populated by the first and depopulated by the second pulse (Figure 3-4). The initial

---

[v] In the context of 2PPE the interstages are called intermediate states. In this thesis, the term intermediate state is also used in the discussion of heterogeneous electron transfer. For clarity, the intermediate state in the 2PPE process is denoted with a different word.

states may, for instance, be valence band states and the interstages can be e.g. conduction band or surface states. While 1PPE gives a stationary background independent of the time delay between pump and probe pulse, time-resolved 2PPE provides information on the transient population of the interstages. The population of the interstages changes because of electron scattering, i.e. the electrons relax energetically or escape into the bulk from where they cannot be emitted anymore. A change of the interstage population has an impact on the kinetic energy spectrum. However, the kinetic energy spectrum cannot be interpreted as a copy of the interstage density of states because, thinking of Fermi's golden rule, the former is also determined by the DOS of the final states and the transition matrix elements.
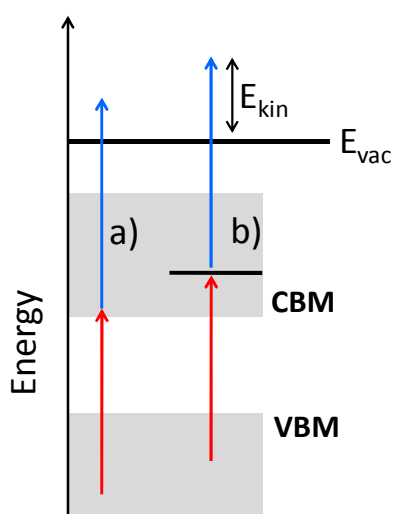
Figure 3-4 Energetic scheme of a 2PPE experiment. The scheme exhibits two examples of 2PPE through interstages. Transition a) represents the case of a broad DOS for initial state and interstage e.g. valence respectively conduction band states. Transition b) corresponds to a situation where the interstage has a rather sharp DOS distribution. This could for example be the case for a surface or image potential state. A discrimination between a) and b) is possible by a variation of the photon energy.

To conduct 2PPE measurements, the fundamental 800 nm pulses are split into two branches by a 15/85 beam splitter. The stronger branch is used to operate a NOPA (I) whose tunable output is set to 500 nm and serves as the sample pump branch.[VI] The remaining 400 nm pulses from the SHG in NOPA I, which have not been used up in the amplification process, are used as the pump beam in the second NOPA (II). The WLC pulses for NOPA II are generated using the weaker 15 % branch of the fundamental 800 nm light. NOPA II yields an independently tuneable spectrum in the visible range, which is set to about 2.3 eV photon energy. A detailed scheme of these series connected NOPAs is laid out in ref. 44. The output of the second NOPA is frequency-doubled in a BBO crystal to generate 4.5 eV probe pulses. Visible pump and UV probe pulses are each compressed with prism pair compressors giving a time resolution of less than 70 fs (cross-correlation). The kinetic energy of the photoemitted electrons is measured with a time of flight spectrometer. To ensure that all photoemitted electrons reach the detector, a positive bias voltage of 1.1 V is applied to the detector.

[VI] A discrimination between pump and probe pulse is of course not meaningful for monochromatic 2PPE.

4 Charge Separation through Defect States in Core/Shell Nanorods

This chapter focuses on the photocarrier dynamics in ZnO nanorods with ultrathin In$_2$S$_3$ absorber shells. Solar cells based on this radial heterojunction design have recently shown promising solar conversion efficiencies. By means of OPTP spectroscopy, the charge separation across ZnO/In$_2$S$_3$ interfaces is analyzed for ZnO nanorods with systematically varied In$_2$S$_3$ absorber thicknesses. While the photoconductivity rapidly decays in neat In$_2$S$_3$ films, the ZnO/In$_2$S$_3$ heterostructures exhibit slow electron injection dynamics occurring within hundreds of picoseconds, and long-lived charge-separated states. The dynamics in the absorber are interpreted as fast (multiple) trapping and second order recombination. The transient photoconductivity of the ZnO/In$_2$S$_3$ core/shell system is analyzed with a correlated three component effective medium approach, yielding a significant decrease of the charge separation efficiency with increasing shell thickness.

4.1 Motivation

The use of nanostructures, and in particular nanorods, as building blocks for solar cells has gained a tremendous interest in recent years. The coaxial design with core/shell nanorods is especially interesting because the charge carrier extraction does not rely on percolation paths as it is the case for a colloidal electrode. Inspired by the nanoparticle dye cell of Grätzel[5] an (ideally abundant and low cost) absorber is deposited on a nanostructured electrode. This absorber may consist of nanocrystals, or quantum dots, or alternatively radial heterojunctions are formed by growing thin layers of semiconductor materials of different bandgap and doping onto a nanorod array.[I] The general advantage of this design is the additional degree of freedom introduced by the three-dimensional nanorod structure that allows using very thin semiconducting layers while maintaining full light absorption. In essence, it means decoupling the optical absorption from the diffusion length of the light absorbing material. Principally, this should reduce the material requirements regarding charge carrier lifetime and transport properties. Hence, it should enable the use of low

---

[I] Early attempts were known as the "extremely thin absorber" solar cell.[45] Now this concept is rather referred to as, "semiconductor sensitized" or "quantum dot sensitized" solar cell.

cost and abundant materials or production techniques with less constraints on the structural and chemical quality.

There are numerous studies on the charge separation in these nanostructured systems. The heterogeneous electron transfer occurring in dye cells has been extensively studied with TA spectroscopy,[46] and a few studies have also addressed this problem with OPTP spectroscopy.[47–50] A similarly active field of research is the electron transfer from quantum dots to metal-oxide semiconductors, which has also been addressed by TA and OPTP spectroscopy.[51] The concepts of dye and quantum dot sensitized solar cells have in common that the absorber consists of isolated units and the interaction of these units is therefore weak. Accordingly, spatial transport prior to charge separation is of little importance in these cells, whereas it is of fundamental importance for solid semiconductor absorber shells on ZnO nanorods (Figure 4-1).
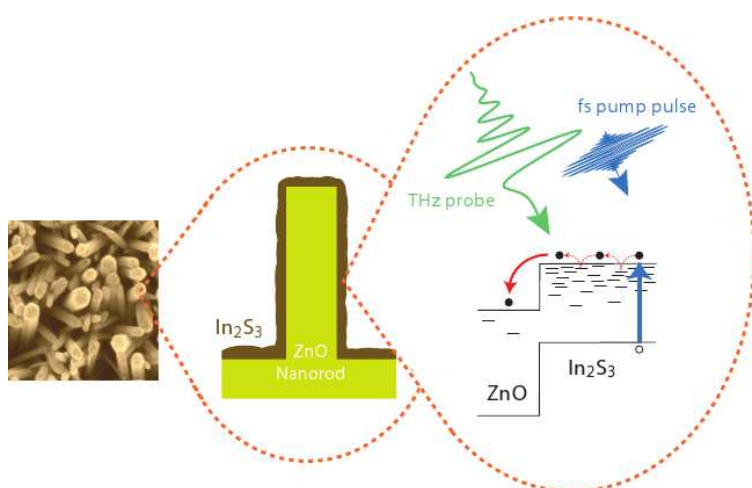

Figure 4-1 Scheme of the probed system and its dynamics. ZnO nanorods are coated with an indium sulfide thin film, which acts as a light absorber. Upon illumation charge carriers migrate to the ZnO electrode, get trapped or recombine. All these processes change the overall conductivity and can therefore be detected by OPTP.

Many different semiconductor absorber shells have been tested on ZnO nanorod electrodes: For instance the sulfides Sb_2S_3,[52] CdS,[53] and In_2S_3,[4] and classical thin film solar cell materials like $CuInS_2$,[54] $CuInSe_2$,[55] $CdSe$,[56] $CdTe$,[57] and also amorphous silicon[58]. A promising energy conversion efficiency of 4.17 % (at air mass 1.5) has been demonstrated for cells based on $ZnO/In_2S_3/CuInS_2$ core/shell nanorods.[54] Similar prototypical solar cells, where ZnO nanorods constitute the electrode, In_2S_3 is the light absorber, and CuSCN represents the hole conductor, have been systematically studied in previous works[4,59,60] demonstrated a relatively good power conversion efficiency of 3.4 %.[4] Moreover, the nanorods, the absorber shell, and the hole conductor were all deposited by simple wet-chemical methods. The local absorber thickness was found to be one of the most critical parameters for the cell performance, with a peak in the efficiency between 20 nm and 30 nm. Despite the beneficial effect of a higher light absorption, the short circuit current strongly dropped for thicker absorber layers due to the very short charge carrier diffusion length, which was estimated to be on the order of 10 nm only. However, with an optimal shell thickness exter-

nal quantum efficiencies close to unity have been achieved.[4] Recently, an optical-pump micro-wave-probe study on the radial ZnO/In$_2$S$_3$/CuSCN system identified the charge separation to occur at the ZnO-In$_2$S$_3$ interface,[59] lasting up to milliseconds. However, the low 10 ns time resolution prohibited a direct observation of the charge carrier dynamics in the absorber as well as the charge separation at the ZnO-In$_2$S$_3$ interface. In this chapter, OPTP spectroscopy is employed to enhance the time resolution to sub-ps in order to gain a deeper understanding of the basic processes governing charge separation at the ZnO-In$_2$S$_3$ interface.

4.2 Material Properties

4.2.1   Zinc Oxide

ZnO has been extensively studied with regard to device applications since decades, and comprehensive review articles on its bulk and surface physics have evolved.[61–64] In the field of photovoltaics, ZnO is known for its use as electrodes or window layers due to its 3.3 eV wide direct band gap,[65] which makes it transparent for the major part of the solar power spectrum. Under ambient conditions, ZnO crystallizes in the wurtzite structure (Figure 4-2).[66] The conventional unit cell of the ZnO crystal lattice is spanned by the vectors

$$\vec{a} = a\begin{pmatrix} 1 \\ 0 \\ 0 \end{pmatrix}, \ \vec{b} = a\begin{pmatrix} 1/2 \\ \sqrt{3}/2 \\ 0 \end{pmatrix} \text{ and } \vec{c} = c\begin{pmatrix} 0 \\ 0 \\ 1 \end{pmatrix}, \tag{4.1}$$

with a = 3.25 Å and c = 5.207 Å .[67] The positions of the basis atoms in terms of these vectors are $(\tfrac{1}{3},\tfrac{2}{3},0)$ and $(\tfrac{2}{3},\tfrac{1}{3},\tfrac{1}{2})$ for Zn and $(\tfrac{1}{3},\tfrac{2}{3},u)$, and $(\tfrac{2}{3},\tfrac{1}{3},\tfrac{1}{2}+u)$ for O, with $u = 0.3817$.[67] Each of the sublattices of the Zn and O atoms is a hexagonal closed package structure with ABAB... stacking sequence, and both sublattices are relatively shifted by $u{\cdot}c$ along the principal c-axis. As a result, every Zn or O atoms is tetrahedrally coordinated by atoms of the other kind.

ZnO usually exhibits n-type conductivity unless efforts for growing it p-type are made. The native n-type conductivity probably does not stem from intrinsic point defects but has to be attributed to chemical impurities[63,68] such as group III elements and hydrogen. Hydrogen may not only form a shallow bulk donor but can also induce surface metallicity, i.e. electrons accumulate so massively at the surface that the CBM is pushed below the Fermi level.[69–71] Electron accumulation layers at ZnO surfaces may be as thin as a few nanometers and contain quantized 2D localized metallic sub-bands in the potential well between the bulk CBM and the vacuum level.[72,73]
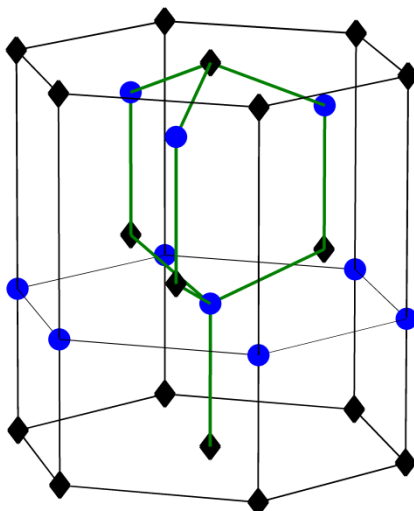
Figure 4-2 Hexagonal unit cell of ZnO. Black diamonds indicate the positions of Zn^{2+}, and blue circles show the positions of O^{2-}.

Another interesting property of the ZnO surface physics in connection with photons is the occurrence of persistent photoconductivity (PPC).[II] PPC was reported in several studies on ZnO.[74–82] Though most studies used UV, light the occurrence of PPC has also been reported after illumination with sub-bandgap light.[80,81] A convincing explanation for this phenomenon is that adsorbed oxygen traps electrons but releases them after photoexcitation.[76] It was proposed that this goes along with a desorption of the oxygen and that even lattice oxygen can be desorbed.[77] This model is supported by the observation that oxygen atmosphere leads to (an accelerated) PPC decay and restores the dark conductivity.[74,75,77,83] In one study, desorbed O_2 could be detected after illuminating ZnO in UHV[84] while in another study, CO_2 was the photodesorbed species.[85] In accordance with the latter observation, Bao et al. suggested that adsorbed hydrocarbons catalyze the removal of lattice oxygen after photoexcitation.[77] Regarding the core/shell nanorods such a desorptive charging of the nanorods should not occur because the shell encapsulates the shell.

4.2.2   Indium Sulfide

In_2S_3 has by far not received as much attention by researchers as ZnO. It has mostly been investigated as a potential replacement for the routinely used but highly toxic CdS in $Cu(In,Ga)(S,Se)_2$ solar cells and is currently regarded as one of the most promising alternative buffer layers.[III,86] Studies on its transport and optoelectronic properties are scarce. Reported values for the mobility

---

[II] PPC refers to the phenomenon that the conductivity does not relax to the dark value when the illumination is switched off but remains at an elevated level for hours or days.

[III] With respect to solar cells, the term 'buffer layer' refers to a coating that reduces surface recombination.

range from 5 to 100 cm^2/Vs,[87,88] and an experimental estimation of the electron effective mass is given as $m^* \lesssim m_e$.[89] Optical absorption measurements indicate that β-In_2S_3 has an indirect bandgap of 2.2 eV.[90] This is also supported by recent DFT band structure calculations, which show that the CBM and VBM are located at the Γ respectively the N point,[91] and the effective electron/hole mass is found to be 0.162/0.470 m_e.

At room temperature In_2S_3 crystallizes in its β phase, which has a spinel structure and contains four ordered vacancies[IV] of the In cation per unit cell.[92,93] The amount of disorder even in perfectly stoichiometric In_2S_3 can assumed to be high because the antisite defect where In from a regular cation site occupies a regular lattice vacancy should have a low formation energy.[87] Irregular cation vacancies and occupied lattice vacancies are regarded as acceptors and donors, respectively. This implies that In_2S_3 may be highly compensated.

4.3 Preparation and Structural Properties

The preparation procedure of the ZnO nanorods is based on the routine of Peterson et al.[94] and described in detail in ref. 95 together with the deposition of the In_2S_3 absorber layers. In brief: A 40 nm thick ZnO seed layer is deposited on [0001] oriented quartz substrates whereupon ZnO nanorods are grown by chemical bath deposition (0.4 M NaOH and 0.01 M $ZnNO_3$ at 80 °C). Such prepared nanorods grow as hexagonal crystals elongated along the c-axis.[94] Figure 4-3 (a) and (b) give an impression of the nanorod morphology. After annealing the samples at 450 °C for 30 min, In_2S_3 absorber layers are put on some of the nanorod samples by a spray ion layer gas reaction (spray-ILGAR) process.[96] The solution for this process contains 0.025 M $InCl_3$, and the sulphurization is done at 200 °C in H_2S diluted with Ar (Ar/H_2S = 95/5). The local absorber thickness can be adjusted by the number of spray-ILGAR cycles. Four samples with 10, 20, 30, and 60 spray-ILGAR cycles were prepared from the same batch of ZnO nanorods. Additionally, planar In_2S_3 layers were grown on quartz to separately examine the charge carrier dynamics in the absorber. TEM micrographs indicate that the planar layers are nanocrystalline with domains on the order of 10 nm (Figure 4-3 (c)).

Table 2 Average shell thickness and fill factor of the core/shell nanorods.

Spray-ILGAR cycles	10	20	30	60
Shell thickness [nm]	4.2	6.3	8.9	16.7
Fill factor	0.3	0.33	0.38	0.53

[IV] This means that the vacancies are part of the crystal lattice instead of being distributed randomly.
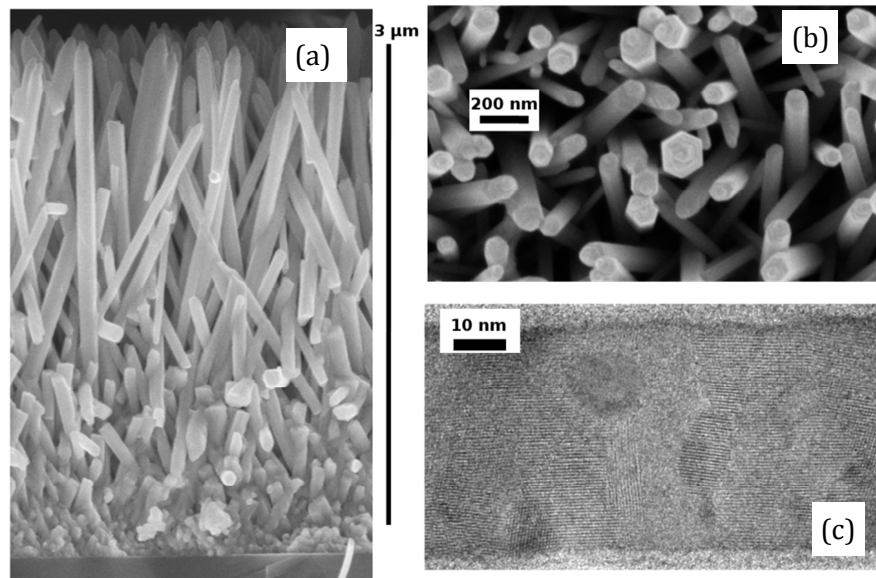
Figure 4-3 (a) SEM side view of uncoated ZnO nanorods. (b) SEM top view of uncoated ZnO nanorods. The chemical bath deposited rods grow non-uniformly with a hexagonal symmetry. (c) TEM micrograph of an In_2S_3 thin film. Crystalline domains of about 10 nm size can be seen.

The length and diameter of the uncoated nanorods are determined from scanning electron microscope (SEM) images and found to be 2.2 μm and 60 ± 20 nm, respectively, with an areal density of $7 \cdot 10^9$ cm^{-2}, and a nanorod volume fill factor of 0.24. This nanorod density yields a surface magnification of roughly 30 compared to a planar electrode. To determine the mean shell thickness of the coated nanorods the fill factor of the coated core/shell nanorods is estimated from SEM images. The mean shell thickness is then obtained as the mean increase d_s of the radii of the uncoated nanorods that yields the same fill factor as that measured on coated samples (Table 2). This gives more accurate results than measuring the increase of the mean diameter because close standing nanorods are hardly distinguishable after coating.

4.4 Electro-Optical Characterization

This section lays the basis for the analysis of the dynamics in the core-shell rods in section 4.5. The optical absorption coefficient of bare ZnO nanorods, core/shell nanorods, and In_2S_3 thin films is derived from steady-state optical absorption measurements, and allows concluding on the excitation density. Analysis of the photoconductivity of nanostructures requires an effective medium approach (EMA). Hence, the Bruggemann EMA is presented and extended to the case of core/shell nanorods. Thereafter, the In_2S_3 and ZnO nanorod mobility is evaluated (using the EMA for the latter), which is essential to know for the interpretation of the dynamics in the coated nanorods.

4.4.1   Optical Properties

The optical transmittance T and reflectance R of the samples are measured using a Perking-Ellmer Lambda35 spectrometer with a Labsphere integrating sphere. The absorbance (1 - R – T) is depicted in Figure 4-4, and it correlates well with the absorber coating thickness. The thickest shell layer shows close to 100 % absorption below the ZnO bandgap. This is possible because the reflectance is strongly reduced due to the rather smooth transition of the refractive index from air to the semiconductor-air effective medium.[97] A selective excitation of the absorber shell can be achieved with the 500 nm pump pulses from a NOPA,[v] whereas to excite bare ZnO nanorods and the planar In_2S_3, the 400 nm pulses obtained from SHG are employed.
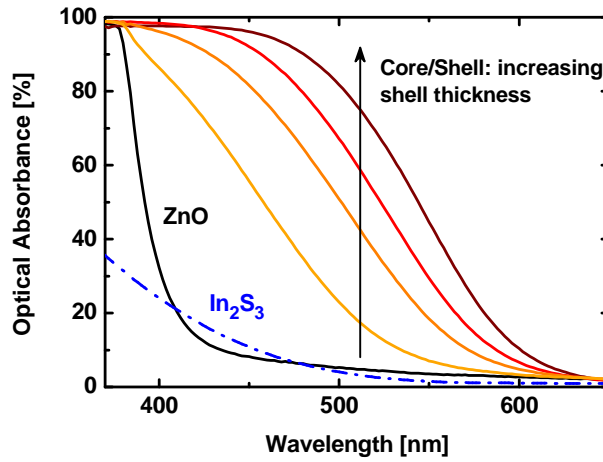

Figure 4-4 Optical absorbance of ZnO nanorods, a planar 50 nm thick In_2S_3 layer (broken line), and ZnO nanorods with 10, 20, 30, and 60 spray-ILGAR cycles of In_2S_3 deposition.

Due to the complicated microstructure and the strong scattering of the nanorod structures, the pump pulse propagation in the nanorod layer is rather complicated. However, there will be a gradient in the absorption, which for simplicity is assumed to result in an exponential excitation profile $\propto e^{-\alpha z}$, so that the absorption coefficient can be estimated as

$$\alpha = -\frac{1}{d}\ln\left(\frac{T}{1-R}\right). \tag{4.2}$$

The squared absorption coefficient of bare ZnO nanorods obtained by this approximation is depicted in Figure 4-5 (a). Since ZnO has a direct band gap, the relation $\alpha^2 \propto \hbar\omega$ holds in the vicinity

---

[v] The remaining ZnO nanorod absorption in the visible range (about 5 % at 500 nm) is an artifact due to scattered light not entering the integrating sphere. This artifact is accounted for by subtracting the ZnO nanorod absorption from the absorption of the core/shell nanorods at 500 nm when the absorption is used for calculations.

of the band gap.[98] From this relation, the band gap can be estimated to be 3.21 eV. This is slightly lower than the reported ZnO single crystal optical band gap of 3.3 eV.[65] A possible explanation is that this is due to defect related absorption. For instance, oxygen vacancies are known to narrow the optical band gap of ZnO.[99] In addition, the sub-bandgap absorption may be enhanced by scattering.
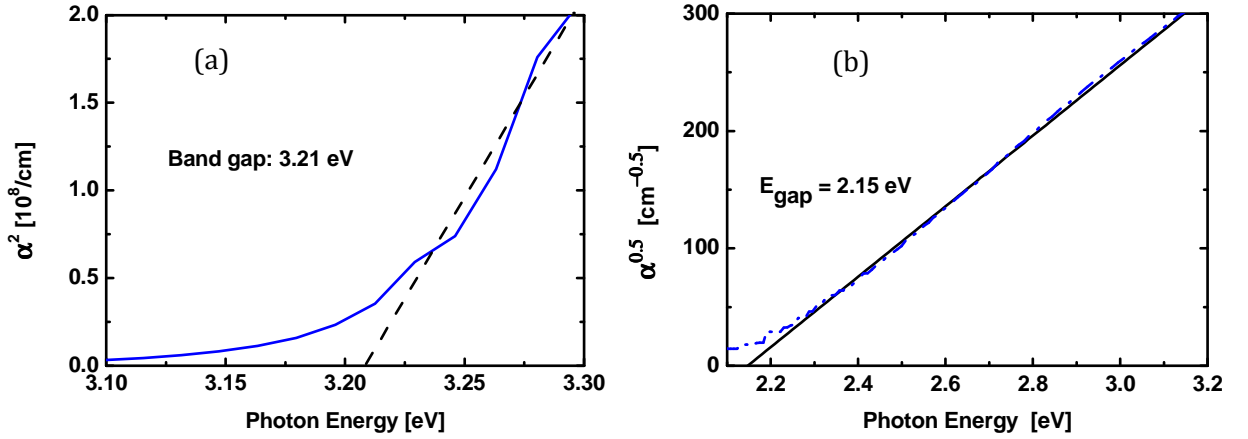

Figure 4-5 (a) Squared absorption coefficient of bare ZnO nanorods (blue). The dashed line designates a bandgap of 3.21 eV. (b) Square root of the absorption coefficient of an In_2S_3 thin film. The linear fit (solid line) demonstrates that the dispersion of the absorption is in agreement with an indirect absorption edge.

The absorption coefficient $\alpha = 4\pi\kappa/\lambda$ of a dense In_2S_3 thin film with thickness d and complex refractive index $n_2 = \eta + i\kappa$ on a substrate with complex refractive index n_3 does not have to be estimated, but can be accurately determined from the measured transmittance T and reflectance R. Let the sample on the substrate be sandwiched between two media with complex refractive indices n_1 and n_4 on the film and on the substrate side, respectively. Then, theoretical expressions for the transmittivity T_t and reflectivity R_t can be derived (cf. section 8.2). Provided the substrate refractive index n_3 is known and the measurement is done in air ($n_1 = n_4 = 1$), then $T_t = T_t(\eta, \kappa, d, \lambda)$ and $R_t = R_t(\eta, \kappa, d, \lambda)$. Hence, the complex refractive index n_2 of the thin film then follows from simultaneously fitting $T_t(\eta, \kappa, d, \lambda)$ to T and $R_t(\eta, \kappa, d, \lambda)$ to R. The absorption coefficient α obtained this way for a thin In_2S_3 film is shown in Figure 4-5 (b). The film thickness as retrieved from the fit is 50 nm,[VI] which agrees remarkably well with the results of the TEM micrographs in Figure 4-3. Using the relation $\sqrt{\alpha} \propto \hbar\omega - E_{\text{gap}}$ for the absorption of an indirect semiconductor[100] (Tauc plot), a

---

[VI] For each wavelength λ, the transmittance T_t and the reflectance R_t depend on η, κ and d. Hence, there are generally many different sets (η, κ, d) which reproduce given values of T_t and R_t. However, if the absorption below the bandgap can be neglected, it is justified to set $\kappa = 0$ which determines η and d uniquely for $\lambda > \lambda_{GAP}$. Hence, η and κ are also determined uniquely for $\lambda < \lambda_{GAP}$, since d is constant.

band-gap of 2.15 eV can be derived from the linear extrapolation of $\sqrt{\alpha}$ to the abscissa. This is close to the reported value of 2.2 eV for the β-In$_2$S$_3$ phase.[90]

Though the absorber is referred to as In$_2$S$_3$, it contains a significant number of foreign atoms. For In$_2$S$_3$ films grown under nominally identical conditions, except for the Ar dilution of the In$_2$S$_3$ gas, Allsop et al. observed over 17 at.% of impurities (mainly hydrogen and chlorine).[96] So it can be expected that the absorber shell has an overall mediocre material quality with a very high level of defects. As mentioned in the beginning, a major idea for the design of nanostructured systems such as the core/shell nanorods is to realize high quantum efficiencies even with low quality absorber materials.

4.4.2 EMA for Core-Shell Rods

The mobilities of planar, solid films can be analyzed by the procedure outlined in section 3.2. In the case of the nanorods, the terahertz pulse probes the photoconductivity $\Delta\sigma$ of the nanorod-air (or vacuum) blend, and an effective medium model has to be taken into account to retrieve the nanorod photoconductivity $\Delta\sigma_r$ from the measured photoconductivity $\Delta\sigma$. Two analytical models are usually employed for this task, the Bruggemann effective medium approach[101] (EMA) and Maxwell-Garnett theory.[102] For the latter model, the fill factor of the most abundant component must be close to unity, which is not fulfilled here since the fill factors vary from 0.24 for bare ZnO nanorods to 0.53 for core/shell nanorods with 60 Spray-IlGAR cycles, so that the Bruggemann EMA is employed. According to the Bruggemann EMA, the effective permittivity $\langle\epsilon\rangle$ of a medium that consists of nanorods with permittivity ϵ_r, which are aligned parallel to the incoming radiation but otherwise randomly dispersed into a matrix with permittivity ϵ_m, is given by

$$f\frac{\epsilon_r - \langle\epsilon\rangle}{\epsilon_r + \langle\epsilon\rangle} + (1-f)\frac{\epsilon_m - \langle\epsilon\rangle}{\epsilon_m + \langle\epsilon\rangle} = 0. \tag{4.3}$$

Here, f denotes the volume fill fraction of the nanorods. The Bruggemann approach can be generalized to an arbitrary number of components as has been outlined by Wood and Ahscroft.[103] In the case of nanorods with a permittivity ϵ_r, where the voids are filled with air, i.e. $\epsilon_m = 1$, solving eq. (4.3) for $\langle\epsilon\rangle$ yields

$$\langle\epsilon\rangle = \frac{1}{2}\left((2f-1)(\epsilon_r - 1) \pm \sqrt{(1-2f)^2(\epsilon_r - 1)^2 + 4\epsilon_r}\right), \tag{4.4}$$

and solving (4.3) for ϵ_r gives

$$\epsilon_r = \frac{\langle\epsilon\rangle^2 + (2f-1)\langle\epsilon\rangle}{1 + (2f-1)\langle\epsilon\rangle}. \tag{4.5}$$

The sign of the square root in eq. (4.4) has to be chosen to obtain a physically meaningful solution. After photoexcitation, the nanorod permittivity changes from its dark value ϵ_r to

$$\epsilon_r^* = \epsilon_r + i\frac{\Delta\sigma_r}{\omega\epsilon_0} \tag{4.6}$$

and the effective permittivity changes from $\langle\epsilon\rangle$ to

$$\langle\epsilon^*\rangle = \langle\epsilon\rangle + i\frac{\Delta\sigma}{\omega\epsilon_0}. \tag{4.7}$$

Provided that ϵ_r is known, the nanorod photoconductivity $\Delta\sigma_r$ can be retrieved from a measurement of the composite photoconductivity as follows. With the help of (4.4) and (4.7), $\langle\epsilon^*\rangle$ is calculated, which then allows to determine ϵ_r^* from (4.5). Finally, $\Delta\sigma_r$ follows from (4.6) as

$$\Delta\sigma_r = \frac{-i}{\epsilon_0\omega}\left(\frac{(2f-1)\langle\epsilon^*\rangle + \langle\epsilon^*\rangle^2}{1 + (2f-1)\langle\epsilon^*\rangle} - \epsilon_r\right). \tag{4.8}$$

By a similar scheme, the effective photoconductivity $\Delta\sigma$ can be derived if the intrarod conductivity is known.

The Bruggemann EMA is suitable to analyze the effective photoconductivity of nanorods. However, in the case of core/shell nanorods, eq. (4.3) cannot simply be extended to three components. In fact, a correlated three component effective medium approach[103] has to be taken into account because the core and the shell are not independently dispersed. This task can be achieved by calculating the mean permittivity $\langle\epsilon_{cs}\rangle$ of the core/shell nanorods as[VII]

$$\langle\epsilon_{cs}\rangle = \frac{\int\epsilon\mathbf{E}\,d\mathbf{r}}{\int\mathbf{E}\,d\mathbf{r}} \tag{4.9}$$

and using it for ϵ_r in eq. (4.3)-(4.5). Here, the integration runs over the volume occupied by the core/shell nanorod and E denotes the electric field. So starting with eq. (4.9) the mean permittivity of the core/shell nanorods is written as

$$\epsilon_r := \langle\epsilon_{cs}\rangle = \frac{f_c\epsilon_c\langle E_c\rangle + f_s\epsilon_s\langle E_s\rangle}{f_c\langle E_c\rangle + f_s\langle E_s\rangle}. \tag{4.10}$$

[VII] This expression has been originally given by Wood and Ashcroft as a way to calculate the effective permittivity.[103] In the case of randomly dispersed nanorods, it yields the same results as the Bruggemann EMA in eq. (4.4). This can be seen by assuming that both, the nanorods and the surrounding medium are made up of cylinders. Then the electric field $E_{in} = 2\epsilon_{out}/(\epsilon_{in} + \epsilon_{out})\cdot E_{out}$ within each cylindrical domain is expressed by assuming that the permittivity and the electric field outside the domain are given as the effective permittivity respectively the mean field, so $E_{in} = 2\langle\epsilon\rangle/(\epsilon_{in} + \langle\epsilon\rangle)\cdot\langle E\rangle$. Now (4.9) can be solved for $\langle\epsilon\rangle$.

Here, the indices c and s refer to the core and the shell, respectively, and the angle brackets $\langle\rangle$ denote the spatial average. To retrieve the electric field in the core and the shell in dependence of the applied field it is assumed that the applied field is oriented perpendicular to the nanorods, as it is also the case in the OPTP experiments. It greatly simplifies the problem if the finite extension of the nanorods is neglected, i.e. it is assumed that the electric potential does not change along the cylinder axis. In this case, the general solution of the two-dimensional Poisson equation in polar coordinates $(\rho = \sqrt{x^2 + y^2}, \phi)$

$$\rho \frac{\partial}{\partial \rho}\left(\rho \frac{\partial \phi}{\partial \rho}\right) + \frac{1}{\rho^2}\frac{\partial^2 \phi}{\partial \phi^2} = 0 \tag{4.11}$$

can be easily derived by separation of variables and is generally given as the series

$$\phi(\rho,\varphi) = \sum_{l=0}^{\infty}\left(\alpha_l \rho^l + \beta_l \rho^{-l}\right)\cos(l\cdot\varphi) + \left(\gamma_l \rho^l + \delta_l \rho^{-l}\right)\sin(l\cdot\varphi). \tag{4.12}$$
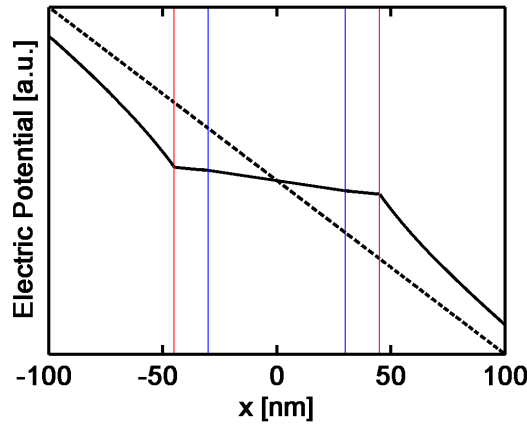

Figure 4-6 This scheme depicts how the potential of a uniform electric field (broken line), which is applied along the x-axis, changes when a core/shell nanorod is placed into the field, with the cylinder axis perpendicular to the field axis. The values for the permittivities of the core and the shell were chosen as those of ZnO and In$_2$S$_3$, respectively. The blue lines indicate the diameter of the core (60 nm) and the red lines indicate the shell thickness (15 nm).

In the core, (4.12) is directly simplified to $\beta_l = 0 \ \forall \ l \neq 0$ owing to the demand for a non-singular potential at $\rho = 0$. The applied electric field outside of the nanorod can be chosen parallel to the x-axis, so the electric potential far away from the nanorod can be written as $\phi_a = -E_0\rho\cos(\phi)$. From the boundary conditions at the core/shell, and the shell/vacuum interface, and the asymptotic behavior of the potential for $\rho \to \infty$, the coefficients in eq. (4.12) can be determined. This has been performed for the most general case of an arbitrary electric field by Nicorovici, McPhedran and Milton in ref. 104. Using their solution the potential in the shell reads

$$\phi_s = \alpha_1^s \rho \cos(\varphi) + \beta_1^s \frac{\cos(\varphi)}{\rho}, \tag{4.13}$$

whereas in the core it is given by

$$\phi_c = \alpha_1^c \cdot \rho \cos(\varphi), \tag{4.14}$$

with the abbreviations

$$\alpha_1^s = \frac{2\epsilon_m(\epsilon_c + \epsilon_s)r_s^2}{(\epsilon_c - \epsilon_s)(\epsilon_s - \epsilon_m)r_c^2 + (\epsilon_c + \epsilon_s)(\epsilon_s + \epsilon_m)r_s^2} E_0$$

$$\beta_1^s = \frac{2\epsilon_m(\epsilon_c - \epsilon_s)r_c^2 r_s^2}{(\epsilon_c - \epsilon_s)(\epsilon_m - \epsilon_s)r_c^2 + (\epsilon_c + \epsilon_s)(\epsilon_s + \epsilon_m)r_s^2} E_0 \tag{4.15}$$

$$\alpha_1^c = \frac{4\epsilon_m\epsilon_s r_s^2}{(\epsilon_c - \epsilon_s)(\epsilon_s - \epsilon_m)r_c^2 + (\epsilon_c + \epsilon_s)(\epsilon_s + \epsilon_m)r_s^2} E_0.$$

Here, ϵ_m and E_0 are the permittivity and the electric field outside the nanorods. Figure 4-6 demonstrates how the electric potential is changed in the presence of a core/shell nanorod. To a good approximation, the potential inside the nanorod is linear in the direction of the applied field (x-axis). The integrals of the components of the electric field perpendicular to the x-axis ($E_y = -\partial\phi/\partial y$) over the core and the shell vanish. Only the components parallel to the x-axis contribute to $\langle E_c \rangle$ and $\langle E_s \rangle$, with the simple result of $\langle E_c \rangle = \alpha_1^c$ respectively $\langle E_s \rangle = \alpha_1^s$, which when inserting into (4.10) yields

$$\epsilon_r = \frac{(\epsilon_c - \epsilon_s)\epsilon_s r_c^2 + \epsilon_s(\epsilon_c + \epsilon_s)r_s^2}{(\epsilon_s - \epsilon_c)r_c^2 + (\epsilon_c + \epsilon_s)r_s^2}. \tag{4.16}$$

This the expression for the effective core/shell rod permittivity, which can now be used in the standard two component Bruggemann EMA in eq. (4.3).

4.4.3 Transport Properties

The ZnO intra-rod mobility, obtained from a measurement of the effective conductivity and the procedure outlined in the last section,[VIII] is depicted in Figure 4-7. In comparison, also the mobility of a planar In$_2$S$_3$ thin film is shown. For both, ZnO nanorods and planar In$_2$S$_3$, the mobility is predominantly real and slightly increases with frequency while the small imaginary part is negative and decreases. This behavior strongly deviates from the typical Drude-conductivity that can

---

[VIII] The ZnO single crystal permittivity[105] was used for the dark permittivity ϵ_r of the nanorods. Interestingly, the photoconductivity of the ZnO nanorods as obtained from eq. (4.8) and the effective conductivity of the nanorod/air composite have the same spectral shape, but the magnitude of the intra-rod conductivity is higher by a level of about 30.

be found in ZnO single crystals[106,107] and ZnO thin films grown by chemical vapor deposition.[108] However, this behavior agrees with the results of previous studies on ZnO nanorods, nanoparticles, or chemical bath deposited thin films[48,109,110] and is generally regarded as a sign of carrier localization (cf. section 2.1, ref. 111). The non-Drude spectra in Figure 4-7 can be well fit by the Drude-Smith model,[11] where the mobility reads

$$\mu_{DS} = \frac{e\tau_{DS}}{m^*} \cdot \frac{1}{1-i\omega\tau_{DS}} \left(1 + \frac{c_1}{1-i\omega\tau_{DS}} \right).$$

(4.17)

In the Drude-Smith model, τ_{DS} is the average time between electron scattering events and c_1 is the so-called 'backscattering factor', which describes the average fraction of an electrons velocity that is retained in a scattering event. The backscattering factor c_1 can be used to tune the spectrum from Drude-like ($c_1 = 0$) to maximally localized ($c_1 = -1 \rightarrow \mu_{DS}(\omega=0)=0$).
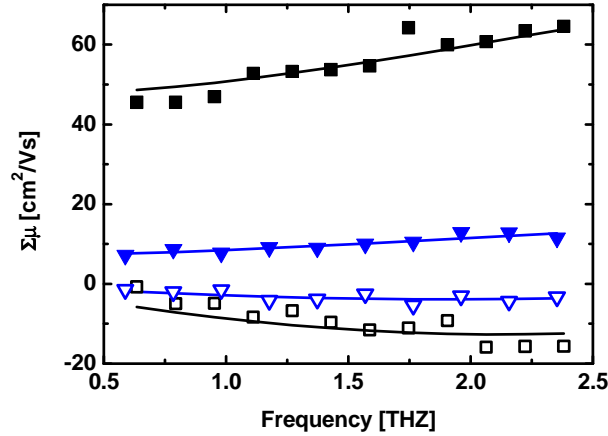

Figure 4-7 Spectra of the ZnO intra-rod mobility (squares, measured in air) and the mobility of a dense In_2S_3 film (triangles). Filled/open symbols denote the real/imaginary part of the mobility. Solid lines are fits with the Drude-Smith model. The photogenerated electron-hole density n_{eh} is on the order of 10^{16} cm^{-3} and 10^{18} cm^{-3} for ZnO and In_2S_3, respectively.

In Smith's original publication this model was not rigorously justified apart from its 'empirical performance and versatility'. Recently however, a physical justification of the Drude-Smith model, which is based on the influence of grain/crystallite boundary scattering, was given by Němec et al.[110] Their model is centered on ensemble Monte Carlo simulations of charge carrier trajectories: After a mean time τ_D, a scattering event occurs and the carrier velocity is randomized according to a Maxwell-Boltzmann distribution.[IX] The effect of grain/crystallite boundaries is simulated by assuming that the charge carrier is reflected at the boundary with a certain probability p_r. By making use of the Kubo formula, the frequency dependent mobility is then retrieved from a Fou-

---

[IX] In the model of Němec et al. the mean scattering rate coincides with the momentum relaxation rate.[110]

rier transform of the velocity autocorrelation. As a result, Drude mobility occurs for vanishing grain boundary scattering but if grain boundary scattering is taken into account, the mobility can be modeled with eq. (4.17) and a negative value for c_1. This model has been successfully applied to simulate the mobility of nanocrystalline CdS, ZnO and TiO_2.[48,110,112] The influence of the grain boundaries depends on the ratio α of particle/grain diameter d and thermal mean free path l_{th}. According to Němec et al., α and the backscattering probability p_r can be roughly linked to the parameters of the phenomenological Drude-Smith model by the empirical equations

$$\tau_{DS} = \frac{\alpha}{2+\alpha}\tau_D \quad \text{and} \quad c_1 = -\frac{p_r}{1+\alpha/20}. \tag{4.18}$$

The Drude-smith scattering time τ_{DS} is smaller than the bulk scattering time τ_D because of the additional scattering at the boundaries. Using eq. (4.17) to fit the mobility of In_2S_3 in Figure 4-7 yields $\tau_{DS} = 29$ fs, $c_1 = -0.78$, and $m^* = 1.61\,m_e$, which is in agreement with a published estimate of the effective mass.[89] Since $\alpha > 0$, (4.18) states that $p_r > 0.78$, and the long range transport (DC mobility) is hindered by a factor of at least 4. From (4.18) and $l_{th} = \sqrt{3k_BT/m^*}\,\tau_D$ it follows that the mean grain size is between 6 nm and 20 nm, depending on the backscattering probability p_r. This value is in good agreement with the grain size observed in the SEM micrographs (Figure 4-3). Fitting the ZnO nanorod mobility with eq. (4.17) yields $\tau_{DS} = 24$ fs, $c_1 = -0.7$, and $m^* = 0.26\,m_e$, which coincides with literature values of the conduction band effective mass of about $0.24\,m_e$.[113,114] The nanorods are mostly isolated and therefore the boundaries must have a high backscattering probability ($p_r \approx 1$). Although (4.18) was derived for the case of spherical nanoparticles, application on nanorods gives a mean particle size of 57 nm which is close to the mean diameter of 73 nm measured for the sample from Figure 4-7. The mobility spectra of ZnO and In_2S_3 have no distinct 'fingerprint' features and their spectral shape is very similar. Hence, the charge separation analysis cannot be based on the spectral data but rather on the dynamics in the time domain.

4.5 Charge Carrier Kinetics

This section deals with the charge separation process in the core/shell nanorods. First, the charge carrier dynamics in bare In_2S_3 thin films are investigated and described in terms of a multiple trapping model. Thereafter, the transient photoconductivity of ZnO/In_2S_3 core/shell nanorods is examined and simulated with a correlated three component effective medium approach, which allows drawing conclusion on the charge separation kinetics and the injection efficiency.

4.5.1 Dynamics in the Bare Absorber

The transient photoconductivity of In_2S_3 exhibits a non-exponential decay behavior (Figure 4-8). A rapid decrease within the first few picoseconds is followed by a much slower, strongly decelerating decay over hundreds of picoseconds. In the accessible range of the excitation density n_{eh}, the fast decay process is independent of the photocarrier density and the peak conductivity is proportional to the pump fluence as shown in Figure 4-8 (a). However, Figure 4-8 (b) demonstrates that the fast decay component is very much affected by the temperature and becomes increasingly dominating for low temperatures. The linearity of the early-time photoconductivity signal with the pump fluence in the time window below 20 ps directly allows to exclude radiative and Auger recombination on this timescale. These processes are nonlinear, so that the recombination rate is rapidly amplified once the photocarrier density surmounts the equilibrium carrier density, and in the weak excitation limit these processes would exhibit an exponential charge carrier decay.
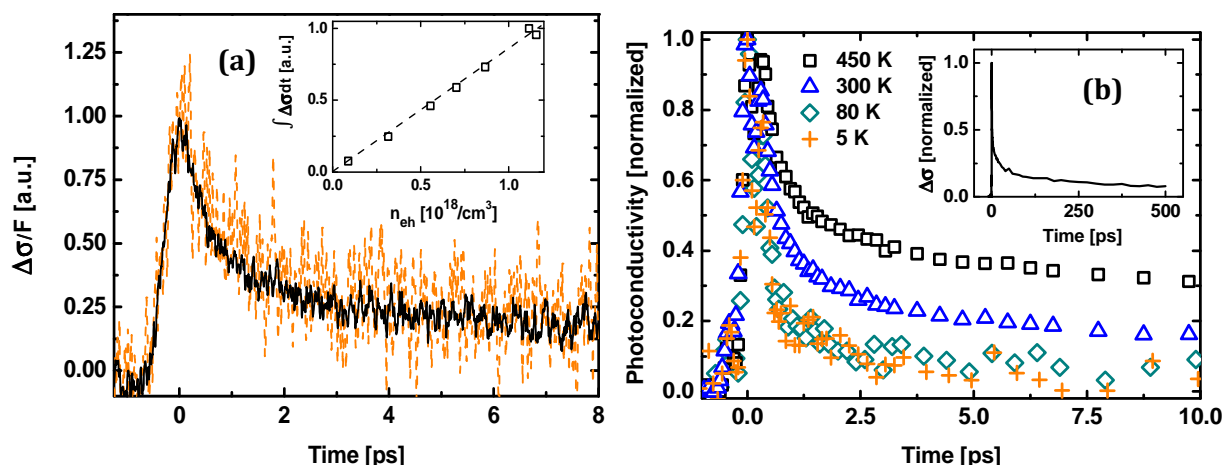

Figure 4-8 (a) Early time photoconductivity decay in In_2S_3 normalized to the pump fluence F for excitation densities n_{eh} of 10^{17} cm^{-3} (broken line) and $1.1 \cdot 10^{18}$ cm^{-3} (solid line). The kinetics is identical, and the inset demonstrates the linear scaling of the photoconductivity with the pump fluence. For a better S/N ratio, the integral of the conductivity within the first 10 ps is shown. (b) Temperature dependent change of the fast decay component. The inset depicts the subsequent slow decay at room temperature.

Regarding the question which mechanism is responsible for the fast ps conductivity decay, also a recombination of electrons and holes via defect related band-gap states (Shockley-Read-Hall recombination[115]) can be ruled out. If the decay was due to electron-hole recombination, the majority of photocarriers would have recombined after just a few ps. However, the charge separation process in ZnO/In_2S_3 core/shell nanorods turns out to proceed over hundreds of ps (section 4.5.2), and the external quantum efficiency of the complete solar cell can be close to unity. It is not comprehensible how this was possible if the charge separation would have to compete with much faster charge recombination. Therefore, it stands to reason that the origin of the fast decay is a

capture of carriers into shallow traps, so that emission back into the band is likely and the carriers are not yet ultimately lost. Alternatively, it is conceivable that the fast initial dynamics are dominated by a rapidly changing mobility due to the cooling of hot carriers.[X]
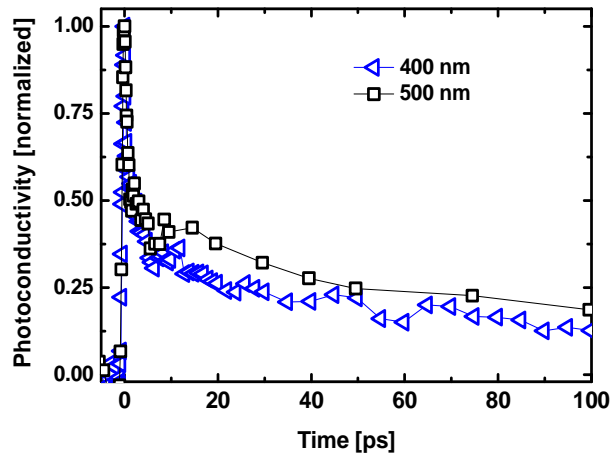

Figure 4-9 Comparison of the transient photoconductivity in In_2S_3 thin films after excitation with 400 nm and 500 nm laser pulses at a photon fluence of about $4 \cdot 10^{12}$ cm^{-2} and $2 \cdot 10^{13}$ cm^{-2}, respectively.[XI]

Hot carriers have a higher mobility than cold ones if a dominating scattering mechanism becomes less efficient with higher kinetic energies (cf. charged impurity scattering in section 2.2.3), or when there are energetic barriers along the transport path.[112,116,117,XII] Energetic barriers may arise from charged defects, which for example can accumulate at grain boundaries and create a potential barrier that requires an activation energy to be overcome.[116] Specifically in compensated semiconductors, clusters of charged impurities may create a spatially fluctuating electrostatic potential that impedes the charge transport.[117] As stated in 4.2.2, In_2S_3 might have a high degree of compensation. However, the excitation density (Figure 4-8) and the pump photon energy (Figure 4-9) do not seem to have an impact on the transient photoconductivity which renders a hot carrier related effect unlikely: The influence of charged defects on the carrier transport can be screened and would therefore exhibit excitation density dependence. Also, the cooling dynamics should depend on the pump photon energy because the latter determines the excess energy.

Based on the above discussion, the most likely assignment of the fast conductivity dynamics is the transition from mobile band states into shallow traps. Shallow traps have long been used in the

---

[X] Hot carriers are characterized by a Fermi-Dirac partition function with a temperature that is higher than the equilibrium lattice temperature.

[XI] These measurements have not been performed in vacuum.

[XII] An example where these two effects have a strong influence on the charge carrier dynamics is given in chapter 6 with $CuInSe_2$.

context of multiple trapping (MT) to explain the dispersive transport in disordered semiconductors.[118,119] The following analysis of the transient photoconductivity by the MT model is simplified by restricting the discussions to the electron dynamics. Electrons and holes are not separately addressable here, however, considering the effective masses (section 4.2.2) it is at least reasonable to assume that the electron contribution to the photoconductivity dominates. The MT model assumes that mobile band states are separated from localized states by the so called mobility edge E_0.[XIII] Below the mobility edge, the density of states exhibits 'band-tails', i.e. the density of (then trap) states D_t is assumed to decay exponentially into the band gap as

$$D_t = \frac{N_t}{kT_0} \cdot e^{\left(\frac{E-E_0}{kT_0}\right)},$$

(4.19)

with the characteristic width kT_0 and the trap density N_t.[XIV] According to elementary semiconductor statistics,[115] the trapping rate is proportional to the photocarrier density and the number of empty trap states while the detrapping rate is proportional to the number of occupied trap states and empty conduction band states. Multiple Trapping, the photocarrier generation rate $G(t)$ and a recombination term $R(t)$ determine the rate equations for the density of free electrons n and the time-dependent trap occupation probability $p_t(E,t)$:

$$\frac{dn}{dt} = G(t) - \int_{E<E_0} c_t D_t \Big[\underbrace{n(1-p_t)}_{\text{trapping}} - \underbrace{(N_c-n)p_t \frac{e_t}{c_t}}_{\text{detrapping}}\Big] dE - R(t)$$

$$\frac{dp_t(E,t)}{dt} = c_t n(1-p_t) - (N_c-n)p_t e_t$$

(4.20)

Here, c_t (e_t) denotes the capture (emission) rate constant, and N_c is the (effective) conduction band density of states at the mobility edge.[XV] Considering that $p_t(E,t)$ is given by a Fermi-Dirac distribution in thermal equilibrium, the capture and emission rate constants are connected by the principle of detailed balance as

$$e_t = c_t e^{\frac{E_t-E_0}{kT}}.$$

(4.21)

[XIII] The mobility edge is usually regarded as being 'sharp' because if localized and delocalized states existed isoenergetically, they would hybridize resulting in extended states.[120]

[XIV] Here, an exponential trap distribution is hypothesized. The real density may for instance as well obey a Gaussian distribution. However, this would at least not change the qualitative description of the MT processes.

[XV] For simplicity, an energetic distribution of mobile states and transitions between these states is not taken into account, and also transitions between localized states which can be important for the conduction below room temperature[121] are neglected. This means that effects like carrier cooling and hopping transport between localized states are not considered.

After some tens of picoseconds, the photoconductivity decay exhibits excitation density dependence, becoming faster for higher excitation densities (Figure 4-10 (a)). Since the conductivity lifetime in In_2S_3 is below about 10 ns,[59] it is reasonable that the transient conductivity which follows the rapid ps decay is due to actual electron-hole recombination. In order to model this pump intensity dependent recombination, $R(t)$ is chosen to model radiative band-band transitions. The radiative decay rate $R(t) = k_2 \cdot (np - n_0 p_0)$ is the simplest higher order recombination mechanism. If the photocarrier densities n and p exceed the dark carrier concentrations n_0 and p_0, $R(t)$ can be simplified to $k_2 \cdot n^2$ which is used here. As demonstrated in Figure 4-10 (a) the THz conductivity $\Delta\sigma = en\mu$ can be well described by calculating the transient electron population in the conduction band and the traps by the MT model (4.20) and by assuming that only the conduction band electrons are mobile. The best fit can be done with the set of parameters $N_t = 10^{19}\,cm^{-3}$, $N_c =$ $8.3 \cdot 10^{18}\,cm^{-3}$, $kT_0 = 47$ meV, $c_t = 3.2 \cdot 10^{-7}\,cm^{-3}s^{-1}$ and $k_2 = 6.2 \cdot 10^{-8}\,cm^3s^{-1}$.
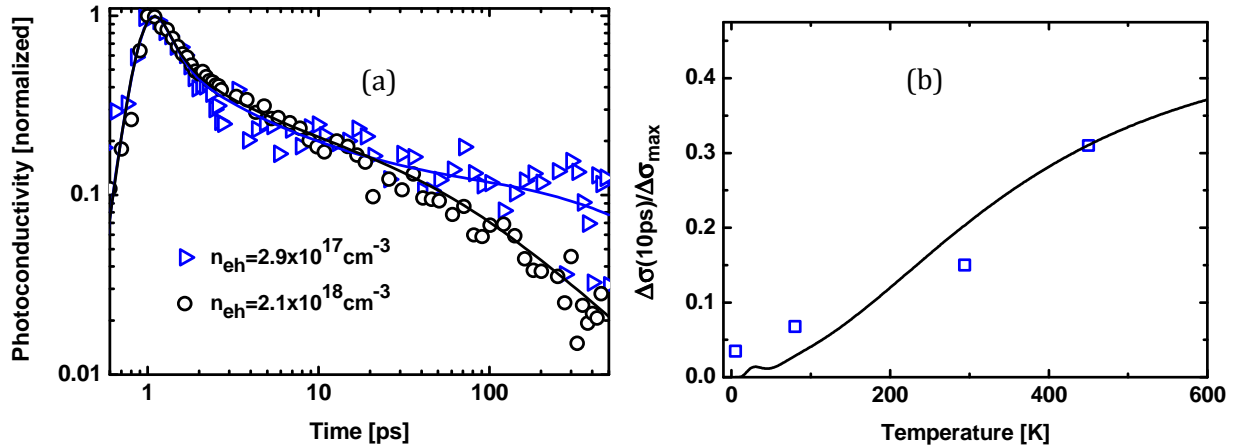

Figure 4-10 (a) Photoconductivity of a planar In_2S_3 thin film for two excitation densities. The lines are simulations of the transient conductivity with the MT model (4.20). (b) Simulated and experimental temperature dependence of the relative contribution of the slowly decaying component.

Interpreting the charge carrier dynamics with the MT model means the fast trapping of electrons into band tail states initially reduces the conductivity substantially. Thermal release of trapped charge carriers to the conduction band competes with trapping, and a quasi-equilibrium evolves with a fixed ratio of free to trapped electrons. However, electron-hole recombination leads to an eventual decay of the photoconductivity, albeit on longer time scales. Since detrapping is a thermally activated process, the fraction of trapped electrons, which loosely translates to the ratio of the relaxed (after a few ps) to the maximum photoconductivity, decreases for higher temperatures. If the best-fit parameters are used to simulate the conductivity dynamics at different lattice temperatures, the experimental trend can be reproduced remarkably well (Figure 4-10 (b)), which backs up the proposed MT model. Since a higher temperature leads to a higher trap release rate, it is well conceivable that the charge separation then proceeds faster and thus with fewer

losses. In prototypical devices based on ZnO/In_2S_3 core/shell nanorods it has indeed been observed that the short circuit current doubles from 180 K to 320 K,[60] giving further support for MT governed electron transport in the absorber.

4.5.2   Charge Separation in Core/Shell Rods

To study the charge carrier dynamics in core/shell rods that follow selective excitation of the absorber shell, pump pulses with 2.5 eV photon energies were taken from a NOPA. This photon energy is well below the 3.3 eV band gap of crystalline ZnO,[65] and assures that direct band-band excitation does not occur. Since no photoconductivity can be measured after excitation of the bare nanorods with 2.5 eV photons ($\Delta\sigma < 1.3 \cdot 10^{-4}$ Scm at a pump fluence of $3 \cdot 10^{13}$ photons/cm^2), two photon absorption and excitation from defect levels do not have to be taken into account here.

Pumping In_2S_3 coated nanorods at 500 nm results in a long lived photoconductivity. The (effective) photoconductivity transient of a sample with an intermediate shell thickness of 9 nm is shown in comparison to that of a neat absorber layer on a 1 ns time scale in Figure 4-11 (a). Initially the conductivity of the core/shell system decays rapidly and in a similar fashion as that of the bare In_2S_3, though there is a difference in the characteristic times of the decay. It will turn out that this difference can be accounted for by variations of the trap density. However, in contrast to the bare absorber the core/shell rods exhibit a decay that slows down and crosses over to a slow hundreds of ps long rise. It has already been shown by TRMC measurements that a long lived (up to µs) charge separated state is formed in the core/shell rods.[59] Hence, the most natural and only reasonable explanation for the delayed rise is the migration of electrons from the In_2S_3 phase to the ZnO phase. While about the first 10 ps of the transient photoconductivity are mostly governed by trapping of carriers within the In_2S_3 shell, the subsequent transfer of electrons to the ZnO increases the signal again, owing to the higher mobility (Figure 4-7).

A surprising behavior is found if the signals for samples with different In_2S_3 shell thicknesses are compared. Figure 4-11 (b) shows the conductivity transients of the thinnest and the thickest studied shell. The effective photoconductivity is depicted normalized to the absorption coefficient α when comparing samples with different shell thicknesses, to eliminate the influence of optical absorption on signal amplitude. In contrast to the core/shell rods with an intermediate 9 nm thick shell, the rods with the thickest and thinnest shell exhibit an (almost) monotonically decreasing and increasing photoconductivity, respectively. Despite the differences in the beginning, the normalized transients converge to roughly the same value at $\tau = 1$ ns and the dynamics slow down which indicates that the charge separation process is mostly complete after 1 ns. Another very surprising feature of the transients is that $\Delta\sigma / \alpha$ at the very beginning (1 ps) is not even approximately constant: It increases by a factor of about 10 from 4 nm to 17 nm shell thickness.
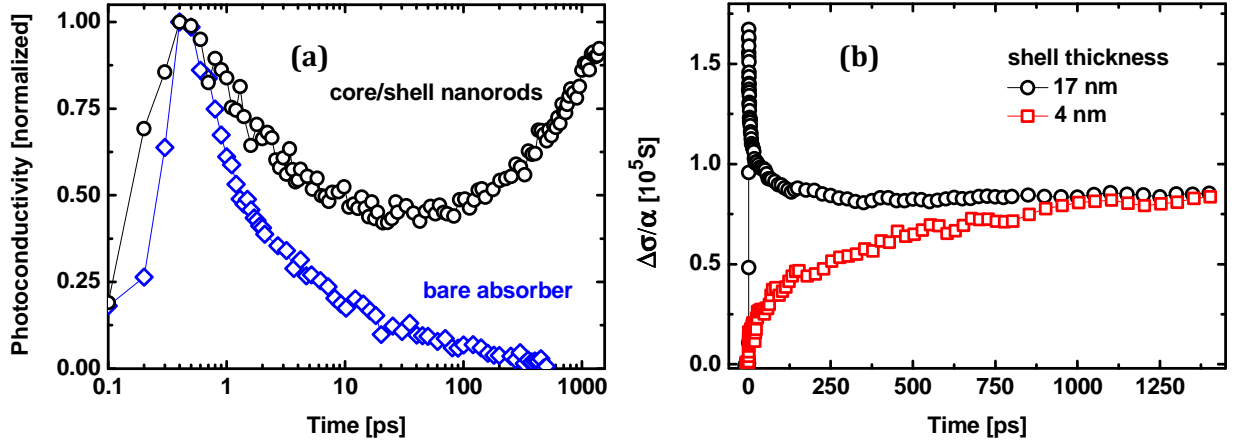
Figure 4-11 (a) Photoconductivity transients of a planar In_2S_3 layer and ZnO/In_2S_3 core/shell nanorods (9 nm shell thickness). (b) Absorption normalized conductivity transients of the core/shell nanorods with the thickest and the thinnest In_2S_3 shell.

The data for the core/shell nanorods in Figure 4-11 represents the effective photoconductivity. As outlined in section 4.4.2, the effective conductivity results from the carrier concentrations in the core and the shell, the respective mobilities, and the geometry of the core/shell rods. It is general-ly not possible to conclude from the effective conductivity on the mobilities or carrier concentra-tions. However, an understanding of the charge carrier relaxation in the shell and the charge sep-aration to the core can be achieved by simulating the effective conductivity by the correlated three component effective medium approach. Photoexcitation increases the carrier density in the shell by $n_s(t)$ which leads to a change of the In_2S_3 permittivity from the dark value $\epsilon_s = 13.5$[122] to $\epsilon_s + i(en_s\mu_s)/(\omega\epsilon_0)$. Similarly, electrons that migrate to the ZnO core increase the conduction band electron density by $n_c(t)$ and the core permittivity changes from $\epsilon_c \approx 7.9$[105] to $\epsilon_c + i(en_c\mu_c)/(\omega\epsilon_0)$.

Since the core (μ_c) and shell (μ_s) mobilities cannot be broken down to the contribution of elec-trons and holes, it is assumed again that the electron contribution dominates, and the combined mobilities from Figure 4-7 are used as approximations for μ_c and μ_s. Figure 4-12 (a) depicts how the normalized effective photoconductivity $\Delta\sigma/\alpha$ varies with shell thickness and the fraction of carriers x that have been injected from the shell into the core. The situation directly after the pump, when all photogenerated carriers are still in the shell corresponds, to $x = 0\%$ and full in-jection into the core without any losses corresponds to $x = 100\%$. As can be observed, the con-ductivity rises strongly when the carriers are transferred from the shell to the core. This is an expected result, since the intra-rod mobility of the ZnO nanorods is higher than the In_2S_3 shell mobility (Figure 4-7). However, it is surprising to see that the absorption normalized conductivity $\Delta\sigma/\alpha$ also increases strongly with the shell thickness. Figure 4-12 (b) demonstrates that this trend roughly reproduces the amplitude of the measured effective photoconductivity directly after the. For the two samples with the thinnest shells, the effect of an EMA alone cannot fully

capture the reduction of the measured effective conductivity. Most likely this deviation can be ascribed to a reduction of the intra-shell mobility due to localization effects when the shell thickness is reduced.
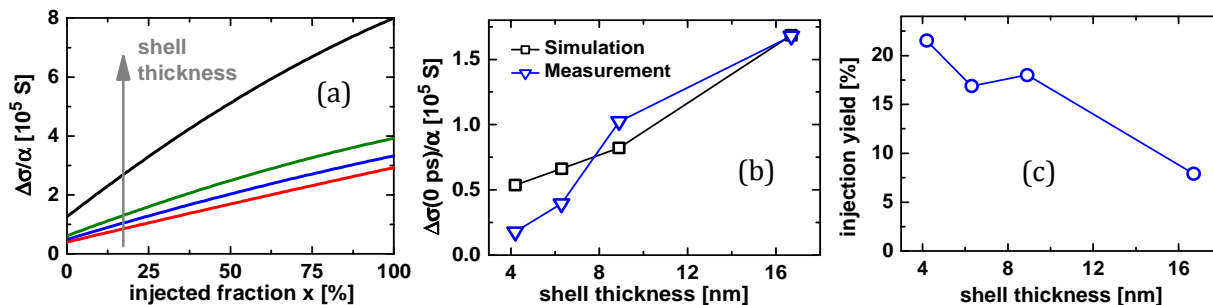

Figure 4-12 (a) Variation of the normalized effective conductivity $\Delta\sigma/\alpha$ with the shell thickness d_s and the fraction of carriers injected from the shell into the core. (b) Variation of the initial photoconductivity with shell thickness compared to the simulation results from (a) for x = 0%.[XVI] (c) Dependence of the estimated injection yield at 1.4 ns on the shell thickness.

The EMA also shows, that the shell enhances the contribution of the core conductivity to the effective conductivity of the rod-vacuum composite (x = 100 % in Figure 4-12 (a)). However, the measured effective conductivities after 1.4 ns seem to converge to roughly the same value independent of the shell thickness. This actually means that the injection yields for different shell thicknesses after 1.4 ns are very different. Estimating the injection yield by comparison of the amplitudes of the measured effective conductivity after 1.4 ns with the simulated values for full injection shows how the injection yield decreases with shell thickness (Figure 4-12(c)). This demonstrates that one has to be careful when interpreting the effective conductivity of nanoparticle absorber/acceptor composites.[59,123] Specifically the previous result,[59] that the charge injection efficiency is independent on the shell thickness up to 45 nm seems to be erroneous. The estimated injection yield here now agrees with the strong decrease of the short circuit current with increasing shell thickness that was found for cells based on ZnO-core/In$_2$S$_3$-shell nanorods and a CuCSN hole conductor.[4] Even for the thinnest shell of 4 nm the estimated injection yield is just about 22 % and it drops to 8 % for the thickest shell. This loss is notably higher than in complete solar cells where the external quantum efficiency of the best cell was reported to be higher than 90 % at AM1.5.[4] This discrepancy can be understood by the higher fluence in this study and the intensity-dependent recombination. The average pump power in this study translates into about 15 suns at AM1.5 and the solar cell quantum yields were found to decrease with pump intensity.[60]

[XVI] To match the amplitudes of the simulated and the experimental photoconductivity, the former was scaled by a factor of 0.75.
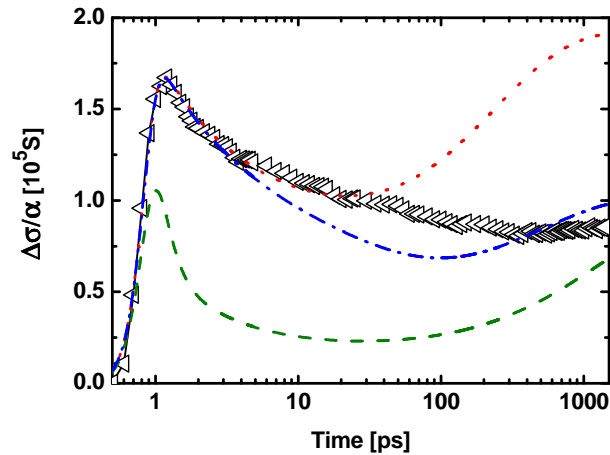
Figure 4-13 Measured photoconductivity (triangles) of the core/shell rods with the thickest shell (17 nm) and simulated transients for $N_t = 2 \cdot 10^{18}\,\text{cm}^{-3}$ and $\tau_{inj} = 1$ ns (blue, dash-dotted), $N_t = 2 \cdot 10^{18}\,\text{cm}^{-3}$ and $\tau_{inj} = 400$ ps (red, dotted) and $N_t = 10^{19}\,\text{cm}^{-3}$ and $\tau_{inj} = 1$ ns (green, dashed).

Figure 4-13 demonstrates that the principal features of the measured core/shell nanorod photo-conductivity transients can be reproduced by using a simple rate constant approach for the spatial charge separation. Starting with the MT model (4.20) to describe the dynamics in the shell, a linear injection rate n / τ_{inj} is added to simulate the carrier transport from the shell into the core. By calculating the carrier densities separately for ZnO and In_2S_3 as a function of time, the total photoconductivity is derived using the effective medium formalism and the mobilities from Figure 4-7. Figure 4-13 illustrates the influence of two main parameters: the trap density N_t in the absorber and the escape time τ_{inj}. The other parameters were kept constant at the values from the analysis of planar In_2S_3. For $N_t = 2 \cdot 10^{18}\,\text{cm}^{-3}$ and $\tau_{\text{inj}} = 1$ ns the simulated transient is in fair agreement with the measured conductivity. In particular, the magnitude of the photoconductivity at the end of the time window is reproduced. If the injection time is changed to 400 ps, more carriers survive the recombination process inside the absorber and the injection yield is overestimated. Thus, the calculated photoconductivity is considerably higher than the measured data after about 30 ps. However, up to that point, the agreement is much better than for the simulation using the longer injection time of 1 ns. This indicates that for a more quantitative model spatial transport and the boundary conditions at the interfaces have to be taken into account.

If the trap density is chosen as the fit result from the bare In_2S_3 (10^{19} cm^{-3}), the amplitudes and decay characteristics are off by a larger margin. This could well originate from the omission of an adequate spatial transport in the model, but could also point to a different material quality when the In_2S_3 is grown onto the ZnO rod structure instead of a planar substrate. With Spray-ILGAR, the indium is offered in the form of $InCl_3$-ethanol droplets while the sulfur is added as H_2S in the gas phase. The local concentration of precursors may then be influenced by a different mass transport inside the ZnO pores changing the material properties.

4.6 Conclusions

OPTP spectroscopy has been demonstrated as a powerful tool for studying charge carrier separation and recombination in semiconductor core/shell nano-heterojunctions. First, the photoconductivity of ZnO nanorods and bare In_2S_3 thin films was analyzed separately, followed by an examination of ZnO/In_2S_3 core/shell nanorods with systematically varied shell thicknesses. The dynamics of the photogenerated charge carriers in the In_2S_3 absorber is found to be dominated by ultrafast capture into shallow traps. A quantitative description of the dynamics is achieved by a MT model, which is consistent with a high trap density in the absorber on the order of 10^{19} cm^{-3}. The transient THz absorption of the core/shell nanorods displays complex dynamics which are strongly dependent on the shell thickness: The transients may exhibit a continuous decrease or increase or a combination of both. These dynamics can be described by superimposing the conductivity decay in the shell due to ultrafast trapping and second order recombination, and a rise component due to electron migration to the core with a higher mobility. Employing a new correlated three component effective medium approach permits to calculate the effective conductivity of core/shell nanorod layers from the separate conductivities within the shell and the core. By comparison with the measured conductivity it can be inferred that the injection yield drops significantly with increasing shell thickness. This finding is in line with the recent observation of a decrease in short circuit current with increasing shell thickness in solar cells made of the same material.

5 Electron Transfer through Interface States in ZnO/Dye Hybrids

Electron injection from photoexcited chemisorbed dyes into zinc oxide is known to proceed in a stepwise manner, i.e. the injected electrons do not occur simultaneously with the dye cation. Yet, the origin of the injection retardation remains controversial. This chapter presents a complementary time-resolved spectroscopy study on the electron injection dynamics from organic dyes into ZnO. The dyes comprise model perylene derivatives whose bridge units are systematically lengthened to clarify the influence of the positive cation on the escape of the injected electron. The combination of TA, OPTP and 2PPE reveals that the delayed release of charges into ZnO is independent of coulomb attraction between the dye cation and the injected electron. Rather, following dye photoexcitation the primary acceptor states of electron transfer into ZnO are interface states formed between the dye and the ZnO surface, which retard the formation of free charges.

5.1 Motivation

The growing demand for sustainable energy generation stimulates research into developing alternative material compositions and concepts for low-cost solar energy conversion using photovoltaics. Dye-solar cells (DSCs), where solar light harvesting dyes are chemically attached to a semiconductor surface, are a promising class of photovoltaic materials. Most studies in the past have focused on Ruthenium-based metal-organic dyes and TiO_2 colloidal electrodes.[5] However, pure organic dyes and electrode materials with higher mobilities or geometries without need for percolation have potential benefits. In this respect, ZnO has been investigated as a potential replacement for TiO_2 as it possesses a variety of advantages over TiO_2. ZnO has a higher bulk mobility than TiO_2 and can easily be grown as well-aligned and crystalline nanorods with direct contact to the back electrode. In principle, this should facilitate the collection of photogenerated carriers compared to the randomly organized percolation networks in colloidal TiO_2 structures. However, ZnO has so far shown inferior performance over TiO_2 electrodes, which reasons are subject to various investigations. One currently debated problem is the delayed injection mechanism into ZnO, [48,124–126] which might have detrimental effects on the injection and recombination processes.

Irrespective of the specific electrode configuration, the primary process in DSCs remains the photoinduced injection of electrons across the organic/inorganic interface. Over the last 15 years numerous time resolved studies have been performed on the subject of heterogeneous electron transfer (HET) from chemisorbed, photoexcited dyes into a semiconductor electrode, mostly in

the context of DSCs.[46] Most of these studies focused on the transient evolution of molecular absorption bands, e.g. excited or cationic state absorption. The most widely used method was transient absorption (TA) in the visible spectral range, and the dynamics were discussed on the basis of the density of bulk acceptor states and the electronic coupling of these states with the dye excited state. Less attention was paid to the fact that the acceptor states in HET may also comprise trap states at the surface.[127]

A more complete picture can be derived when TA spectroscopy is extended into the near and mid-IR region, or even complemented by optical-pump terahertz-probe (OPTP) spectroscopy.[10] With these methods, the arrival of injected electron in semiconductor bulk states and thus the generation of freely moving electrons can be probed by intra-conduction band transitions. This extension allows probing the injection dynamics separately from both, the molecule and the semiconductor side, and renders important additional information. Based on a comparative study employing visible to near infrared (NIR) probe pulses to analyze the dynamics of the widely used Ru-complex N3 attached to colloidal ZnO, it was first proposed by Furube et al. that the electron transfer from the excited dye to the final ZnO bulk acceptor states proceeds via intermediate species on the ZnO surface.[124] The intermediate state was explained as an exciplex formed between the dye excited state and a ZnO surface state.[124] The occurrence of a stepwise injection mechanism could be confirmed in other studies with ZnO nanoparticles sensitized by coumarin derivatives[125,126] and a porphyrine-based dye.[48] In the latter case, the authors assigned the origin of the intermediate species to the Coulomb attraction between positively charged dye cations at the surface and injected electrons. They also reported that the Coulomb attraction impedes electron transport by reducing the intra-particle mobility. Other suggestions for the nature of the intermediate state are injection into resonances or injection into dye-induced surface-localized states.[126] Since the intermediate state is expected to be localized at the interface between ZnO surface and dye, the electron back reaction is potentially faster compared to a delocalized bulk acceptor state.[128] Thus, the presence of intermediate states is of general importance for the functionality of dye-sensitized ZnO solar cells as it might jeopardize the injection process and allow for increased recombination of electrons with the oxidized dye.

As interface states may play a crucial role in the electron transfer, TA and OPTP spectroscopy should preferably be complemented by a surface-sensitive technique. 2PPE can selectively probe the transient non-equilibrium population of molecular and semiconductor states at the interface region, and has been demonstrated to be a proper tool for unraveling HET.[129] 2PPE has been shown to yield the same information on molecular injection dynamics as TA,[130,131] while additionally allowing to probe the bulk escape of injected electrons.[132] Applying 2PPE on perylene derivatives chemisorbed to TiO_2 gave indications for electron injection into adsorbate-induced interface states prior to delocalizing into the TiO_2 bulk.[130,131] While this can also be interpreted as a stepwise injection mechanism, the free electron absorption of dye-sensitized TiO_2 can built up within

25 fs,[133] which is orders of magnitude faster than in ZnO.[48,124–126] Hence, even though there are indications that intermediate species occur also in electrode materials other than ZnO, the lifetimes of the intermediate species and their implications on recombination losses are exceptionally high for ZnO.

This chapter intends to gain a better understanding of the stepwise injection mechanism in ZnO hybrids. For this purpose HET from chemisorbed model dyes into ZnO is complementary probed with TA, OPTP, and 2PPE for a series of perylene derivatives with systematically prolonged conjugated bridges and a carboxylic anchor. The increasing bridge length introduces a variable spatial separation between the cation and the ZnO surface, which allows testing the influence of the cation coulomb attraction on electron injection.

The analysis focuses on the $(10\bar{1}0)$ surface of ZnO, which is the most stable low index surface of ZnO[134] and the predominating surface of ZnO nanorods. 2PPE measurements are carried out on ZnO$(10\bar{1}0)$, whereas TA and OPTP experiments are performed on dye-sensitized ZnO nanorods, which yield adequate transient absorption signals due to the enhanced surface area.

5.2 Sample Preparation

ZnO nanorods with a diameter of about 60 nm and a length of 2-3 µm are grown by the procedure described in section 4.3. The six side facets of the ZnO nanorods dominate the surface available for dye interaction, and consist of the most stable, mixed-terminated nonpolar $(10\bar{1}0)$ surface.[134,135] For TA and OPTP measurements alkali free glass[I] and [0001] oriented quartz substrates are used as substrates, respectively. Glass substrates coated with a conductive indium tin oxide layer were used for UPS and XPS measurements to prevent a charging of the samples.

The chemical structures of the basic perylene chromophore with tert-butyl spacers which prevent dimerization,[136] and the different bridge/anchor groups are shown in Figure 5-1. The synthesis of C3 with the CH=CH bridge and COOH anchor is described elsewhere.[27] The extended conjugated bridges of the molecules C5-C11 are prepared by successive Wittig-Horner reactions, and/or Knoevenagel condensation. The substances are purified via column chromatography on silica gel and characterized by nuclear magnetic resonance (NMR) and mass spectroscopy. The purity of the substances is at least 95 %.[40]

The nanorod samples are heated in a mufle furnace at 430 °C in air for 60 min, and cooled to room temperature in nitrogen atmosphere. The films are then sensitized for one hour in a nitrogen environment using 10^{-5}M chloroform solutions of the perylene derivatives. During sensitization the

---

[I] The presence of sodium influences HET.[32]

samples are gently shaken with an IKA MS3 shaker. After dye sensitization, the samples are rinsed with spectroscopic grade chloroform for 5 min to remove any excess dye molecules not attached to the surface. The dye-sensitized samples are evacuated in a desiccator (p ≈ 10^{-4} mbar) for 30 min prior to steady-state absorption, TA, or OPTP measurements. Samples for UPS and XPS measurements are dried under nitrogen atmosphere.
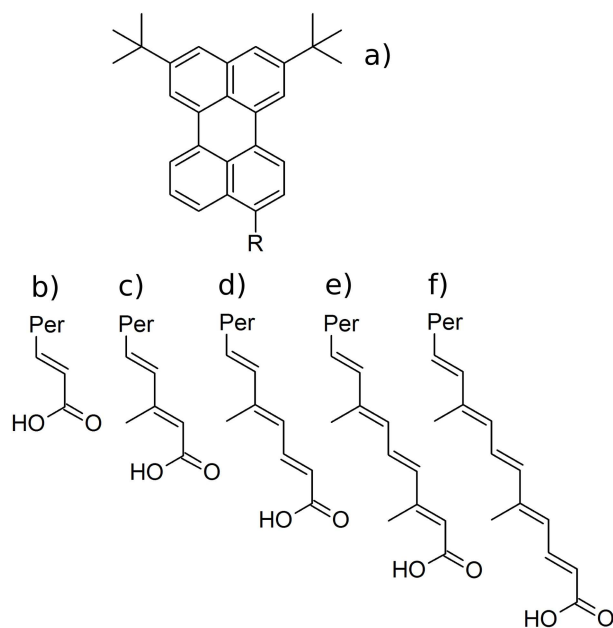
Figure 5-1 a) Structure of the perylene derived chromophore, b)-f) the different bridge/anchor units attached to the chromophore, yielding the dyes C3, C5, C7, C9, and C11.

For 2PPE measurements, $ZnO(10\bar{1}0)$ single crystals were purchased from Mateck GmbH. After cleaning the surface in a UHV chamber[II] (10^{-9} mbar) by several cycles of Ar^+ bombardment (650 eV, 10 min, 6-8 µA) and annealing at 400 °C for 10 min, the ZnO crystal is transferred under UHV conditions into a UHV chamber for in-situ dye-sensitization. First, the preparation chamber is flooded with ultrapure N_2 to a pressure of about 400 mbar. Then a $2 \cdot 10^{-5}$ M degassed solution of C3 in chloroform is prepared using a Schlenk line, and pumped from a glass flask connected to the preparation chamber into a cuvette inside of it. Subsequently, the ZnO crystal is immersed into the dye solution containing cuvette. After about 60 min of sensitization, the ZnO crystal is rinsed several times with pure, water-free chloroform to remove loosely bound dyes. As a last step, UHV conditions are restored inside the preparation chamber, and the crystal is transferred back to the 2PPE chamber under UHV conditions.

[II] XPS measurement show that this cleaning procedure effectively removes organic contaminations (cf. section 8.3) from the single crystal surface.

5.3 Properties of the Perylene Derivatives

A good understanding of the optical transitions in the dye molecules is a requirement for the analysis of the TA of the hybrid systems. Hence, the spectral absorption bands of the neutral, the optically excited, and the ionized molecule are identified in 5.3.1. This is followed by a discussion of the LUMOs of the neutral molecules and the HOMOs of the oxidized molecules because the LUMO's spatial overlap with the acceptor states has a great significance for the electron injection, and the cation HOMO can be interpreted as the origin of the Coulomb attraction on the injected electron.

5.3.1   Spectral Characterization

Figure 5-2 exhibits the optical absorption of C3, C7, and C11 anchored to ZnO nanorods and of C3 dissolved in methanol. With increasing bridge length of the chemisorbed molecules, the absorption of the hybrid systems extends more into the red, while for all dyes the first ground state absorption band peaks around 450 nm. Comparing the optical absorption of C3 dissolved in methanol and anchored to ZnO nanorods, demonstrates the influence of the chemical environment: The absorption is strongly broadened when the dyes are anchored on the ZnO electrode. Based on a previous study, most of this broadening can be ascribed to inhomogeneous rather than to lifetime broadening.[137] This means that the spectral broadening reflects the immanent heterogeneity of the sensitized samples where each dye has a slightly varying local chemical environment.

A Franck-Condon progression, with a peak separation of the different vibrational levels of the perylene skeletal stretching mode of about 170 meV, underlies the first ground state absorption.[137] Due to a strong inhomogeneous broadening, this is not very obvious for the chemisorbed molecules with conjugated bridges but can be identified for C3 in methanol.[III] The energy of the involved vibrational mode is $\gg k_B T$ at room temperature. Therefore, only the vibrational ground state of this mode is populated at room temperature. In the THz and 2PPE experiments, the 500 nm pump photons excite the dyes at the low energy side of the ground state absorption. At least for C3, this will mainly generate the vibrational ground state of the electronic excited state. In the TA experiments also pump pulses with 425 – 450 nm center wavelength are used, which can populate vibrationally excited states of C3-C11.

[III] It can even be resolved more clearly when the acrylic acid (-CH=CH-COOH) bridge/anchor in C3 is exchanged by propionic acid (-CH_2-CH_2-COOH).[138]
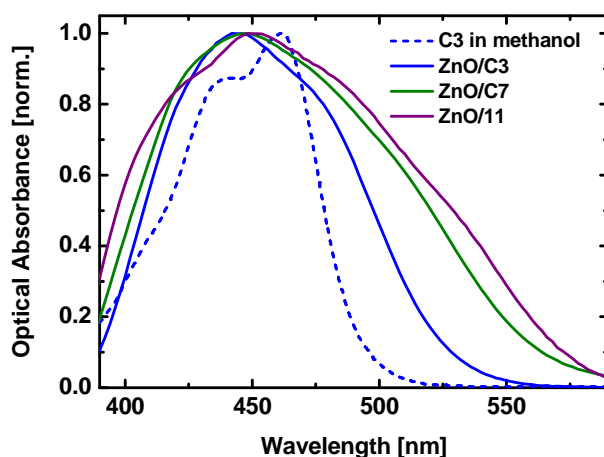
Figure 5-2 Ground state absorption of C3 dissolved in methanol and of C3, C7, and C11 chemisorbed to ZnO nanorods. The dye related absorption is identified as the difference of the absorption spectra of the ZnO/dye hybrids and bare ZnO nanorods.

Molecular transitions of ZnO hybrid systems whose excitation energy is higher than the ZnO band gap are difficult to probe in practice. Absorption measurements in solution show that the next (experimentally observable) absorption band above the ground state absorption locates around 260 nm for C3.[40] The energetic difference of the first absorption band around 450 nm and the second band around 260 nm corresponds to a transition at 700 nm, which is where the excited state absorption can be probed.[40] This means that the same energetically higher lying state can be reached through optical excitation from the ground and from the first excited state. The molecules with longer bridges (C5-C11) exhibit the band at 260 nm but also additional bands between 260 nm and 450 nm.[40] The energetic differences between these additional bands and the first absorption band correspond to wavelengths from the NIR to the visible. Hence, if these transitions are allowed, they will invoke excited state absorption bands in C5-C11 from the visible to the NIR as well, which can in fact be observed up to 1100 nm in ZnO/C11 (cf. Figure 5-10).

The spectral properties of neutral and excited C3 in solution as well as attached to colloidal TiO_2 and ZnO nanoparticles and the cation generated in oxidizing agents have been studied before.[40,139] The excited state of C3 in methanol peaks at 720 nm and the maximum of the cationic absorption generated by oxidation in sulfuric acid is at 595 nm. Attached to TiO_2 or ZnO nanoparticles these absorption bands can be observed at almost the same spectral positions,[40,139] and they are very similar to those of the ZnO nanorods hybrids with the bigger molecules C5-C11 (Figure 5-3).
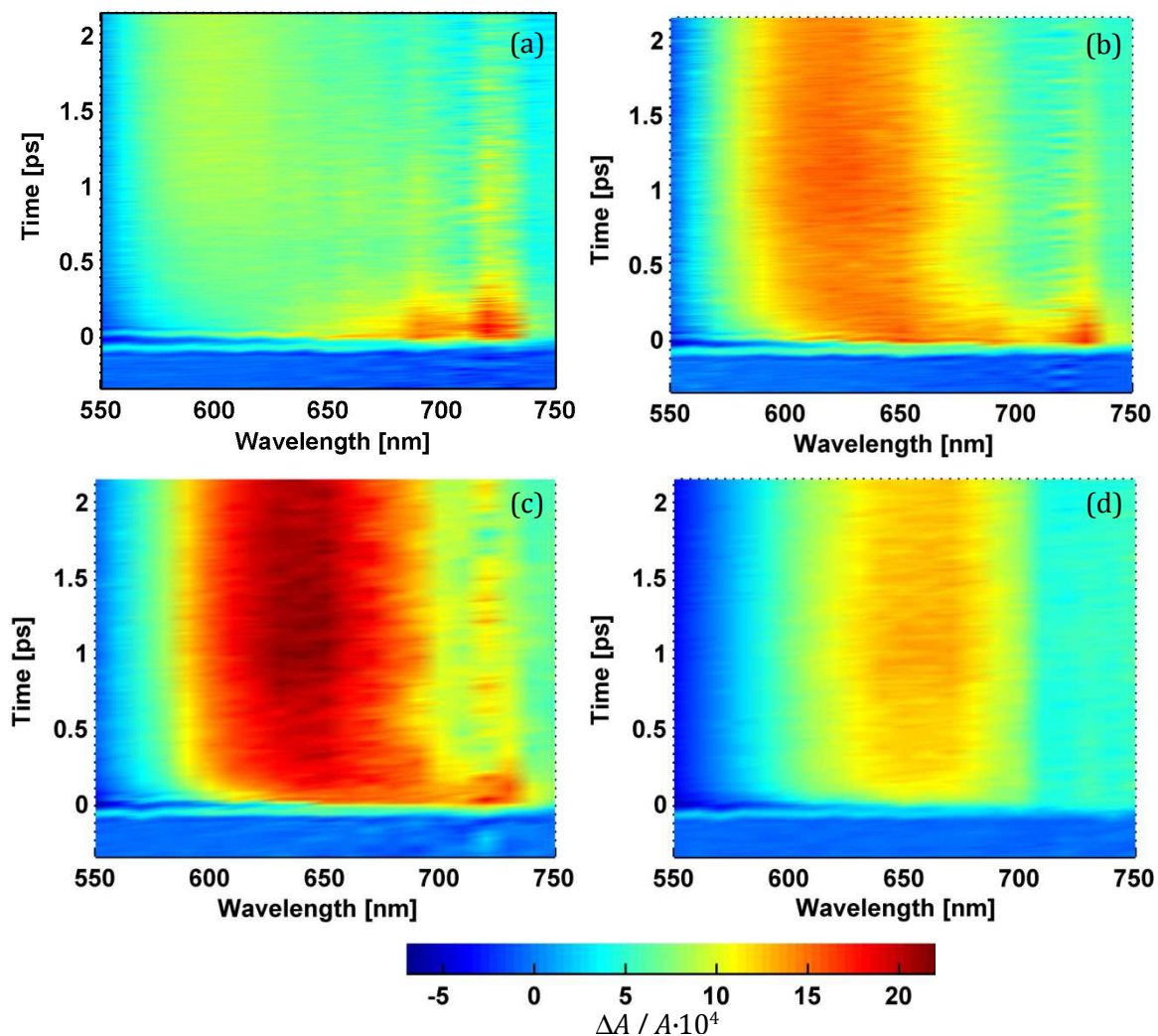
Figure 5-3 Transient differential absorption spectra of ZnO nanorods with C5 (a), C7 (b), C9 (c), and C11 (d). The legend, where positive values indicate increased absorption, applies to all graphs. The positive differential absorption in the depicted spectral region is attributable to excited and oxidized molecules, while the negative differential absorption at the low wavelength side is due to ground state bleaching.

However, with increasing bridge length the absorption bands of oxidized and excited molecules progressively overlap. Still, the absorption bands shown in Figure 5-3 can be assigned to the oxidized and excited states based on the spectral similarity of C5-C11 to the thoroughly studied C3 (Figure 5-2). This assignment is also conform to the observed dynamics (section 5.5.1, Figure 5-3) because the rise time of one feature (cation) is equal to the decay time of the other feature (excited state).[IV] Further support comes from a measurement of the excited state absorption of C5 and C11 in methanol which is centered around 720 and 665 nm, respectively.[40] It is also possible to

---

[IV]The fact that electron injection occurs and thus, that the cation is generated is unambiguously proven by the OPTP measurements (cf. section 5.5.2).

estimate the absorption spectrum of the oxidized molecules by the differential absorption at a very long pump-probe delay.[v] These quasi-cation spectra peak at 595/610 nm for C3/C5 and around 650 nm with a tail into the NIR for C7, C9, and C11 (Figure 5-4).
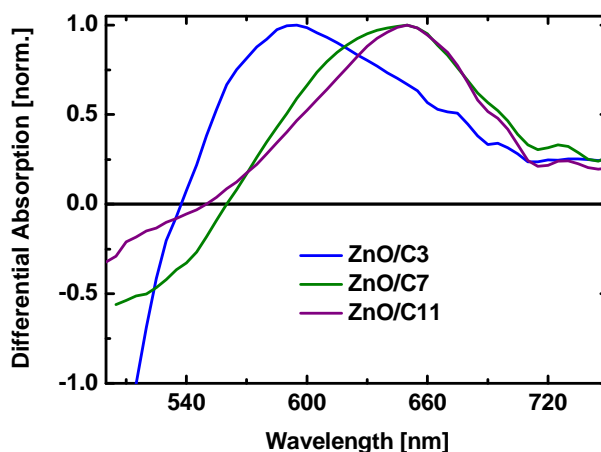

Figure 5-4 Differential absorption spectra for selected ZnO/dye hybrid systems at a long pump-probe delay of 500 ps. Positive values indicate an increase in absorption assigned to cation absorption. The increased transmission (negative signal) around 500 nm is due to ground state bleaching.

5.3.2 Molecular Orbitals

A prerequisite for a strong electronic coupling is a spatial overlap of the molecular excited state wavefunction with the empty acceptor states at the interface. Semi empirical calculations show that the highest occupied molecular orbitals (HOMOs) of the neutral molecules C3-C11 are mainly localized on the perylene chromophore, but the lowest unoccupied molecular orbitals (LUMOs) extend over the bridge onto the anchoring unit (Ref. 40 for C3, C5, C7 and C11, Figure 5-5 for C9). Hence, photoinduced HET should be facilitated irrespective of the length of the conjugated bridge. Recent quantum chemical calculations for C3 in methanol solution confirm that the S0-S1 transition is a HOMO- LUMO transition.[140] If the LUMO of the free molecule is taken as an estimate for the excited state of the ZnO/molecule hybrid system, strong electronic coupling between the dye LUMOs and the empty ZnO acceptor states leading to ultrafast electron transfer can be expected.

The LUMO of the cation is localized almost completely on the perylene part of the molecule for C3.[40] It was shown that for longer bridges (C5 – C11) an increasing part of the cation LUMO extends onto the bridge (Ref. 40, Figure 5-5), so that the effective distance of the cation LUMO to the surface appears to be increasing up to C7, and to saturate for C9 and C11. If the electron density of

---

[v] The spectrum may be distorted by a fraction of the excited molecules that do not participate in HET. This may e.g. occur for unbound molecules or for molecules at anchoring sites where HET is unfavorable.

the neutral molecule is assumed to be rather homogenous, and if the cation LUMO is used as an estimate for the missing electron density due to electron injection, the position of the cation LUMO can be related to the cation dipole moment. Indeed, the dipole moment of the cation ground state increases from 7.5 D for C3 to 10.8 D for C7, but is only 3.5 D for C11.[40] The dipole moment of the latter molecule is rather low because the missing electron density is partly shifted from the chromophore onto the bridge, i.e. it is localized near the center of the chromophore.
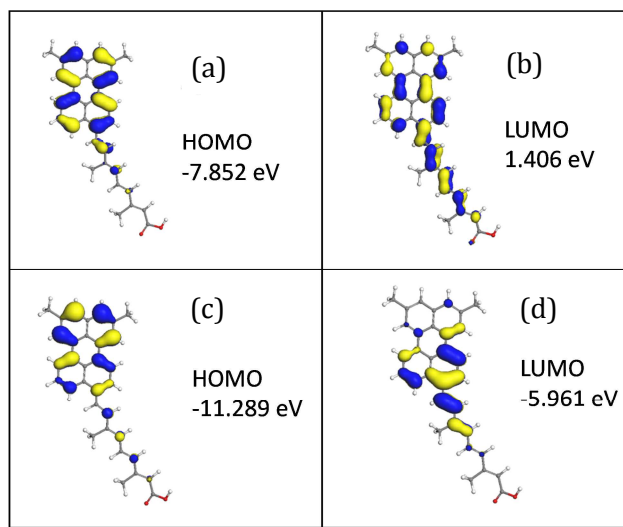

Figure 5-5 Isodensity plots of different molecular orbitals of the molecule C9: (a) HOMO of neutral C9. (b) LUMO of neutral C9. (c) HOMO of the cation. (d) LUMO of the cation. The semi-empirical molecular orbital calculations were performed with Materials Studio 6.0 (NDD0 Hamiltonian, AM1). The restricted/unrestricted Hartree-Fock (open/closed shell) method was used for the neutral/oxidized molecule, respectively. The molecular orbitals of C3, C5, C7 and C11 are presented in Ref. 40.

5.4 Characterization of the Interface

This section starts with a discussion of the carboxyl binding on $ZnO\left(10\bar{1}0\right)$ and the molecules' alignment, which influences the spatial separation of chromophore and surface. This is followed by XPS and UPS studies, which yield information on chemical contaminations and the energetic alignment of the molecular levels relative to the ZnO bands. The position of the injection level relative to the conduction band minimum plays an important role for the injection process, as stated by (2.49), and Co-adsorbants may also affect the transfer dynamics.[138]

5.4.1   Dye Adsorption

The interaction of the sensitizer molecules with the ZnO nanorods mostly occurs at the mixed-terminated, nonpolar $\left(10\overline{1}0\right)$ surface which constitutes the side facets of the nanorods.[134,135] Several studies on the adsorption of carboxylic acids on this surface, which is depicted in Figure 5-6, concluded that the bidentate bridging configuration has the highest molar adsorption energy.[141–144] In this configuration the –COOH carboxyl group is deprotonated and each oxygen binds to another Zn atom. However, other binding configurations (of relatively small molecules) that only use up one Zn per molecule were shown to have a lower adsorption energy per molecule but a higher adsorption energy per surface unit and are thus favored thermodynamically.
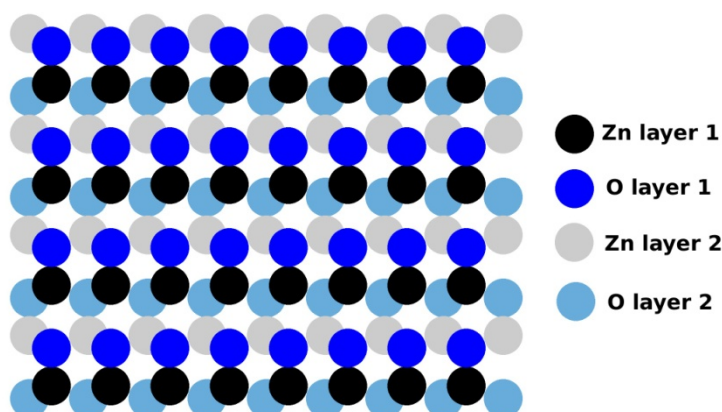

Figure 5-6 The two uppermost layers of the unreconstructed ZnO $\left(10\overline{1}0\right)$ surface. The horizontal/vertical distance of adjacent atoms of the same kind of the top layer is a/c with a = 3.25 Å and c = 5.207 Å.

The areal density of molecules adsorbed in the bidentate bridging binding mode is maximally about 5/nm² for a fully covered surface, which can be estimated from the density of available anchoring sites (Figure 5-6). From a comparison of the optical absorbance of ZnO/molecule hybrid systems to the absorbance of a molecular solution with known molarity, it can be estimated that the actual areal density of adsorbed C3-C11 is at most 2/nm² (section 8.4). One reason for this low surface coverage may be that many potential adsorption sites are occupied by unintended co-adsorbents such was water, hydrogen, or solvent molecules. Considering the size of the molecules with their bulky tert-butyl spacer groups, another reason may be that the maximal dye surface covering is not restricted by the number of Zn anchoring sites but by the dimensions of the molecules (cf. Figure 1 in ref. 145). Due to this constraint, the bidentate bridging mode may become the thermodynamically most stable configuration because a full coverage with the other binding modes cannot be realized. Hence, it is reasonable to assume that bidentate bridging is the most prevalent adsorption mode. According to recent calculations, C3 and C9 stand upright on

$ZnO/(10\overline{1}0)$ if they are anchored in the bidentate bridging mode.[145,146] This supports the notion of interpreting the bridge unit as a spacer between the cation and the injected electron.

5.4.2   Surface Contamination (XPS)

Core level binding energy spectra are acquired by XPS on freshly annealed ZnO nanorods,[VI] and on ZnO nanorods that are immersed in chloroform for 60 min after annealing. Figure 5-7 (a) shows that carbon can be traced on the unsensitized, freshly annealed nanorods (termed bare in the following), but that the C 1s XPS line is significantly higher on nanorods that have been dipped into chloroform after the annealing procedure. The C-contaminations on the bare ZnO nanorods most likely stem from the exposure to ambient atmosphere during the transfer to the XPS UHV chamber, and it can be assumed that also other (non C-containing) molecules such are adsorbed on the surface.
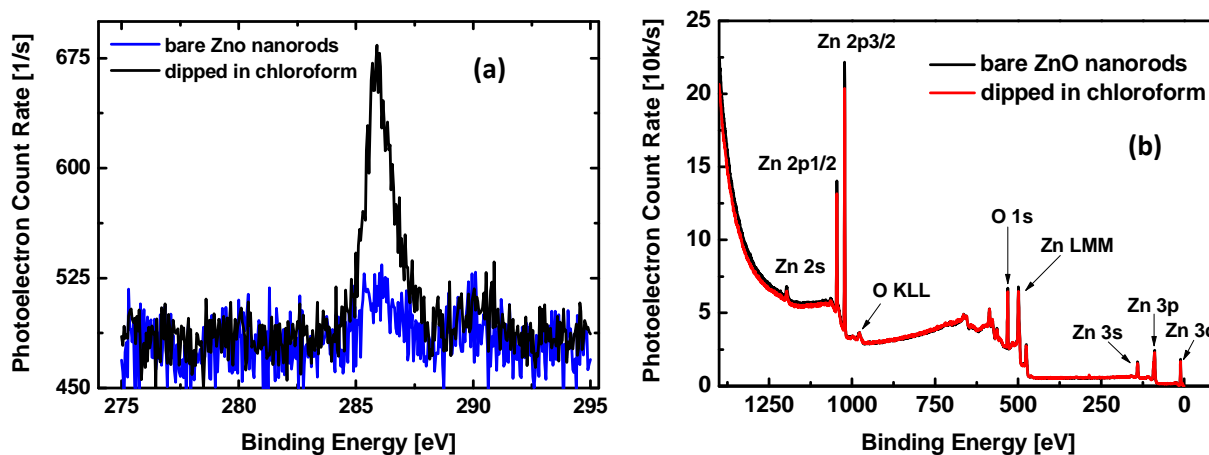

Figure 5-7 (a) C 1s XPS peak of freshly annealed nanorods and of nanorods that were dipped in chloroform for 60 min, which is the same exposure time as during sensitization. (b) XPS overview spectrum.

Though traces of carbon can be detected on freshly annealed ZnO nanorods as well as on cleaned $ZnO(10\overline{1}0)$ (cf. section 8.3), the XPS spectrum of the chloroform exposed nanorods demonstrates that the wet-chemical processing introduces by far the biggest amount of "dirt", which may stem from dissolved impurities and possibly even solvent molecules. Hence, the presence of unintended organic co-adsorbents is a common feature of hybrid systems in the field of DS(S)C's and cannot be avoided in principle by this routine. This is particularly true for dye sensitized TiO$_2$ or ZnO nanoparticle films because these nanoparticles are usually applied on the substrate by using an

---

[VI] The annealing procedure was the same as that of nanorods that were sensitized with dye molecules: Annealing at 430 °C for 60 min in ambient atmosphere and subsequent cooling in nitrogen atmosphere.

organic "glue" such as polyethylene glycol or ethyl cellulose, which cannot be completely removed afterwards.[32]

It is known that the chemical environment influences the electron injection process.[138] So strictly speaking, injection times that are derived experimentally on contaminated samples might be different than those that would be measured on hypothetical samples without any residual co-adsorbants. However, the different ZnO nanorod/molecule hybrids in this study are prepared under identical conditions, so a potential influence of the co-adsorbants should not perturb the comparison between samples. This also applies for the comparison of the ZnO nanorods, which are exposed to ambient atmosphere, and the single crystal surface, which is not exposed to ambient atmosphere, because the majority of contaminations stems from the solvent and not from the atmosphere. In addition to contaminations from the atmosphere or the solution, the sensitization of the ZnO surface in the dye solution can involve dissociative adsorption of the carboxylic anchor group, so that hydrogen, split-off from the carboxylic acid anchor group, is adsorbed on nearby oxygen surface atoms.[VII] Yet, the presence of hydrogen cannot be detected by XPS.

5.4.3   Level alignment (UPS)

The work function of ZnO nanorods was measured on bare and solvent exposed samples, and on specimens sensitized with C3, C7, and C11 in order to test if the solvent or the adsorbed dyes invoke an (additional) band bending. Within the scope of the statistical fluctuations, the work functions of the different samples are the same, with a mean value of $3.96\,eV \pm 14\,meV$. Hence, the adsorbed dyes, C-contaminations from solution, and hydrogen from dissociative anchoring (if present) have no significant influence on the energetic position of the ZnO states. Literature values for the work function of (clean) $ZnO(10\bar{1}0)$ are around 4.5 eV,[69,71,149] and adsorbed hydrogen, methanol, and water may lower this value by up to about 500 meV.[69–71] This indicates that the 3.96 eV work function of the ZnO nanorods may be influenced by some adsorbants, which however would have to stem from another source as the dye solution.

Figure 5-8 (a) depicts low binding energy UPS spectra of bare and C3 sensitized nanorods. The binding energy at the valence band maximum can be determined as 3.46 eV from the high-energy cutoff of the emission spectrum. Since the work function does not change upon dye sensitization, the positions of the band extrema relative to the Fermi energy remain unchanged, too. Hence, the

---

[VII] An extensive review on the effect of different adsorbants on ZnO was given by C. Wöll.[64] Theoretical results indicate that adsorption of hydrogen on $ZnO(10\bar{1}0)$ yields a metallic surface if it binds only to the oxygen atoms.[147,148] At room temperature hydrogen does not adsorb to Zn surface atoms and in compliance with theory, metallicity was found for hydrogen (and also water and methanol) exposed $ZnO(10\bar{1}0)$.[69–71] The metallicity arises because hydrogen (and the other adsorbants) act as charge donors and induce a charge accumulation layer at the surface along with downward band bending.

UPS spectra of the hybrid systems with C3, C7, and C11[VIII] can be compared to that of bare nano-rods, yielding two peaks for each dye, which are located 0 eV and about 1.3 eV above the VBM, and which are assigned to the HOMO-1 and HOMO, respectively. A very similar alignment was observed in nanocolloidal TiO_2/C3 hybrids.[150] For C3 the positions of the HOMO and HOMO-1 relative to each other and relative to the VBM can also be compared to recent DFT and TDFT cal-culations,[140,145] showing full agreement. The broad binding energy spectrum of the electrons pho-toemitted from the HOMO originates in the same process as the optical ground state absorption spectrum: vibrational excitation of the molecule (cf. section 2.3).
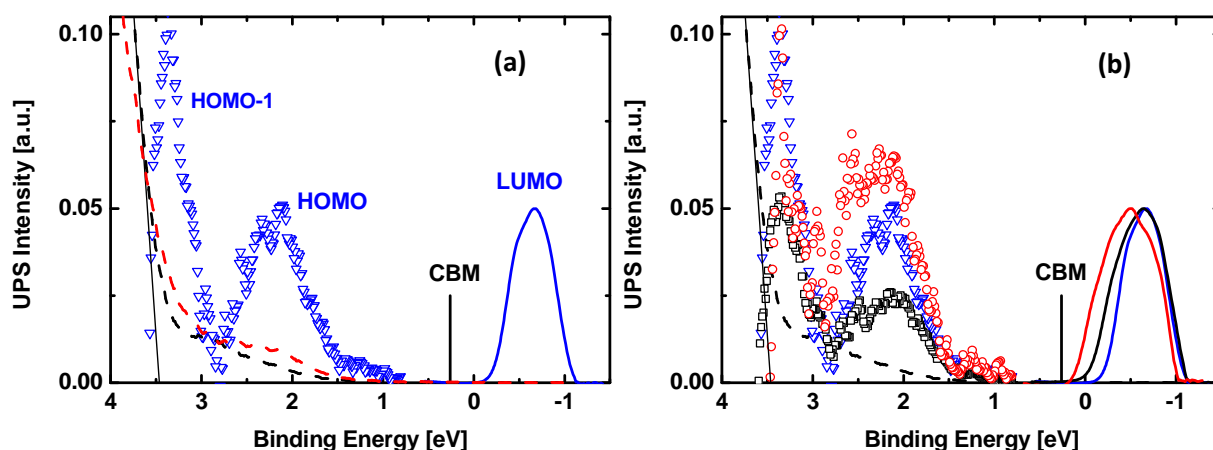

Figure 5-8 (a) UPS spectrum of bare nanorods (black, dashed) and C3 sensitized nanorods (red, dashed) in the region of the valence band edge and the (magnified) difference spectrum (blue triangles) as well as the estimated position of the C3 LUMO. (b) In addition to (a) also the difference spectra of the nanorod hybrids with C7 (black squares) and C11 (red triangles) and the corresponding estimates of the LUMOs are shown.

By adding the 3.21 eV bandgap of the ZnO nanorods (section 4.4) to the VBM, the position of the CBM can be obtained and similarly, the positions of the LUMOs can be estimated by adding the dye induced absorption spectrum of the hybrid systems to the center of the HOMO. In all cases, the LUMOs are located at least 500 meV above the conduction band minimum, which means that the so-called wide band limit is fulfilled.[151]

5.5 Injection Process

This section begins with a TA study of the molecular dynamics in the hybrid systems, followed by an analysis of the transfer-induced ZnO photoconductivity in order to encircle the intermediate state from the molecular and the semiconductor side. The discussion of the injection mechanism is completed by probing the interface dynamics with time-resolved 2PPE.

[VIII] The hybrid systems with C5 and C9 have not been measured by UPS and XPS.

5.5.1 Molecular Dynamics

Since the absorption spectra of the oxidized and excited C3-C11 overlap, state mixing has to be taken into account for the analysis. If, for example, the oxidized (excited) molecules contribute with a maximum amplitude $A^+(\lambda)$ $(A^*(\lambda))$ and the injection kinetics are exponential, the transient differential absorption reads

$$\Delta A(t > 0) = A^+ + \left(A^* - A^+\right)e^{-\frac{t}{\tau}} \qquad (5.1)$$

or equivalently

$$\Delta A(t > 0) = A^* + \left(A^+ - A^*\right)\left(1 - e^{-\frac{t}{\tau}}\right). \qquad (5.2)$$

Hence, if $A^* > A^+$, the transient differential absorption exhibits an exponential decay, but towards 0 instead of A^+. And if $A^+ > A^*$, there is an exponential rise, but starting at A^* instead of 0.
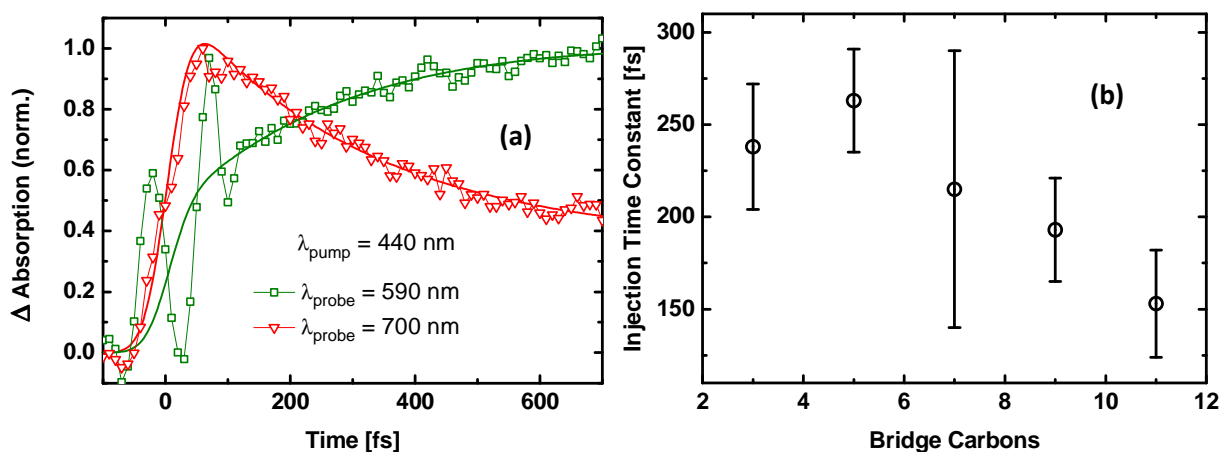

Figure 5-9 (a) Transient differential absorption of ZnO/C5 at 590 and 700 nm where the cationic respectively the excited state absorption dominates. The thick solid lines are fits according to the model explained in the text, yielding an injection time of 290 fs. (b) TA injection time constants of the perylene derivatives in dependence of the bridge length. The error bars indicate the spread of the injection times between different spots on the sample.

Figure 5-9 (a) exemplifies such a superposition of the different spectral features for the hybrid system ZnO/C5: At a probe wavelength of 590 nm and 700 nm the absorption of oxidized and excited molecules dominates and the differential absorption can be fit with (5.1) and (5.2), respectively, yielding an injection time constant τ of 290 fs. Taking this state mixing into account is very important, as otherwise the 590 nm transient could be interpreted as being biexponential or even as containing a direct charge-transfer component to the ZnO due to the 'kink' at the beginning. The oscillations in the 590 nm transient absorption signal are due to the cross phase modu-

lation between pump and probe on the glass substrate.[152] The perturbations introduced by the cross phase modulation and the overlap of cation and excited state introduce an uncertainty to the determination of the injection times in addition to the intrinsic spread due to the heterogeneity of the sample. Generally, the (average) injection time constant for each hybrid system is retrieved from several fits at different wavelengths in the visible region. However, for ZnO/C11 the state mixing is so strong in the visible region (cf. Figure 5-3 (d)), that the dynamics can only be evaluated in the NIR, where the tail of the excited state absorption dominates over the cation (Figure 5-10). Yet, all injection times measured for C3-C11 are between 130 fs and 290 fs (Figure 5-9 (b)). Considering that the LUMO of the molecules extents onto the bridge, the short injection times are explainable by an intramolecular charge transfer excitation from the chromophore to the bridge and the anchor. Interestingly, the injection times might exhibit a decreasing trend with increasing bridge length, indicating that the electronic coupling is even stronger for the longer conjugated bridges.
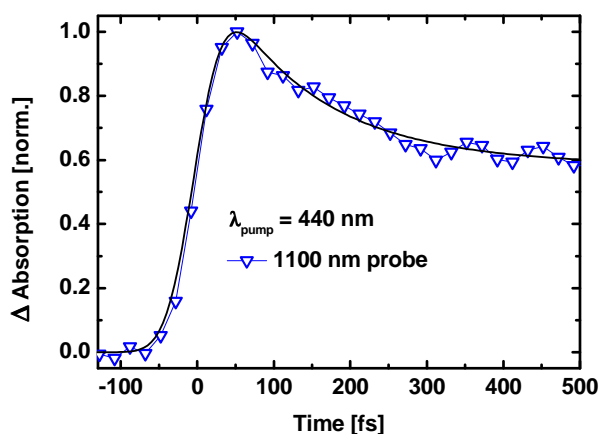

Figure 5-10 Transient differential absorption of ZnO/C11 in the NIR where the excited state dominates.

For ZnO/C3 and ZnO/C5, the excitation wavelength is varied from 500 nm to 425 nm, which does not lead to a change of the injection time within the uncertainty of the measurement. At room temperature, the molecules are in their vibrational ground state before excitation. Pump pulses with a wavelength of 500 nm are at the low energy side of the ground state absorption band of C3 and C5, i.e. there is little excess energy. So in the photoexcited molecule higher vibrational states are only weakly populated. Contrary, excitation at 425 nm leads to a significant vibrational excitation. In this case, the vibrational energy of the molecule can be converted into additional energy of the injected electron (cf. 2.3), whereas the electron is preferably injected into acceptor levels below the donor level after excitation at 500 nm, accompanied by vibrational excitation of the cation. Hence, the independence of the injection time on the excitation energy shows that the (coupling weighted) density of acceptor states does not change significantly over an energy window on the order of 400 meV around the donor level position.

5.5.2   Free-Electron Generation

After excitation with 500 nm pulses, the THz conductivity in ZnO/C3 exhibits a slow monoexponential rise within about two picoseconds. A monoexponential fit including convolution with the time resolution[IX] yields a time constant of 1.7 ± 0.25 ps (Figure 5-11 (a)). Since pumping bare unsensitized nanorods at 500 nm does not yield a measurable photoconductivity, the kinetics of the sensitized sample can be clearly attributed to electron injection. Thus, the photoconductivity rises about a factor of 7 slower than the cation absorption, which can be well seen in Figure 5-11 (a) despite of the lower OPTP time resolution in comparison to the TA experiment (about a factor of 10).
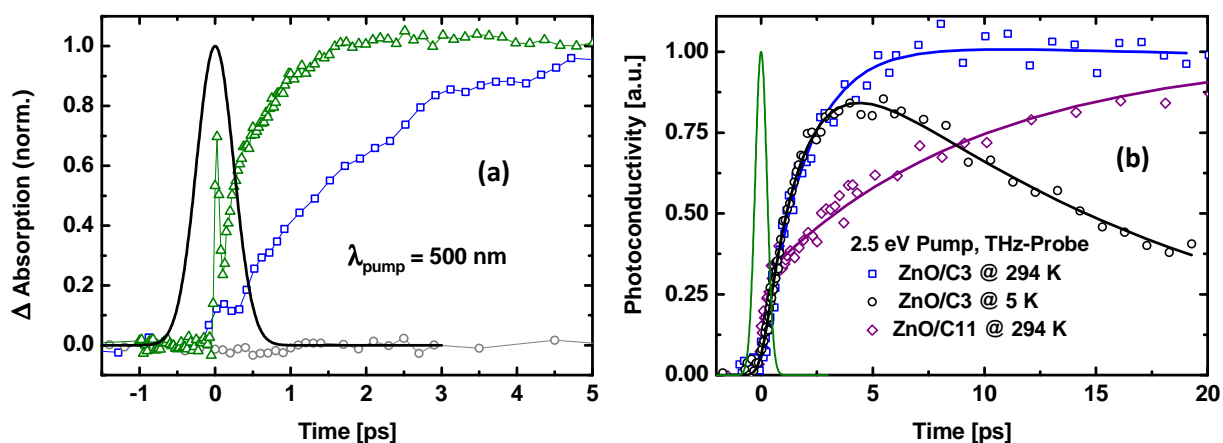

Figure 5-11 (a) Transient differential absorption of ZnO/C3 probed at 590 nm (triangles) at the maximum of the cation absorption band (Figure 5-4) compared to the transient THz conductivity of ZnO/C3 (squares) and bare ZnO nanorods (circles). The Gaussian indicates the about 0.5 ps time resolution of the OPTP setup, whereas the TA signal has a better time resolution < 100 fs. (b) Dependence of the THz kinetics on the length of the bridge unit and the temperature. The conductivity at 4.5 K was scaled down by a factor of 10. Solid lines are fits with (5.3).

The dyes with longer bridges (C5 – C11) do not exhibit monoexponential injection kinetics, as can be seen for the largest dye C11 in Figure 5-11 (b). Although the kinetics are more complicated than the simple monoexponential rise found for the smallest dye C3, qualitatively a slow-down can be observed. The transients can be analyzed by assuming two independent exponential injection pathways with contributions σ_1/σ_2 and time constants τ_1/τ_2, and a time constant τ_{rec} describing the early back electron transfer and trapping:

[IX] The time resolution was estimated from the rise of the conductivity in a ZnTe single crystal. ZnTe is very suitable for this purpose because it has a bandgap of 2.3 eV and an absorption length of 200 nm at 2.5 eV pump photon energy,[153] so that the photoconductivity is minimally affected by intraband relaxation of the excited carriers and the dispersion of pump and probe pulses in the crystal.

$$\Delta\sigma(t) = \sigma_1\left(e^{-t/\tau_{rec}} - e^{-t/\tau_1}\right) + \sigma_2\left(e^{-t/\tau_{rec}} - e^{-t/\tau_2}\right), \tag{5.3}$$

which is convoluted with the time resolution in order to fit the data. The discussion of the dynamics can be simplified by concentrating on the commonly used average injection time[154]

$$\overline{\tau} = \frac{\sigma_1\tau_1 + \sigma_2\tau_2}{\sigma_1 + \sigma_2}. \tag{5.4}$$

This average injection time exhibits a strong increase with the bridge unit length, as shown in Figure 5-12 (a). The photoconductivity $\Delta\sigma(t) = en(t)\mu(t)$ depends on the density of photocarriers $n(t)$ and their mobility $\mu(t)$. Therefore one cannot identify the change of the photoconductivity with the increase of conducting electrons if the mobility changes significantly when electrons travel from the surface to the interior of the nanorods. A recent magneto-transport study revealed that the mobility of ZnO surface electrons (in an accumulation layer) is considerably smaller than that in the bulk.[155] If there is for instance a higher defect[156] or carrier[70,147] concentration at the surface, the electron scattering rate is raised, which lowers the mobility. Also, if the acceptor state is an intrinsic surface state with a negligible mobility, the buildup of the conductivity will be limited by the reaction speed of electron transfer from the surface state to bulk states with a finite mobility. However, changes of $\Delta\sigma(t)$ due to a mobility gradient or intrinsic intermediate states depend on the nanorods rather than on the dyes. Hence, differences in the conductivity rise time between different ZnO nanorod/dye hybrid systems can be related to the specific influence of the dye. As the TA injection times are roughly constant and at least one order of magnitude smaller than the conductivity rise time (Figure 5-9 (b)), the dependence of the latter on the bridge length indicates the existence of an intermediate state, which is strongly dependent on the chemisorbed donor molecule. Thus, the injection time $\overline{\tau}$ is a measure for the lifetime of the intermediate state, which must be an immobile, localized state rather than an extended Bloch state.

According to a recent model, injected electrons are trapped at the surface because of the cation coulomb attraction,[48,126] thereby slowing down the transition to free electron bulk states. The cation LUMOs of C3-C11 are localized on or close to the chromophore and the bridges function as spacers (cf. section 5.3.2), so that the attracting force of the cations on the injected electrons should decline from C3 to C11. However, the fact that the converse trend can be observed indicates that the Coulomb attraction of the cation is not the origin of the retarded photoconductivity rise here.
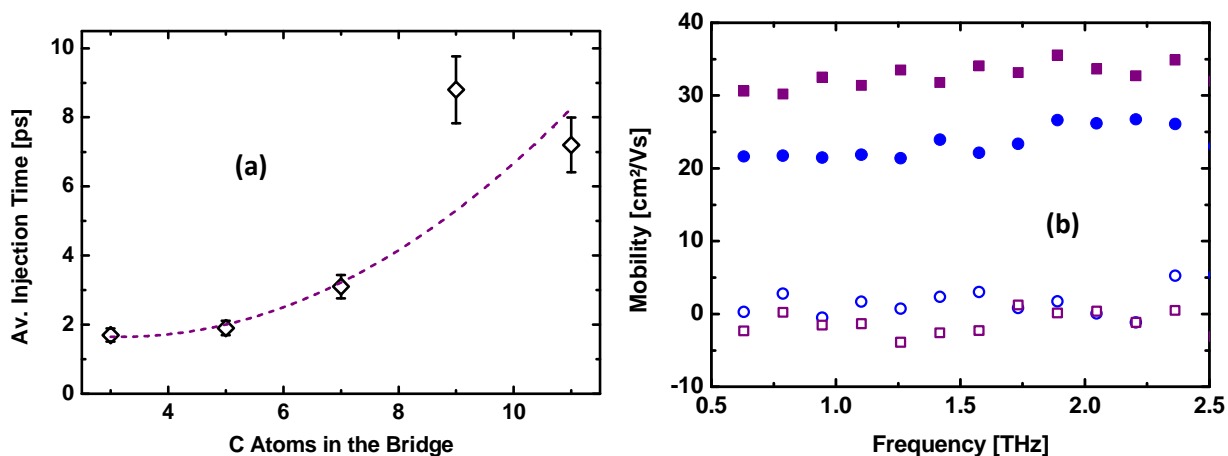
Figure 5-12 (a) Dependence of the average THz conductivity rise time (5.4) on the bridge length of the different ZnO/dye hybrids. (b) Comparison of the intra-rod mobility μ of bare ZnO nanorods (squares, sum of electron and hole mobility) and C3-sensitized nanorods (circles, electron mobility only). Bare/sensitized nanorods were excited at 400/500 nm, respectively. Filled symbols denote the real part and open symbols the imaginary part of the conductivity.

Also, if the description of the injected electron as being trapped at the surface in any kind of potential well e.g. due to the cation Coulomb attraction would be correct, a dependence of the conductivity rise time on the temperature would be expected: Overcoming the energetic barrier requires thermal action energy and tunneling through the barrier depends on the barrier width, i.e. the temperature-dependent electronic screening. However, ZnO/C3, the hybrid system with the potentially strongest cationic Coulomb attraction, exhibits no change in the conductivity rise time between room temperature and 4.5 K. This is again in disagreement with the Coulomb attraction model and also any thermally activated surface escape process such as detrapping.

The influence of the cation coulomb attraction can furthermore be evaluated by a comparison of the photoinduced mobility spectra of bare and dye-sensitized ZnO (Figure 5-12 (b)). According to a recent study by Němec et al.,[48] the mobility of ZnO nanoparticles is strongly influenced by the presence of charged molecular donors. The most striking feature was that the real part of the mobility was drastically suppressed when dye cations were present at the interface and the mobility became mostly imaginary, which is a signature of carrier localization.[10] As Figure 5-12 (b) demonstrates, this effect cannot be observed at all here; the spectral shape remains unchanged. The slight amplitude difference in the real part of the mobility can easily be explained by the fact that both electrons and holes are probed in the bare nanorods but only the injected electrons in the sensitized nanorods. Additional uncertainties in the mere amplitude arise from the free carrier generation efficiency, the optical absorption, and the photo degradation of the dye molecules. Although a hypothetical influence of the attached cations would presumably be less pronounced in the nanorods compared to the smaller nanoparticles in the study of Němec et al.,[48] the fact that

no change of the intra-rod transport can be asserted is a further indication that the hole on the dye has no particular influence on the injected electrons.

5.5.3   Transient Energetics at the Interface

Figure 5-13 exhibits kinetic energy spectra of photoemitted electrons from $ZnO(10\bar{1}0)$/C3 after selective excitation of the dye with 2.5 eV photons as in the OPTP experiments. Since the electrons are believed to be emitted from within a depth of only 1.5 nm,[132] 2PPE probes the very interface region. Bare $ZnO(10\bar{1}0)$ exhibits no measurable 2PPE under the same conditions, confirming that all 2PPE dynamics emanate from the excited molecules. The 2PPE kinetic energy spectra are dominated by the secondary electron peak around 250 meV, which dominates the underlying spectrum of directly emitted, unscattered electrons. The photoionization spectrum of the excited molecule as well as of the injected electrons is expected to be rather broad without any sharp spectral features. Apart from inhomogeneous broadening, which can also be strong on single crystals,[129] this is due to changes of the molecular vibrational state during electron injection and photoionization, , which was detailed for perylene derivatives anchored to TiO_2.[129]
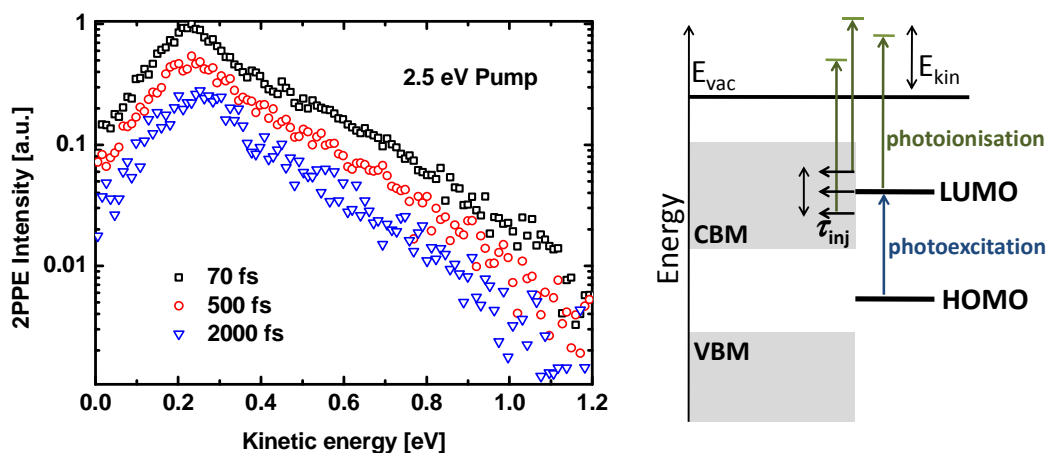
Figure 5-13 2PPE spectra of the hybrid system $ZnO(10\bar{1}0)$/C3 at different pump-probe delays. The scheme exemplifies the relation between the kinetic energy and the energetic position of the original state from which the electron is lifted above the vacuum level, i.e. the excited state of the dye and surface-near acceptor states.

The spectrum at a pump-probe delay time of 70 fs in Figure 5-13 corresponds to maximum signal amplitude. Judging from the TA, the majority of the molecules has not yet undergone electron transfer at this time delay (Figure 5-9), whereas after 500 fs the cation formation is mostly complete, and 2 ps is the characteristic rise time of the photoconductivity (Figure 5-11). During these processes the 2PPE spectrum decreases in amplitude but retains its shape. The decay dynamics of the 2PPE spectrum is multiexponential and sustain over many ps (Figure 5-14 (a)). After a few

hundred fs, the contributions from excited dyes have faded out, and the photoelectrons solely originate from injected electrons. These long lifetimes of ZnO-related photoelectron contributions are completely different from the dynamics of surface-near electrons emitted after band-band excitation of bare $ZnO(10\bar{1}0)$, which have a lifetime on the order of only some 10 fs when excited to at least 100 meV above the conduction band minimum.[149] Ultrafast relaxation of (bulk) electrons in ZnO was also found in a theoretical study and explained with strong electron-phonon coupling.[157] Hence, the exceptionally long 2PPE lifetime here gives strong evidence that the primary acceptor states of HET are neither conduction band nor intrinsic surface states, however, the intermediate states have to be localized at the interface, due to the low 2PPE escape depth.

The 2PPE transients can be modeled by regarding photoionization of the excited dyes, and photoemission from primary acceptor states at the interface and from free electron conduction band states. Denoting the population of excited molecules, intermediate acceptor states, and final free electron states with n_i, n_{im}, and n_f, respectively, and assuming exponential transfer kinetics yields

$$\frac{dn_i}{dt} = -\frac{n_i}{\tau_1}$$

$$\frac{dn_{im}}{dt} = \frac{n_i}{\tau_1} - \frac{n_{im}}{\tau_2} \tag{5.5}$$

$$\frac{dn_f}{dt} = \frac{n_{im}}{\tau_2} - \frac{n_f}{\tau_3},$$

which can be solved analytically. The rate equations describe the transient changes in the populations due to electron injection into intermediate acceptor states (τ_1) and subsequent transfer to bulk states (τ_2). Finally, a third time constant τ_3 describes the decay of the free electron population due to recombination, trapping, bulk escape. To fit the 2PPE data, each of the populations is weighted with a different amplitude, which acts as additional fit parameter, due to possible variations of the transition matrix elements. Hence the 2PPE signal is fit with

$$A_i n_i\left(t;\tau_1\right) + A_{im} n_{im}\left(t;\tau_1,\tau_2\right) + A_f n_f\left(t;\tau_1,\tau_2,\tau_3\right), \tag{5.6}$$

which yields a very good agreement with the transients as shown in Figure 5-14 (a). The time constants τ_1 and τ_2 exhibit a slight decrease with increasing kinetic energy (Figure 5-14 (b)), which can be explained by a variation of the secondary electron background along the reaction path. Otherwise, the energy dependence of the intermediate state lifetime τ_2 may be due to the variation of the conduction band density of acceptor states. An alternative explanation for the variation of τ_1 is an ensemble of anchoring sites with different electronic coupling strengths V_{DA}, and different energetic positions of the molecular ground and excited state, so that the kinetics at each site does not depend on the pump-photon energy, but can vary with 2PPE kinetic energy if electronic coupling and energetic position of the excited state are correlated.
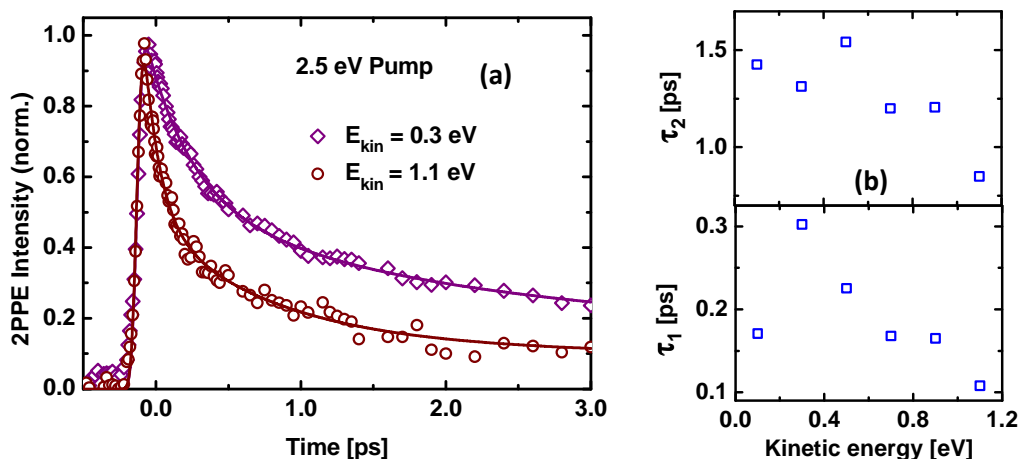
Figure 5-14 (a) 2PPE transients at two different kinetic energies (averaged over 200 meV energy windows). The solid lines are fits according to (5.6) (a) Dependence of τ_1 and τ_2 on the kinetic energy.

The average values for τ_1 and τ_2 from different 2PPE transients between 0.1 and 1.1 eV kinetic energy are 190 ± 30 fs and 1.3 ± 0.2 ps, respectively. These values are very similar to the injection time of 240 ± 35 fs from the TA measurements and the conductivity rise time of 1.7 ± 0.25 ps from the THz measurements, especially considering the fact that slightly different systems are probed. For instance the wet-chemical prepared nanorods can be expected to contain more impurities and residual coadsorbates than the elaborately prepared ZnO single crystal. This agreement strengthens the stepwise injection model (5.5).

5.5.4   Origin of the Intermediate State

In earlier studies it was suggested that the intermediate species is an exciplex originating in the hybridization of the molecular excited state and a surface localized state of ZnO.[124,125,126,48] In some cases the binding to anti binding transition of the exciplex transition was reported to be observable in the NIR.[124,125] In other cases the exciplex absorption band was claimed to overlap with the cation absorption,[48,126] but could still be identified by the fact that it absorbed stronger than the cation, so that the differential absorption at the common cation/exciplex band showed decay kinetics that coincided with the buildup of the free electron absorption. Here, there is no indication of TA in the probed spectral region between 470 nm and 1100 nm other than ground state bleaching, cation or excited state absorption, rendering the existence of an exciplex unlikely.

It has been proposed that the attracting force between positively charged cations and injected electrons traps electrons at the ZnO surface.[48,126] It was argued that this happens on ZnO, but not on TiO$_2$ surface because of the lower electrostatic screening in ZnO compared to TiO$_2$. The permittivities of ZnO ($\epsilon_\parallel = 9, \epsilon_\perp = 7.8$)[158] are indeed much lower than those of anatase TiO$_2$ ($\epsilon_\parallel = 23$, $\epsilon_\perp = 45$),[159] but so are those of SnO$_2$ ($\epsilon_\parallel = 9, \epsilon_\perp = 13.5$).[160] However, SnO$_2$ exhibits no retarded free

electron absorption even with the same dye coumarin 343 that gives a long-lived intermediate state on ZnO.[126] In the ZnO hybrids with C3-C11, the dependence of the injection kinetics on bridge length and temperature, and the unperturbed mobility spectra contradict an impact of coulomb attraction on the electron injection retardation. Therefore, it can be deduced that the coulomb attraction of the cation is not the sole and universal mechanism behind the retarded free electron signal in ZnO/dye hybrids.

The 2PPE data show that electrons are located at the interface for a time that roughly corresponds to the free electron buildup without relaxing energetically. Earlier, it was suggested that the acceptor states in HET involve adsorbate-induced interface states that are created through the formation of the chemical bonds between the dye molecules and the semiconductor surface.[130–132] The chemical coupling represent a strong perturbation so that the hybrid system cannot be broken down into molecular orbitals and semiconductor band states, i.e. into the states of the isolated components. Since the interface states are created by the interaction of both components, it is immediately understandable why the lifetimes of electrons in these states depend on both, semiconductor and dye, ranging from a few picoseconds (here) to hundreds of picoseconds,[9,48] or not being observable at all.[162,163]

5.6 Conclusions

The heterogeneous electron transfer from chemisorbed dyes at the ZnO surface was investigated for a series of perylene derivatives with systematically elongated conjugated bridge units between the chromophore and the carboxylic acid anchor group. The generation of oxidized electrons due to HET after photoexcitation was monitored with TA, while the build-up of the photoconductivity in ZnO after injection was accessed with OPTP. The time and energy dependent population of donor and acceptor states at the interface region could be monitored with 2PPE.

The electron transfer from the molecular donors into interface states does not exhibit any evidence of exciplex formation and proceeds on a time scale of about 200 fs, while the subsequent release into free electron states occurs on a significantly longer time scale of 2-10 ps. Increasing the bridge length leads to further delays in free electron generation, albeit the greater spatial separations of attracting positively charged cations and injected electrons. This and the independence of the intra-rod mobility and the THz-kinetics on the oxidized adsorbants respectively the temperature give strong evidence that the electrons are not trapped in a potential well at the surface. Since 2PPE proves that the injected electrons are localized energetically and spatially at the interface, it is concluded that the primary acceptor states are interface states created by the interaction of the adsorbates and the ZnO surface. Only the coupling of these states to the ZnO bulk states determines the rate of free electron generation. This finding shows that ZnO bulk proper-

ties such as the conduction band density of states and the permittivity are less significant for the electron transfer process than what is commonly assumed: Instead, the ZnO/molecule interface plays the key role in the heterogeneous electron transfer. This finding may assist in guiding new designs capable of reducing the detrimental effect of delayed charge formation at hybrid/ZnO interfaces.

6 CuInSe$_2$: Influence of Stoichiometry on Relaxation Processes

This chapter focuses on charge transport and early charge carrier relaxation and loss mechanisms of photogenerated electron-hole pairs in polycrystalline CuInSe$_2$ (CIS) thin films. Comparing stoichiometric and heavily compensated, off-stoichiometric solar cell grade CuInSe$_2$ exposes the profound influence of electrostatic potential fluctuations on the charge transport in the latter material. It is shown that the composition drastically affects the recombination kinetics and strongly reduces the charge carrier lifetime in stoichiometric CIS. This is tentatively attributed to the effect of an intrinsic defect: the Cu$_{In}$ antisite.

Parts of this chapter are in preparation for publication in Physical Review B.

6.1 Motivation

Solar cells based on chalcopyrite semiconductors are a promising thin film solar cell technology. The reasons for the importance of this technology include low-cost production and high photovoltaic performance. Cells that are based on the ternary absorber CuInSe$_2$ reach efficiencies up to 15 %,[164] and the present record efficiency for optimized cells with Cu(In,Ga)Se$_2$ absorber is as high as 20.3 %.[6] Alloying CIS with Ga on the In-sublattice leads to beneficial effects like an increased bandgap and a reduction of the defect concentration.[165,166] To attain highest performance, the absorber is grown with a Ga/(Ga+In) ratio of about 0.3 and a Cu/(Ga+In) ratio of 0.8 - 0.92.[167] With this Cu-poor composition, CIS has a tremendous amount of intrinsic point defects such as Cu vacancies or In$_{Cu}$ antisites.[I] Point defects that act as donors almost cancel out with those that act as acceptors, so that the material exhibits a high degree of compensation.[168,169] Hence, there are far less charge carriers than charged defects, and the electric field of the ionized impurities cannot be effectively screened. Since the distribution of defects is not homogenous on the nanoscale, clusters of charged defects cause a spatially fluctuating electric potential. The implications of these potential fluctuations - accumulation of charge carriers in the electrostatic potential wells – are claimed to be manifested in the PL.[117,168–179] Hitherto, the consequences of this spatially fluctuating potential for the charge transport in CIS have not been discussed.

[I] In total, there are 12 different intrinsic point defects: 3 interstitials, 3 vacancies and 6 antisites.

The question why stoichiometric (also termed Cu-rich) $CuInSe_2$ performs worse than Cu-poor CIS in solar cells although the former has a smaller point defect density is still not understood. Though the PL lifetime in stoichiometric CIS is lower than in Cu-poor CIS,[180] which indicates that short lifetimes are an intrinsic, detrimental feature of stoichiometric CIS, an explanation why Cu deficiency leads to increased charge carrier lifetimes has not yet been given. So far, it is not even clear whether Cu-rich CIGS performs worse because of a higher recombination at the heterointerface with the commonly used CdS buffer[181,182] or because of recombination in the bulk.[180]

In this chapter, OPTP spectroscopy is employed to gain a deeper understanding of how the composition affects the charge transport and relaxation in $CuInSe_2$. In contrast to TRPL, OPTP does not suffer from the artifact that a spatial separation of electrons and holes leads to a seemingly shorter charge carrier lifetime. The sub-ps time resolution is utilized to pay special attention on fast relaxation processes, which (partly) precede the electron-hole recombination.

6.2 Material Properties

6.2.1 Structure and Defect Physics

$CuInSe_2$ is a I-III-VI$_2$ semiconductor that usually displays p-type conductivity, but can become n-type under Cu-rich but Se-poor growth conditions.[7] It condensates in the tetragonal chalcopyrite crystal structure (space group $I\bar{4}2d$),[183] which is named after the mineral 'chalcopyrite' ($CuFeS_2$). With lattice constants of a = b = 5.78 Å and c = 11.62 Å for the principal axis,[183] the cuboid convential unit cell, depicted in Figure 6-1, has a volume of $a^2c = 389$ Å^3. The primitive unit cell is half as big and is spanned by the primitive vectors

$$\vec{a} = \begin{pmatrix} a \\ 0 \\ 0 \end{pmatrix}, \ \vec{b} = \begin{pmatrix} 0 \\ a \\ 0 \end{pmatrix} \text{ and } \vec{c} = \frac{1}{2}\begin{pmatrix} a \\ a \\ c \end{pmatrix}. \tag{6.1}$$

The basis of the primitive unit cell consists of eight atoms and accordingly, there are 21 optical phonon modes. $CuInSe_2$ is well known for its complex defect physics that originates in a variety of intrinsic point defects such as cation (Cu,In) antisites or vacancies. The capacity of CIS to tolerate large off-stoichiometries lies in its ability to compensate the off-stoichiometry by the formation of intrinsic defects. Just from a consideration of the stoichiometry deviation, it can be seen that the defect concentration must be extraordinarily high. For a single phase chalcopyrite crystal with the composition $Cu_{0.95}In_{1.05}Se_2$ (Cu/In = 0.9), the defect concentration can be estimated from the off-stoichiometry and the atom density n_a to be at least $1/4 \cdot 0.05 n_a \approx 5.1 \cdot 10^{20}$ cm^{-3}. And indeed, recent neutron scattering experiments have shown that $CuInSe_2$ remains in the chalcopyrite phase down

to Cu/In ~ 0.8 while exhibiting a (composition-dependent) point defect density on the order of several 10^{20} cm^{-3}.[184]

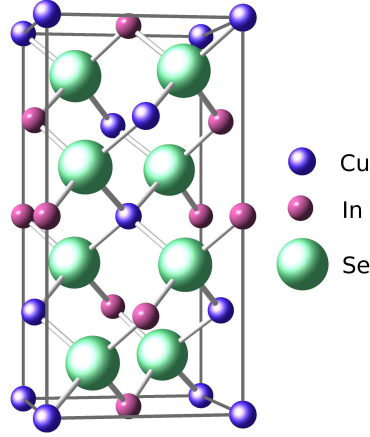Figure 6-1 Convential unit cell of CIS in the chalcopyrite structure.

In the past, the defect pair In_{Cu}-$2V_{Cu}$ was attributed an important role in the defect physics because it was thought of to have a remarkably low formation energy.[185,186] Most recent theoretical results contradict this previous notion: Though the formation energy of the In_{Cu}-$2V_{Cu}$ defect pair was found to be much lower for In-rich than for Cu-rich growth conditions, it was not identified as a particularly important defect.[187] Rather, it was shown that under Cu-rich growth the antisite defects Cu_{In} and In_{Cu} and the copper vacancy V_{Cu} are the most important defects, and the intrinsic Fermi level is at about 0.3 eV above the VBM. In the same study, In_{Cu}, V_{Cu} and the defect pair In_{Cu}-V_{Cu} were identified as the intrinsic defects with the lowest formation energy under Cu-poor growth conditions, leading to an intrinsic Fermi level at about 0.4 eV above the VBM. Since V_{Cu} acts an acceptor,[186] Cu_{In} as a localized hole trap,[187] and In_{Cu} as a donor,[186] the defects (partly) compensate each other, so that the net charge carrier density can be orders of magnitude lower than the defect concentration.

Table 3 Important material parameters of CuInSe$_2$.

Parameter	Value	Source
Mass density ρ	5.74 g/cm^3	atomic weight + unit cell volume
$\epsilon(0)$	11.3	Ref. 188
$\epsilon(\infty)$	7.75	Ref. 189
c_l	3770 m/s	Ref. 190
D_{ac}	9.39 eV	Ref. 191
$\hbar\omega_{op}$	25 meV	Ref. 192
a_B	7 nm	$a_B = 4\pi\epsilon_0\epsilon_r\hbar^2 / (m^* e^2)$
α (1.55 eV)	$7.5 \cdot 10^4$ cm^{-1}	Ref. 193
m_e^*	0.08-0.09	Ref. 194–198

6.2.2   Electronic Structure and Transport

The electron effective mass has been estimated from Hall measurements at 0.09 m_e,[198] and from intervalence band absorption measurements, hole masses were determined as 0.71 m_e (heavy holes), 0.092 m_e (light holes) and 0.085 m_e (split-off band).[199] According to recent theoretical calculations, the conduction band effective mass is slightly anisotropic with $m_\parallel = 0.09 m_e$ and $m_\perp = 0.08 m_e$ at the Γ-point, and the valence band effective masses are strongly anisotropic.[195] Figure 6-2 (a) shows the dispersion of the inverse effective mass around the center of the Brillouin zone in an energy interval that roughly corresponds to the range of occupied electronic states at room temperature. The strongly anisotropic and non-parabolic character of the valence bands complicates a discussion of hole transport. However, it can be argued that the contribution of holes to the photoconductivity, which scales as $1/m^*$, is small compared to that of electrons because the majority of holes is created in the heavy hole band by the 1.55 eV pump photons.[II] Though heavy holes can eventually be scattered into the light hole band, which is separated energetically by about 10 meV, the following discussion will make use of the simplifying approximation that the hole mobility can be neglected compared to the electron mobility. Also, the non-parabolicity of the conduction band will not be taken into account, which seems to be a reasonable approximation (Figure 6-2 (b)) and allows for using the formalism of section 2.2.3.

In single crystalline CIS that is not intentionally grown off-stoichiometric, electronic conduction is realized by band transport,[200] so the mobility is determined by the scattering mechanisms of extended Bloch states (cf. section 2.2). Typically, the mobility first rises with decreasing temperature because of reduced phonon scattering and then decays as $T^{-1.5}$ after an intermediate maximum because charged impurity scattering gets more efficient at low temperature. Amplitude and position of this maximum depend, amongst other things, on the impurity concentration. Reported values for the electron Hall mobility in single crystals under ambient conditions vary between 100 and 1000 cm^2/Vs.[200–203] Depending on compensation and impurity concentration, band transport may not be the dominant conduction mechanism at very low temperatures any more, when very few charge carriers are present in the bands. If the impurity concentration N is very high ($N \approx 1/a_B^3 = 3{\cdot}10^{18}$ cm^{-3}), the wave functions of neighboring impurities overlap and an impurity band is formed, which may dominate the transport with metal-like properties.[204] At low temperature and low impurity concentration, charge transport in CIS occurs through transitions over adjacent acceptor/donor levels, i.e. through hopping.[202,205,206]

[II] Heavy holes are generated preferably instead of light holes because the heavy hole band has a relatively high density of states, owing to the flatter energy dispersion (the DOS scales as $m^{*3/2}$).
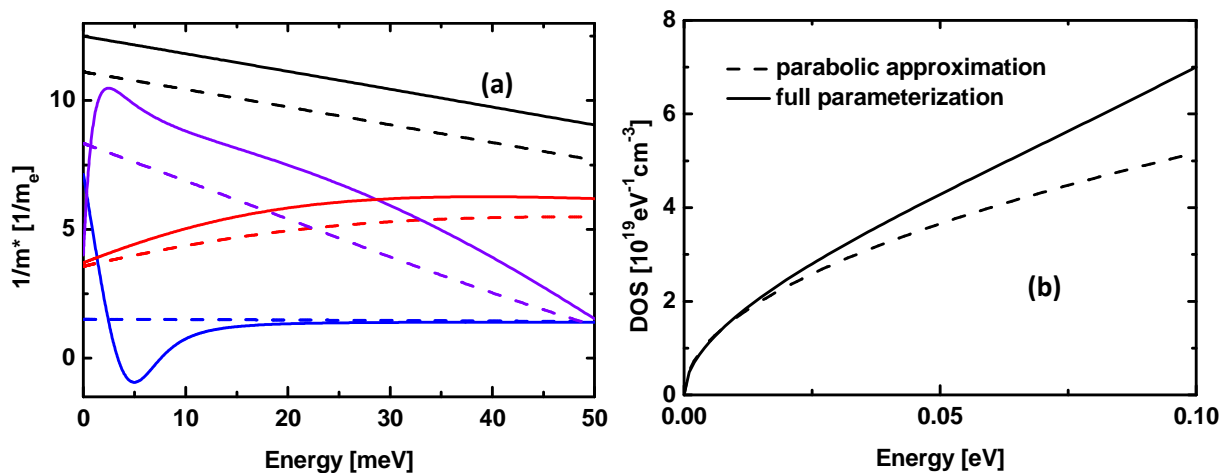
Figure 6-2 (a) Dispersion of the inverse effective mass along the [100] (solid lines) and the [001] (broken lines) direction for the conduction band (black) and the heavy hole (blue), light hole, (violet) and split off (red) valence band. The numerical values are calculated according to a full band parameterization.[194] (b) Comparison of the density of states calculated within the parabolic band approximation (broken line) and within the full band parameterization.[194]

For polycrystalline CIS thin films, in addition to the above considerations, also the grain boundaries have to be regarded. They can act as (energetic) barriers, which especially impede long range transport.[116] Energetic barriers at grain boundaries can generally arise from an accumulation of charged trap states.[116] Specifically in chalcopyrites, also charge neutral grain boundaries have been predicted theoretically[207,208] and recently been observed[209] to pose energetic barriers. Electrical measurements on polycrystalline CIS have shown a limiting influence of grain boundaries on charge transport and a thermally activated[III] mobility.[210–214] Reported values for the electron mobility in polycrystalline CIS do not exceed a few tens of cm²/Vs at room temperature, and thus they are much smaller than those measured on single crystals.[210–212]

As yet another factor that controls the charge transport properties in CIGS the coexistence of extended and localized states separated energetically by a mobility edge[120] was proposed.[215,216] This localization, which was thought of to arise from the compositional disorder (reminiscent of Anderson localization[217,218]), was introduced to explain the very small electron drift mobility of less than 1 cm²/Vs measured on solar grade CIGS.[216] The compositional disorder in off-stoichiometric CIS goes along with point defects that can act as donors or acceptors. It is known that CIS generally has a high density of ionized defects and a high degree of compensation at the same time, so that there are few charge carriers to screen the electrostatic impurity potential. The

---

[III] Thermal activation means that the transport across grain boundaries happens by thermionic emission and therefore includes a Boltzmann factor $\exp\left(-E_A / k_B T\right)$.[210–212]

implications of this spatially fluctuating potential have so far not yet been discussed in the context of charge transport in CIS or CIGS.

6.2.3 Potential Fluctuations

As long as the concentration of charged defects is low compared to the concentration of free charge carriers, the impact of this perturbation can be modeled by to the Fermi golden rule as invoking transitions between iso-energetic Bloch states. This scattering mechanism is a limitation for the mobility and affects both, long- and short range transport respectively DC and AC mobility. This becomes different when the concentration of donors and acceptors and the degree of compensation is high. In this case, the spatially fluctuating electrostatic potential of the charged defects leads to a heavily structured energy landscape and the charge carriers gather in the deepest potential wells.[117,219,220] Now, long range transport necessitates tunneling or thermal activation energy E_A to overcome the energy barriers. Typical values for the mean fluctuation of the electrostatic potential in CIS, which increases with decreasing Cu/In ratio, are 20-60 meV.[168] Experimental confirmation for the occurrence of potential fluctuations in (non-stoichiometric) ternary chalcopyrites comes from a number of PL studies.[168–179]

A model of the potential fluctuations that allows for an immediate estimate of typical potential variations has been given by B. I. Shklovskii.[219] The standard deviation of a Poisson distribution with expectation value M is $\sqrt{M}$. Thus, the typical deviation of the number of charged impurities in a volume R^3 from the mean value is $\sqrt{NR^3}$, with $N = N_D + N_A$ denoting the total density of charged donors and acceptors. Without screening, the fluctuation of the impurity density leads to a Coulomb potential

$$\gamma(R) = \frac{e^2}{4\pi\epsilon R}\sqrt{NR^3}.$$ (6.2)

In a volume R^3, there is a typical excess or deficit density of charged impurities given as

$$\Delta N = \frac{\sqrt{NR^3}}{R^3}.$$ (6.3)

With increasing size of the test volume R^3 the Coulomb potential (6.2) would become unphysically large. However, since ΔN approaches 0 for big volumes R^3, any finite charge carrier density $n > \Delta N$ can always screen the potential. Therefore, only fluctuations on a scale smaller than

$$r_s = \frac{N^{1/3}}{n^{2/3}}$$ (6.4)

remain unscreened. Together with eq. (6.2) this yields the typical magnitude of the potential fluctuations

$$\gamma = \frac{e^2}{4\pi\varepsilon} \frac{N^{2/3}}{n^{1/3}}.$$ (6.5)

Carrier transport is possible by thermal excitation above the energetic barrier which contributes a factor $\exp\left(-E_A / k_B T\right)$ to the mobility, with E_A on the order of γ. In addition, tunneling through the barrier, which is proportional to $\exp\left(\sqrt{m\gamma}\, r_s / \hbar\right)$, becomes important for low enough temperature. Since both, γ and r_s drop off with growing charge carrier density, it is to be expected that the mobility increases with the excitation density.

6.3 Experimental and Technical Details

The spot size of the pump laser is kept at about 3 μm (fwhm intensity) at a maximum intensity of about 300 mW, which translates into a photon flux $I_0 = 7\cdot10^{13}$cm^{-2}. The optical absorption coefficient α of CIS at 800 nm is about $7.5\cdot10^4$ cm^{-1} and the refractive index at 800 nm is reported to be about 2.9.[193] Calculating the reflectance R of a thin film with these parameters (cf. section 8.2) gives a value of 25 ± 0.5 % if the thickness is greater than 500 nm. So the maximally achievable electron-hole pair density (averaged over the absorption length) can be estimated at $0.63\cdot I_0 \left(1-R\right)\alpha \approx 3\cdot10^{18}$ cm^{-3}, while the minimum density, where with a strongly attenuated pump a photoconductivity can still be measured, is about $5\cdot10^{15}$ cm^{-3}.

If not stated otherwise all measurements are performed under high vacuum and the samples are stored in a vacuum chamber between measurements because it is reported that exposure to air degrades CIGS.[221,222]

6.3.1   Sample Preparation

CIS layers are grown by physical vapor deposition on c-oriented sapphire substrates by a multi-stage process. During the first stage, selenium and indium are evaporated simultaneously on the substrate, which was kept at a temperature of 330 °C. In the second stage, selenium and copper are deposited, while the substrate is kept at 550 °C. If the samples are intended to have a Cu-poor composition, a third stage with selenium and indium deposition follows. The higher substrate temperature in the second and third stage facilitates a diffusive mixing of the different components.[223] After growth, the samples were kept in vacuum to minimize degradation effects.[221,222] If not stated otherwise, Cu-rich samples were immersed in KCN before the measurements. KCN is known to etch away copper selenide phases[224] and oxides[225] at the surface.

Under standard processing conditions, CIGS absorber layers for solar cells are grown on molybdenum coated soda-lime glass substrates, which has the benefit that its thermal expansion coefficient is close to that of CIS (Figure 6-3). A drawback of soda-lime glass is that it is not transparent

to THz radiation, and regarding temperature dependent measurements, its relatively low heat conductivity is a limitation. Sapphire substrate is not only transparent to THz radiation but also has a much better heat conductivity than soda-lime glass. Beneficially, the thermal expansion of sapphire is also very similar to that of CIS (Figure 6-3). So elastic stress due to the mismatch of the expansion coefficients of substrate and CIS absorber layer will not play a completely different role in sapphire compared to the standard material. The use of soda-lime glass under standard conditions leads to a natural supply of sodium during the growth, which has long been known to be beneficial for the cell efficiency.[226] In order to test whether sodium has an effect on the charge carrier dynamics, Cu-poor CIS was optionally deposited on sapphire with an 8 nm thick NaF precursor layer.
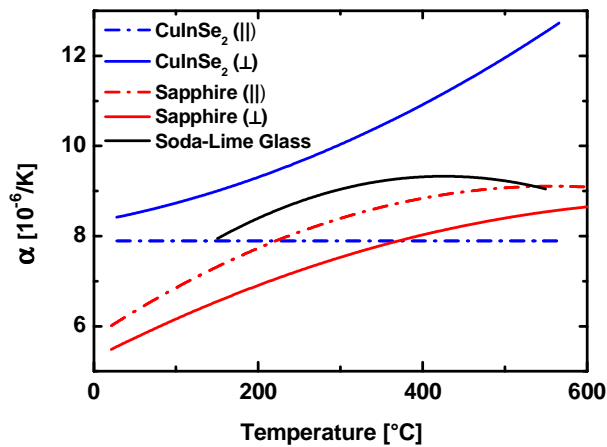

Figure 6-3 Thermal expansion coefficients, parallel and perpendicular to the principal axis, of CIS and sapphire, and the isotropic expansion coefficient of soda-lime glass. The values for CIS, sapphire and soda-lime glass are taken from Ref. 183, 227 and 228, respectively.

The resulting composition of Cu-rich and Cu-poor samples was measured with X-ray fluorescence (XRF) spectroscopy and is given in Table 4. The Cu/In ratio of the Cu-rich process is 0.97, i.e. stoichiometric within the uncertainty of the XRF measurements. The Cu/In ratio of the Cu-poor process is 0.86, which is typical for solar cell grade CIGS.

Table 4 Composition of Cu-rich and Cu-poor samples as measured with XRF.

	Cu	In	Se
Cu-rich	24.73 %	25.45 %	49.81 %
Cu-poor	22.83 %	26.48 %	50.70 %

The morphology of the CuInSe$_2$ films was investigated with SEM (Figure 6-4). Cu-rich films consist of grains with a typical size of about a micrometer, while Cu-poor films have smaller grains

with a diameter on the order of several 100 nm. However, Cu-poor $CuInSe_2$ grown with an additional NaF precursor layer has very large grains with a size of several micrometers.
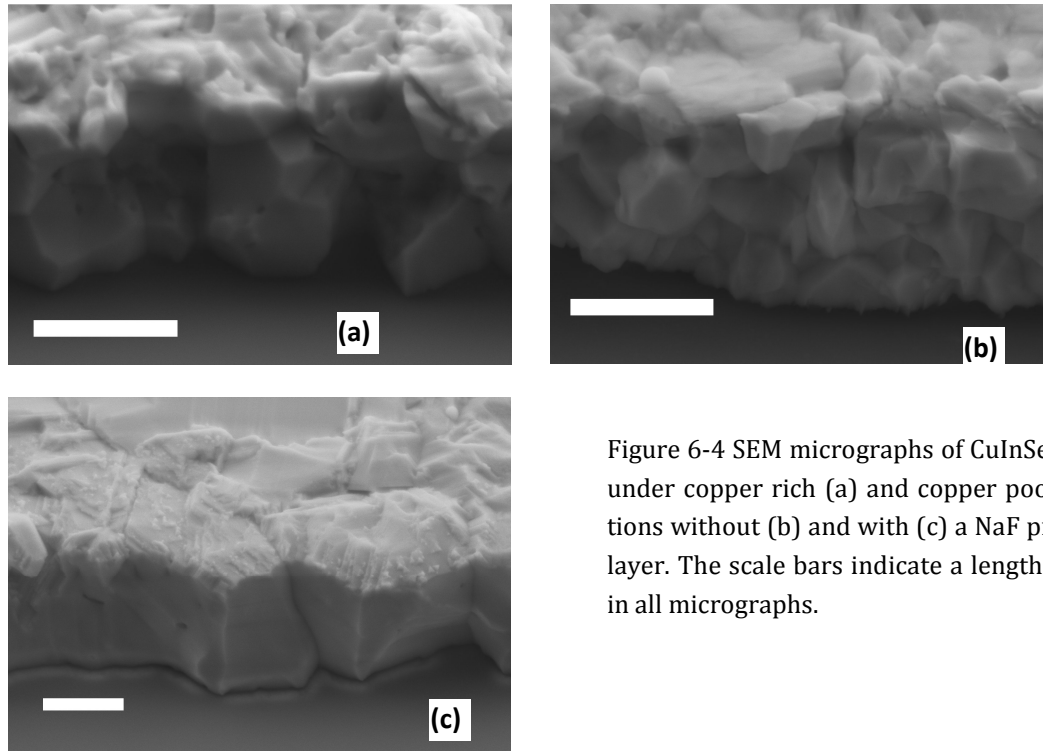

Figure 6-4 SEM micrographs of $CuInSe_2$ grown under copper rich (a) and copper poor conditions without (b) and with (c) a NaF precursor layer. The scale bars indicate a length of 1 µm in all micrographs.

6.4 Stoichiometric CuInSe$_2$

This section starts with characterizing PL measurements, which show that the typical PL of (single-) crystalline, stoichiometric CIS can be reproduced. It turns out, that the charge transport can be described very well by the simple Drude-like theory of section 2.2.3. Hence, the momentum relaxation time (MRT) can be derived from the spectral dependence of the photoconductivity. This allows for a detailed description of the limiting scattering mechanisms and yields insight into the cooling dynamics of hot electrons. Also, mobility effects can be separated from the time-dependent decay of the photoconductivity, thereby enabling an unambiguous determination of the charge carrier lifetime, which is analyzed and a model for the recombination is proposed.

6.4.1   Photoluminescence

PL yields information on the energetic position of states in the forbidden region that play a role for the recombination. By means of time resolved PL (TRPL), it is also possible to draw conclusion on the charge carrier lifetime. Recently, it was shown that the PL lifetime of CIGS depends strong-

ly on the chemical environment under which the samples are stored. Exposure to air severely lowers the PL lifetime, which also happens to a lower degree to samples stored under nitrogen atmosphere.[221,222] Many earlier PL studies were performed without a special control of chemical environment or sample history. Hence, conclusions from these studies have to be treated cautiously.

Temperature and intensity dependent PL measurements are executed under vacuum conditions using a closed cycle cryostat. The samples were excited with a continuous wave laser at a wavelength of 660 nm. The maximum intensity, corresponding to neutral density (ND) 0,[IV] was 93 W/cm². A typical order of magnitude charge carrier lifetime for high quality CIGS absorbers is 10 ns.[229] With this lifetime and an absorption coefficient of $1.1 \cdot 10^{15}$ cm^{-1},[193] the photo-generated charge carrier density can be estimated to be on the order of 10^{17} cm^{-3}. This is an order of magnitude lower than the maximally achievable excitation density in the OPTP measurements, but the charge carrier density range in both experiments still overlaps.
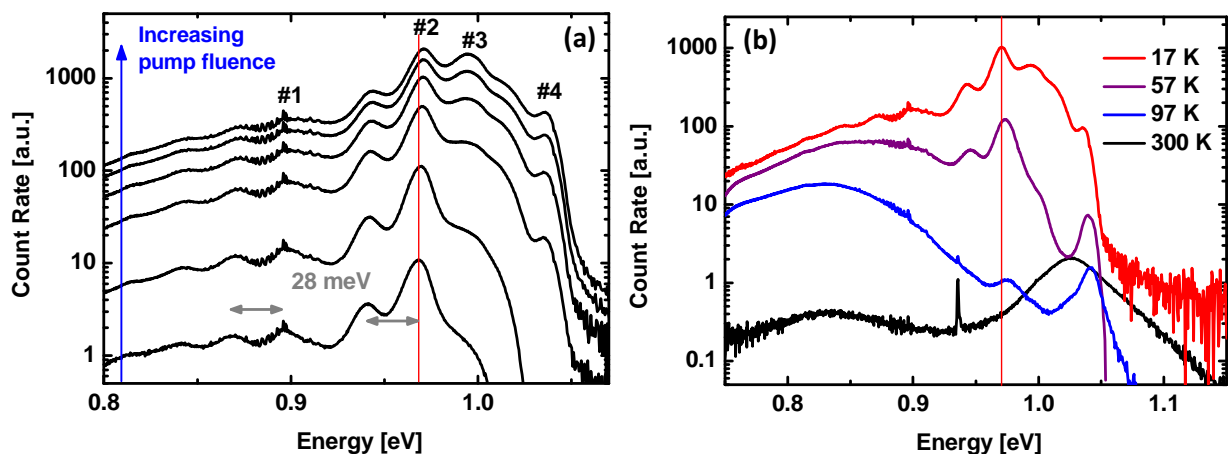

Figure 6-5: (a) Intensity dependent PL spectra of Cu-rich CIS at a sample temperature of 17 K. The bottom curve corresponds to ND3 and the uppermost curve to ND0. The red vertical line serves to point out the slight blue shift of the peak position with increasing illumination intensity. The grey arrows indicate the longitudinal optical phonon replica of peak #1 and #2, which are separated by about 28 meV from the zero phonon line.[230] (b) Temperature dependent PL spectra of Cu-rich CIS at ND0.5.

As shown in Figure 6-5 (a), the luminescence of Cu-rich CIS exhibits several well resolved emission peaks at a very low sample temperature of 17 K. The peaks at energies $\geq 1\,\text{eV}$ depend much stronger on the excitation power than those at energies $< 1\,\text{eV}$, which display a blue shift on the order of 1 meV per decade of increased excitation power. However, at intermediate temperatures,

---

[IV] A ND x filter denotes a spectrally almost constant optical attenuator that reduces the transmission by a factor of 10^{-x}.

where these peaks are less pronounced but still present, this intensity-dependent shift cannot be observed any more. Increasing the temperature from 17 K to room temperature lets the sharp emission peaks shift blue and decrease in amplitude until they finally disappear while broad absorption bands centered at about 0.83 eV and 1.025 eV are formed (Figure 6-5 (b)). The PL spectra exhibit no indications of band-band transitions, so that the dominant recombination process occurs through defects states or, at low temperatures, involves radiative recombination of (bound) excitons.

The observation of sharp emission peaks in Cu-rich CIS and their blue shift with increasing pump intensity or temperature (at low temperatures) is in agreement with previous studies.[230–235] The peak with the highest transition energy has generally been assigned to excitonic recombination. Depending on the study, the other peaks were assigned to free to bound or donor-acceptor pair (DAP) transitions. Both transition types lead to the same qualitative blue shift of the peak positions when temperature or pump intensity are raised. For free to bound transitions, the temperature effect is due to the increased kinetic energy of the free carrier, and the shift with increasing intensity is due band filling. In the DAP transition model, a trapped electron and a trapped hole, with a spatial separation R, recombine by emitting a photon, whose energy is determined through[230]

$$\hbar\omega + N \cdot \hbar\omega_{L0} - \frac{e^2}{4\pi\epsilon\epsilon_0 R} = E_{gap} - E_D - E_A \tag{6.6}$$

because the energy of the products (1 photon, N longitudinal optical phonons, and the ionized defects) must equal the energetic difference of donor and acceptor level. Here, E_D and E_A are the donor and acceptor binding energies, and the third term on the lhs of eq. (6.6) describes the potential energy of positively charged donor and negatively charged acceptor. This model predicts a blue shift of the luminescence with increasing excitation power because the average recombination distance R decreases. Furthermore, it also predicts a blue shift with increasing temperature because distant pairs exhibit a long lifetime and are predominantly ionized before they recombine, so that the recombination is dominated by pairs with smaller separations and thus higher luminescence energies.

An inspection of the Coulomb term in eq. (6.6) allows for an estimate of the maximally achievable intensity-dependent shift of the luminescence bands. Extreme low excitation corresponds to $R \rightarrow \infty$ (0 meV), and the high excitation limit corresponds to the filling of all available defect states, which relates to R = 10 nm for a reasonable impurity density on the order of 10^{18} cm^{-3} (cf. section 6.4). Hence, the maximally achievable shift can be estimated at 13 meV.

Table 5 Observed PL transitions in Cu rich CIS and their assignments.

Peak	Energy [eV]	Transition
#1	0.896	Donor-Acceptor
#2	0.968	Donor-Acceptor
#3	0.995	Bound exciton
#4	1.036	Bound exciton

Because peak #1 and #2 can be observed for very low pump intensities and exhibit the character-istic excitation density dependence, they are assigned to DAP transitions. In the literature, peak #3 and #4 have been explained with free to bound, bound or free exciton, or DAP transitions.[231–235] Here, an assignment of these peaks to free excitons can be excluded because the peak positions are not consistent with the 1.05 eV band gap[236] and the 8 meV exciton binding energy.[237] An iden-tification of these peaks with DAP transitions also fails because the peak position is insensitive to a variation of the pump intensity. The same applies to free to bound transitions, because band filling effects would imply a blue shift on the order of 10 meV in the low temperature PL (Figure 6-6).[v] Excitons may form complexes with defects thereby increasing the total binding ener-gy,[238,239] and it seems likely that peak #3 and #4 can be ascribed to bound excitons. A slight blue shift with increasing temperature can be observed for peak #4, which is attributed to the abnor-mal, positive correlation of CIS band gap and temperature below about 100 K.[240]
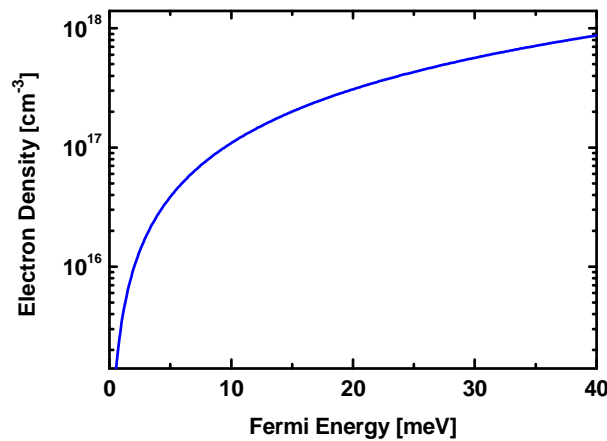

Figure 6-6 Dependence of the electron density on the Fermi level (referenced to the CBM) at 5 K in CIS.

---

[v] Assuming a reasonable lifetime of 10 ns (cf. section 6.5.3), the maximum excitation density in the PL ex-periments was estimated at 10^{17} cm^{-3}.

6.4.2   Hot and Cool Electron Transport

Figure 6-7 demonstrates that the mobility spectrum of Cu-rich CIS exhibits the functional form

$$\mu = \frac{e}{m^*}\frac{\tau_D}{1-i\omega\tau_D} \tag{6.7}$$

of a simple Drude spectrum in the frequency range from about 0.7 THz to 2.7 THz.[VI]
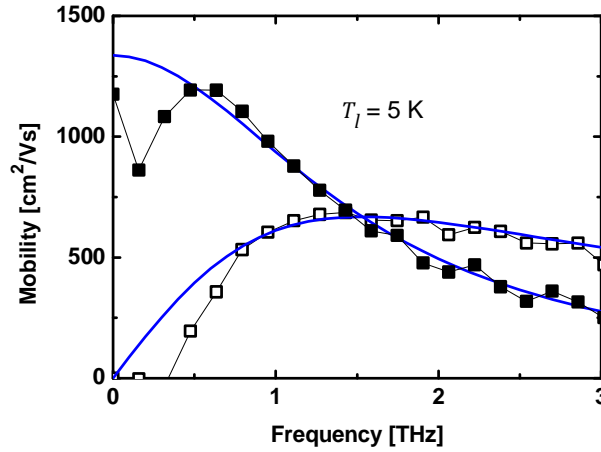

Figure 6-7 Mobility spectrum of Cu-rich CIS at a lattice temperature T_l = 5 K, a pump-probe delay of 3 ps, and a photogenerated electron-hole pair density of about $5.3\cdot10^{16}$ cm^{-3}. Solid lines are fits according to the Drude model (6.7) with τ_D =105 fs, and m^* = 0.14 m_e.[VII] Full/open symbols denote the real/imaginary part.

As outlined in 2.2.3, the functional form of eq. (6.7) is an approximation for a more fundamental theory of the mobility. The parameter τ_D, which is retrieved from fitting eq. (6.7) to the experimental mobility spectra, can be regarded as an approximation of the MRT $\langle\tau\rangle$ defined in (2.41), which controls the $\omega\rightarrow0$ limit of the mobility: $\mu = e\langle\tau\rangle/m^*$.[VIII] In this section, mobility spectra are simulated with the more fundamental methodology of eq. (2.40), taking reasonable scattering mechanisms into account. These simulated spectra can be well fit with the Drude model (6.7), and

---

[VI] Outside this range, the data becomes increasingly unreliable due to a lack of spectral density in the probe pulses. Additionally, the low frequency data is progressively affected by the finite size of the pump beam (cf. section 3.2).

[VII] A possible origin for the discrepancy of the effective mass m^* = 0.13 m_e that is retrieved from the Drude fit and the literature value of the effective mass $m_e \sim 0.08$ (Table 3) is discussed in section 6.4.5.

[VIII] In this chapter, the mobility is sometimes discussed in terms of the extrapolated DC mobility because the latter allows for an easier comparison with drift or Hall mobility literature values. Of course, the mobility cannot be probed for $\omega\rightarrow0$ here, so it is not known if the DC mobility is actually given as $e\tau_D/m^*$ or if it deviates to lower values because of inhibited long range transport (grain boundaries).

the retrieved τ_D agrees within 15 % with the calculated $\langle\tau\rangle$ (as shown in the appendix in 8.6). Hence, fitting (6.7) to the experimental as well as the simulated spectra yields a good approximation of the momentum relaxation time $\langle\tau\rangle$ and allows for an easy comparison of measured and simulated mobility spectra.

Figure 6-8 (a) exhibits the relaxation time τ_D derived from experimental data with (6.7) in dependence of the sample temperature for pump-probe delays of 2, 20 and 200 ps. At a short pump-probe delay of 2 ps, the relaxation time rises from 60 fs at room temperature to 120 fs at 5 K. Accordingly, also the mobility roughly doubles. At a longer pump probe delay of 20 ps, the relaxation time still exhibits an increase but only by about 20 fs. 200 ps after the excitation pulse, the temperature dependence of the relaxation time has an intermediate maximum around 80 K and thereafter decreases to 40 fs at 5 K. This qualitative trend is typical for a situation where the transport is limited by charged impurities at low temperatures and phonon scattering at high temperatures and has been observed in several studies[200–202,204,211] on the Hall mobility of CuInSe2.[IX] Since Hall mobility measurements do not involve optical excitation, it is reasonable to presume that the temperature dependence of the MRT at 200 ps pump-probe delay represents a relaxed situation where the photocarriers have equilibrated to the lattice temperature. Accordingly, the temperature dependence at 2 ps and 20 ps pump-probe delay results from a non-equilibrium situation where the electrons are "hot".
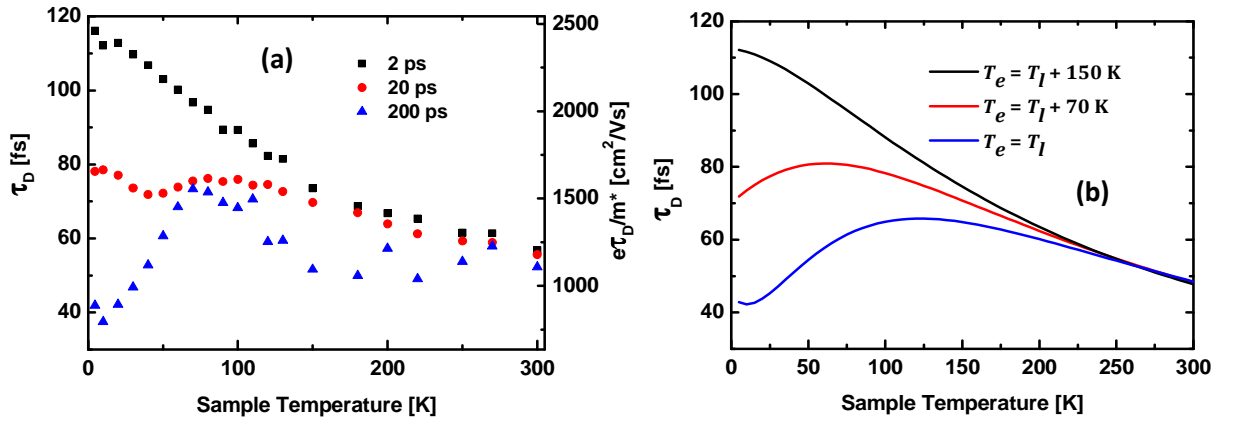
Figure 6-8 (a) Dependence of the relaxation time τ_D, and the estimated DC mobility on the sample temperature at different pump-probe delays. The concentration of photogenerated conduction band electrons is about $5.1\cdot10^{16}$ cm^{-3}, and a value of 0.083 m_e is used for m^*.[194] (b) Relaxation time τ_D, obtained from fitting (6.7) to mobility spectra calculated from (2.40) taking ionized impurity ($n_i = 4\cdot10^{17}$ cm^{-3}, $n = 5.1\cdot10^{16}$ cm^{-3}) and acoustic deformation potential scattering (D_{ac} = 36 eV) into account.

[IX] However, the interpretations differed. One study claimed that non polar optical phonon scattering is not important,[200] two others found it to be a major scattering mechanism.[204,211] It will turn out that the data in Figure 6-8 can neither be explained by nonpolar nor polar optical scattering.

It can be estimated that the heating of the phonons, due to the energetic relaxation of the electrons, can be neglected for lattice temperatures down to at least 30 K (cf. section 8.5). Hence, the lattice is characterized by the cryostat-controlled sample temperature. The "hot" electrons, however, are characterized by a non-equilibrium distribution function, which is assumed to be of Fermi-Dirac type $f(T_e, E_F)$ here with an electronic temperature $T_e \geq T_l$. So Figure 6-8 (a) shows how the MRT changes due to the cooling of hot electrons and the implications of this cooling are stronger for lower lattice temperature.

Figure 6-8 (b) demonstrates that the trend in Figure 6-8 (a) can be qualitatively reproduced with (2.40) when the MRTs (2.34) and (2.32) of charged impurity[X] and acoustic deformation potential scattering[XI] are taken into account, and when the electronic temperature is assumed to be 150 K and 70 K higher than the lattice temperature at pump probe delays of 2 and 20 ps, respectively.[XII] It is assumed that the sample is fully compensated, and any intrinsic charge carrier density is neglected with respect to the extrinsic carrier density.

It turns out that it is not possible to reproduce the hot electron mobility in Figure 6-8 (a) by predominant scattering with optical instead of acoustical phonons.[XIII] Regarding non-polar optical

---

[X]To evaluate the integral in eq. (2.40) for charged impurity scattering, the electron quasi-Fermi level E_F and the Thomas-Fermi screening wave vector $q_0 = (4\pi^2 / \epsilon \cdot \partial n / \partial E_F)^{1/2}$ must be known. This can be achieved by numerically calculating the charge carrier density as $n = \int D(E) f(E; E_F, T) dE$, using the effective mass density of states $D(E)$. The correct Fermi energy follows from the requirement that the experimental excitation density is reproduced. Once the Fermi energy is known, the calculation of the screening wave vector is straightforward.

[XI] Expression (2.32) for the acoustic deformation potential MRT is derived by simplifying the phonon occupation number as

$$\frac{1}{e^{\hbar\omega(\mathbf{q})/kT_l} - 1} \approx \frac{kT_l}{\hbar\omega(\mathbf{q})} - \frac{1}{2},$$

which relies on $\hbar\omega(\mathbf{q}) \ll kT_l$.[12] For hot phonons at very low lattice temperatures, this approximation becomes increasingly inexact. The maximal error in the above approximation occurs for $\mathbf{q} = 2\mathbf{k}_{max} \approx 2\sqrt{3m^* kT_e} / \hbar$, i.e. backscattering of the highest energy electrons. However, with the parameters used in Figure 6-8 (b), even the maximal error does not lead to a change of the simulated relaxation time by more than 1 %.

[XII] To simplify the calculation, the interaction of electron and holes is neglected. Also, the contribution of holes and recombination on the electric screening strength is not taken into account.

[XIII] The reason lies in the different dispersion relations: Acoustic phonons can have arbitrarily low energies, so that scattering can always occur, even for very low lattice temperatures or very low electron energies. Optical phonons however, always have a finite energy. So at low lattice temperatures the occupation numbers are exceedingly low, and carriers with energies less than the phonon energy cannot emit phonons at all. The characteristic optical phonon energy in CIS corresponds to kT at room temperature (Table 3), so in

phonons, this is plausible because the interaction strength is not known and, based on symmetry arguments, it was also proposed that this type of scattering does not occur for electrons in CIS at all.[203] In contrast, the scattering due to electron-polar optical phonon interaction (2.27) depends on known material parameters and would have a significant impact on the mobility at room temperature. However, a significant contribution from polar optical phonons to the total momentum relaxation rate would not only conflict with the hot electron mobility but would also predict a very rapid electron cooling (cf. section 6.4.3), which is not consistent with the tens of ps long dynamics in Figure 6-8 (a). The reason for this discrepancy may be that the conventional, analytic model (ref. 18–21) of the interaction of electrons and polar optical phonons is based on an unscreened interaction of carriers with the phonon induced polarization field, and that it has been derived for the particular case of a single longitudinal optical phonon branch. CIS however, has several longitudinal optical phonon branches.[192]

An acoustic deformation potential of $D_{ac} = 36$ eV, which is the result of simulating the experimental data, is in line with previous reports, which suggested acoustic deformation potentials between 7 eV[211] and 55 eV.[200] In transport studies on CIS, the overall mobility is usually determined by adding up the (inverse) mobilities of different scattering processes. As demonstrated in section 8.7, this can yield quantitatively different results compared to the (correct) application of Matthiessen's rule, where relaxation rates are added up and which is applied here. Hence, the comparison of numerical results is complicated. An alternative method to assess the deformation potential is to measure the temperature dependence of the band gap. Quintero et al. have measured this variation and decomposed it into the contribution from the thermal expansion of the lattice and the electron-phonon interaction.[191] By equating the latter contribution with the theoretical expression[241]

$$\left.\frac{\partial E_{gap}}{\partial T}\right|_{e-ph} \approx 0.175 \frac{k_B V}{\hbar^2 M c_{ac}}\left(m_e^* D_e^2 + m_h^* D_h^2\right),\tag{6.8}$$

and the former contribution with[191]

$$\left.\frac{\partial E_{gap}}{\partial T}\right|_{dil} = 2\alpha\left(D_e + D_h\right),\tag{6.9}$$

the conduction band deformation potential was calculated as -9.39 eV. Here, V and M are the volume of the primitive cell and the mass of the atoms therein, respectively, and c_{ac} is the velocity of sound. If the calculation of Quintero et al. is redone with more recent values for the band mass-

---

the liquid helium to liquid nitrogen temperature range, optical phonon scattering is inefficient even for hot electrons. Hence, in this region the mobility would be governed by impurity scattering, which fails to adequately describe the hot electron mobility (cf. Figure 8-5(b)).

es,[194] and if predominant coupling to longitudinal modes with a velocity of sound of 3770 m/s[190] instead of 2010 m/s is assumed, a value of $D_{ac} = |D_e| = 20.7$ eV is retrieved. This is close to the value of 36 eV obtained from simulating the momentum relaxation rate.

6.4.3 Cooling Dynamics

The dynamics of the MRT in Figure 6-8 (a), which are due to the thermalization of hot electrons with the lattice, are most obvious at the lowest sample temperature of 5 K. Figure 6-9 exhibits the fully resolved decay of the MRT at this temperature. Over about the first 100 ps, the relaxation rate τ_D decays from over 100 fs to roughly 30 fs and stays constant afterwards on a ns timescale. Since the time dependence of τ_D is implicitly a dependence on the transient electronic temperature, the latter can be determined by calculating cooling curves, simulating the relaxation rate based thereon, and comparing it to the measurement. The cooling curve is acquired as follows.

Electron cooling occurs through phonon emission. For thermalized carriers phonon absorption and emission balance each other, however, in case of hot carriers phonon emission dominates, and there is a net energy transfer to the lattice. The resulting energy loss rates for an electron with energy E due to acoustic phonon and polar optical phonon scattering are[13]

$$R_{ac}(E) = -\frac{D_{ac}^2 (2m^*)^{5/2}}{2\pi\rho\hbar^4} E^{3/2}$$

$$R_{opt}(E) = C_0 \frac{e^2 \omega_{op}^2 m^* (\epsilon(0) - \epsilon(\infty))}{2\pi\sqrt{2m^* E} \cdot \epsilon(0)\epsilon(\infty)} \left(\frac{\mathrm{asinh}\left(\sqrt{E/\hbar\omega_{op}}\right)}{e^{x_0} - 1} - \frac{e^{x_0} \cdot \mathrm{asinh}\left(\Re\left(\sqrt{E/\hbar\omega_{op} - 1}\right)\right)}{e^{x_0} - 1} \right). \tag{6.10}$$

Here, C_0 is a phenomenological attenuation parameter.[242] The total energy loss rate of an electron distribution that is defined by the density of states $D(E)$ and the Fermi-Dirac occupation probability $f(E; E_F, T_e)$ is

$$\frac{dE(T_e)}{dt} = \int_{E_{CBM}}^{\infty} R(E) f(E; E_F, T_e) D(E) dE, \tag{6.11}$$

with $R = R_{ac} + R_{opt}$. Since this loss rate implicitly depends on time via the electronic temperature $T_e(t)$, it holds

$$\frac{dE(T_e(t))}{dt} = \frac{dE(T_e(t))}{dT_e} \cdot \frac{dT_e}{dt}, \tag{6.12}$$

where the first factor on the rhs can be calculated as[XIV]

$$\frac{dE\left(T_e\right)}{dT_e} = \int\limits_{E_{CBM}}^{\infty} E \cdot D\left(E\right)\frac{df\left(E;E_F,T_e\right)}{dT_e}dE.$$ (6.13)

Hence, the transient electronic temperature $T_e\left(t\right)$ follows from integrating

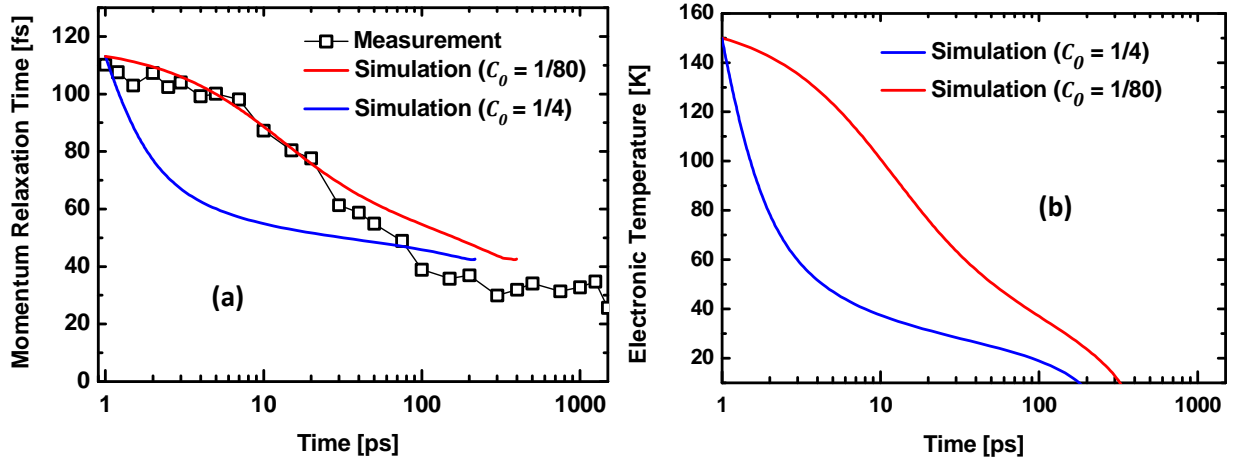$$\frac{dT_e}{dt} = \frac{dE}{dt}\bigg/\frac{dE}{dT_e}.$$ (6.14)

Figure 6-9 (a) Experimental and simulated time dependence of the momentum relaxation rate in Cu-rich CIS at a sample temperature of 5 K and a pump fluence of 0.019 I_0 (I_0 = 7.4·10^13/cm²). (b) The cooling curves that correspond to the simulation in (a).

Figure 6-9 (a) demonstrates that a cooling curve with a strong attenuation factor C_0 = 1/80 (depicted in Figure 6-9 (b)) allows for a reasonable reproduction of the measured transient MRT. Otherwise, the carrier cooling due to polar optical phonon emission leads to a rapid decay which disagrees with the observed trend. The simulation of the mobility in 6.4.2 has led to the conclusions that acoustical phonons are more limiting to charge transport than optical phonons, and that the 'text-book expression' for the interaction of electrons and polar optical phonons[12,14] is an overestimation for CIS. This conclusion is consistent with the finding that the text-book expression for R_{opt}[13,14] is also an overestimation.

[XIV] As usual, the temperature dependence of the Fermi level follows from the demand that $\int_{E_{CBM}}^{\infty} f\left(E;E_F\left(T_e\right),T_e\right)D\left(E\right)dE = n$, where n is the experimental excitation density.

6.4.4   Recombination Mechanism

Since the frequency dispersion of the photoconductivity in Cu-rich CuInSe$_2$ can be fit with the simple, analytical Drude model $\Delta\sigma = nq^2\tau_D / m^* \cdot (1 - i\omega\tau_D)^{-1}$, changes of $\Delta\sigma$ can be separated into changes of the transient excess charge carrier density $n(t)$ and the MRT τ_D. This separation is achieved by fitting the Drude formula to the photoconductivity for each pump-probe delay. At room temperature a change of τ_D does not yet play a role, so that the lifetime of photoconductivity and charge carriers is equal, but has to be taken into account for cryogenic temperatures (Figure 6-8 (a)).
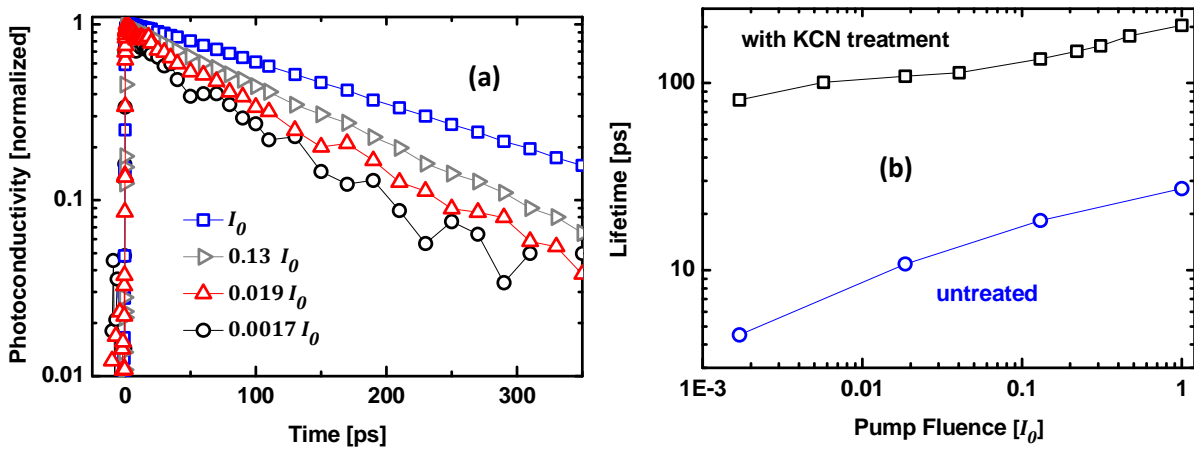

Figure 6-10 (a) Exponential photoconductivity decay curves in Cu-rich CIS (with KCN treatment) at room temperature (I$_0$ = 7.4·10^{13}/cm^2). (b) Dependence of the charge carrier lifetime on the excitation density at room temperature.

Figure 6-10 (a) exhibits photoconductivity transients of Cu-rich CIS for various pump intensities at room temperature. The photoconductivity decays exponentially, so that the excess charge carrier density can be described by a single lifetime, which increases from about 80 ps at low excitation to 200 ps at the high excitation,[XV] and which is in agreement with published charge carrier lifetimes in Cu-rich CIS.[180] An increase of the lifetime with the excitation density is symptomatic for stepwise recombination via intra-bandgap states, which constitute a bottleneck for the reaction. In contrast, radiative band-band and Auger recombination would be strongly amplified for high enough excitation densities. Without a KCN treatment, which removes copper selenides and oxides from the surface,[224,225] the lifetime shows a similar trend regarding the excitation density, however, it is reduced by roughly one order of magnitude compared to etched samples (Figure 6-10 (b)).

[XV] The lower limit of the excitation density is given by the requirement to execute a measurement in reasonable time, while the upper limit is given by the laser fluence.

The enhancement of the lifetime through the KCN treatment indicates that the shorter lifetime in the unetched CIS is limited by surface recombination due to the contamination with copper selenides and oxides. In contrast, the lifetime may be limited by bulk recombination when these contaminations are etched away. In a simplified picture, the decay rate of an excess charge carrier density n is often described with a capture cross section σ_{cap}:[243]

$$\frac{dn}{dt} = N_t \sigma_{cap} v \cdot n. \tag{6.15}$$

Here, N_t is the density of free recombination/trapping sites and v is the thermal carrier velocity. Taking the charged impurity density of $4 \cdot 10^{17} cm^{-3}$, which was used to simulate the ionized impurity scattering contribution to the mobility (Figure 6-8), as an order of magnitude estimate for N_t yields a capture cross section of $1.5 \cdot 10^{-15}$ cm^{-2} to reproduce an electron lifetime of 100 ps at room temperature. Since this capture cross section is of reasonable magnitude, it may indeed be possible that the surface recombination is negligible after the KCN treatment.
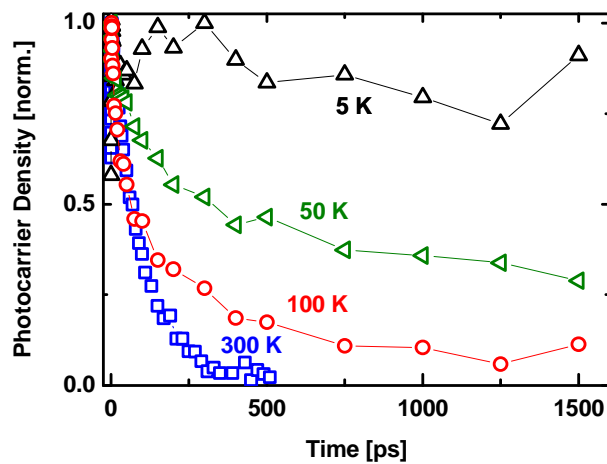

Figure 6-11 Transient excess carrier density in Cu-rich CIS for different sample temperatures at a constant pump fluence of 0.019 I_0 ($I_0 = 7.4 \cdot 10^{13}$/cm^2).

When the temperature is lowered, the recombination is decelerated and exhibits a progression that cannot be described by a single exponential decay anymore (Figure 6-11 (a)). If the electrons were captured into shallow (hydrogen-like) traps, the recombination kinetics should accelerate for decreasing temperature.[243] Hence, it is likely that the recombination proceeds through deep traps and involves multiple (optical) phonon emission (MPE), which is also indicated by the thermally activated recombination in Figure 6-11 (a): Since the electronic level of a defect depends on the nuclear positions of nearby lattice atoms, and different charge states of a defect generally go along with different configurations of these atoms,[244,245] thermal activation energy is

necessary to reach a nuclear configuration where electron capture can happen.[XVI] If the electronic levels of the neutral and the negatively charged defect cross at some energy above the conduction band minimum, higher energy electrons are preferably captured instead of those at the CBM, so the recombination can be affected by electron cooling. According to this model, the initial slow-down of the recombination at intermediate temperatures of 5 and 100 K can be explained with electron cooling. At 5 and 300 K this effect cannot be observed because at 300 K even the relaxed electron distribution can fully participate in recombination and at 5 K the ability of the defect to reach the crossing point is the major limitation.

6.4.5   Effect of Surface Roughness

As shown in Figure 6-12 (a), the measured mobility does not agree with the theoretically expected value of $e\tau_D / m^*$, as calculated from the fit parameter τ_D and the literature effective mass (Table 3), even if it is taken into account that the fit parameter τ_D slightly overestimates the MRT (Figure 8-4 (b)). Possible explanations for this discrepancy are that the density of states effective mass is higher than the reported value of 0.08-0.09 m_e,[194–198] so that the theoretical estimate is too high, or that the experimental value is too low. The former possibility appears unlikely because several independent studies report the same value. So which artifact could influence the experimental mobility? The determination of the mobility by (3.1) is tailored to the situation of a homogenous flat thin film. However, Figure 6-4 shows that the films have a natural surface roughness. So to some extent the photoconductivity of the surface region, which is a mixture of CuInSe$_2$ and air/vacuum, is measured instead of the CIS bulk photoconductivity.

To simulate the consequences of the surface roughness, the Bruggemann EMA can be applied. The effective permittivity $\langle\epsilon\rangle$ of a medium consisting of randomly dispersed spheres of two different materials with permittivities ϵ_1 and ϵ_2 (CIS and voids) is determined through[101]

$$f\frac{\epsilon_1 - \langle\epsilon\rangle}{\epsilon_1 + 2\langle\epsilon\rangle} + (1-f)\frac{\epsilon_2 - \langle\epsilon\rangle}{\epsilon_2 + 2\langle\epsilon\rangle} = 0,$$ (6.16)

where f denotes the volume fill fraction of the material with permittivity ϵ_1. The effective photoconductivity can now be calculated analogously to the procedure in section 4.4.2. For a about equal shares of CuInSe$_2$ and vacuum, the effective photoconductivity exhibits almost the same

---

[XVI] This recombination model (ref. 244,245) can be understood in the Born-Oppenheimer approximation, which states that the defects electronic level depends parametrically on the configuration of the atom cores in the immediate vicinity. If the electronic ground state of the defect is in the band gap, the defect can only capture an electron when the cores around the defect reach a configuration (by thermal fluctuation) where the defects electronic level crosses the conduction band minimum. After electron capture, the electronic ground state of the defect is generally at a different nuclear configuration. The rapid relaxation of the local lattice atoms to this new configuration leads to the emission of lattice phonons.

spectral shape as the CIS photoconductivity, but is about three times smaller (Figure 6-12 (b)). This explains qualitatively how a rough surface can lead to a reduction of the measured photo-conductivity in OPTP experiments.
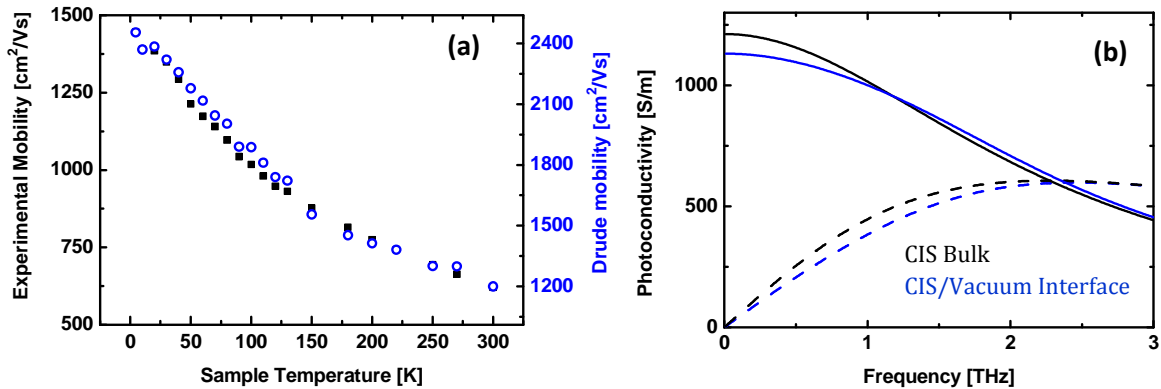

Figure 6-12 (a) Comparison of the measured DC mobility (extrapolating (3.4) to 0 THz) and the theoretical value calculated from the fit parameter τ_D as $e\,\tau_D\,/\,m^*$ (Table 3). (b) Typical CIS photoconductivity (calculated from (2.7) with $n = 5.1{\cdot}10^{22}$ cm^{-3}, $\tau_D = 70$ fs, and $m^* = 0.083\ m_e$) compared to the effective photoconductivity of a CIS/voids mixture ($f_{CIS} = 0.54$), scaled up by 3. Solid/broken lines denote the real/imaginary part.

6.4.6   Grain Boundaries

Grain boundaries are generally an important factor for charge transport in polycrystalline materials. The properties of grain boundaries in CIS are an active field of research. What makes grain boundaries especially interesting in CIS is their potentially beneficial role for cell efficiencies: polycrystalline CIS outperforms single crystalline cells.[208],[XVII] The interface region between neighboring crystallites with different orientations exhibits a complex structure with many dislocated atoms. This disordered structure can lead to defect states, which may act as recombination centers,[116] and if charged defect can lead to potential energy barriers,[247] which inhibit charge transport. A mechanism that is can lead to a benign influence of grain boundaries is an offset of the valence band, which repels holes but not electrons and so reduces the recombination.[208]

Potential barriers at grain boundaries obstruct the intergrain transport. Clearly, this particularly affects the DC mobility which is determined by the ability of electrons to undergo long range transport. However, backscattering at grain boundaries can also lower the mobility at THz frequencies, and can even lead to disturbances of the mobility spectrum that are indicative of carrier

[XVII] It has been proposed that impurities segregate to grain boundaries rendering the interior of CIS grains purer than a comparable single crystal with an even distribution of defects.[246]

localization.[110] The maximum consequence of this effect can be clarified by regarding perfectly reflecting grain boundaries, i.e. a backscattering probability of 1. A typical room temperature mean free path in CIS can be estimated at 25 nm. The grain size in copper rich CIS is on the order of 500 nm, which yields a value of -0.5 for the backscattering parameter of the Drude-Smith model with (4.18). This would have a large effect of the mobility, so that it does not resemble the Drude spectrum any more (Figure 6-13). Hence, the grain boundaries in CIS have to be permeable – at least to some extent.
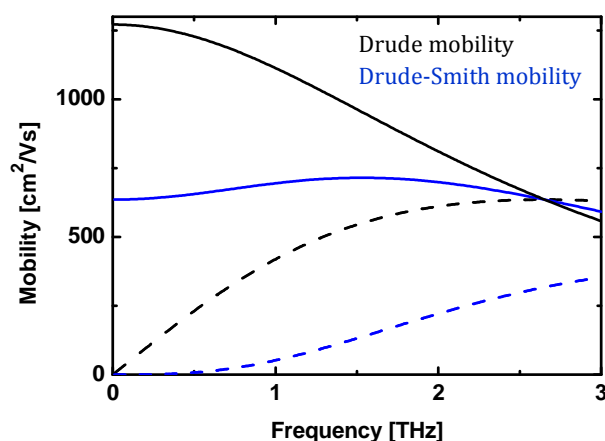

Figure 6-13 Comparison of Drude mobility (τ_D = 60 fs, $m^* = 0.083\,m_e$) and Drude-Smith mobility (τ_D = 60 fs, $m^* = 0.083\,m_e$, c_1 = -0.5). Solid/broken lines denote the real/imaginary part.

6.5 Solar Cell Grade CuInSe$_2$

In this section, the transport and recombination in CIS with a solar cell grade composition is examined. Since PL is an often used characterization technique for CIGS absorbers (and devices), its appliance here is used to verify the comparability of the Cu-poor samples. Thereafter, OPTP measurements uncover how the carrier transport and the recombination are affected by the off-stoichiometry. The transport is discussed in light of the potential fluctuation model, and from the impact of the composition on the charge carrier lifetime the Cu$_{In}$ antisites is identified as the dominating recombination center. Since the presence of sodium did not lead to any discernable alteration of $\Delta\sigma(\omega,\tau)$,[XVIII] this section does not generally discriminate between CIS grown with or without a NaF precursor layer.

[XVIII] The only effect of sodium that can be observed is that the photoluminescence amplitude and lifetime decays when sodium containing samples are illuminated under ambient conditions.

6.5.1   Photoluminescence

Figure 6-14 (a) exhibits intensity dependent low temperature PL spectra of Cu-poor CIS.[XIX] At ND3, two PL bands at 0.836 eV and 0.917 eV can be distinguished. At higher fluence, the low energy band cannot be clearly discriminated from the tail of the high energy band. Increasing the pump intensity leads to a blue shift of the PL bands by 12 meV per decade of excitation power, which is about an order of magnitude more than in Cu-rich CIS. The temperature-dependent variation of the PL at constant pump intensity is depicted in Figure 6-14 (b). Raising the temperature from 17 K to room temperature first leads to a red shift and a loss in PL intensity by several orders of magnitude. Then a new band around 0.99 eV band appears, which shifts blue. At room temperature, the PL spectrum exhibits at least three transition bands whose position is insensitive to the pump intensity.
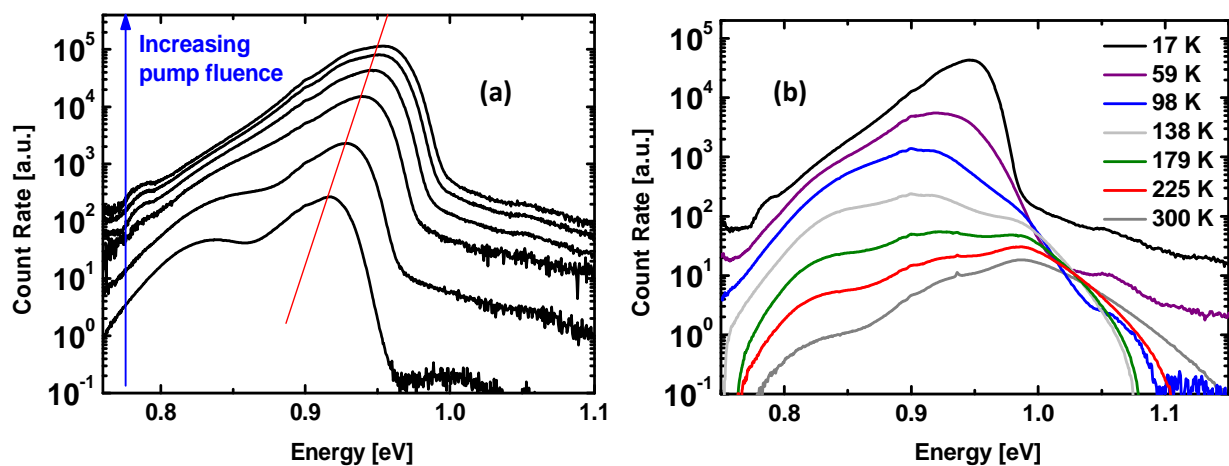

Figure 6-14: (a) PL spectra of Cu-poor CIS at a sample temperature of 17 K for different pump intensities. The bottom/top curve corresponds to ND3/ND0. The red line points out the blue shift of the PL with increasing pump intensity. (b) Temperature dependent PL spectra of Cu-poor CIS at ND0.5.

The PL of Cu-poor CIS can be explained with the potential fluctuation model (section 6.2.3).[169] At low temperature and low intensity, the carriers populate the deepest potential wells. When the intensity is increased, the PL bands shift to higher energies because of the filling of deep wells and the reduction of the fluctuation amplitude due to more efficient screening. In contrast to DAP and free to bound transitions, this shift can be on the order of 10 meV per decade of excitation density.[169] The temperature-dependent shift of the PL in Figure 6-14 (b) can also be explained with potential fluctuations. Charge carriers in the upper states of the potential wells need less thermal energy to hop and are therefore more mobile than states at the bottom of the wells. Therefore, they have a higher probability of finding a non-radiative recombination center. The

---

[XIX] The experimental situation is identical to that described in section 6.4.

radiative recombination of the low energy carriers remaining in the wells causes the red shift of the PL spectrum. If the temperature is elevated high enough, the charge carriers can be excited into band-like states. The band-impurity (and band-band) recombination shifts blue with increasing temperature because of the kinetic energy of the carriers.

6.5.2   Transport in a Fluctuating Potential

Figure 6-15 shows the dramatic effect of the composition on the mobility: In contrast to stoichiometric CIS, the mobility in Cu-poor CIS lacks any resemblance to the Drude theory. The real part of the mobility has an ascending slope, which is reminiscent of the THz mobility in amorphous semiconductors[248,249] and which is generally regarded as a sign of carrier localization. Also, the absolute value of the mobility is much smaller than in stoichiometric CIS, especially at low frequencies. Already at 0.7 THz, the 150 cm^2/Vs in Cu-poor CIS are about a factor of 4 lower compared to stoichiometric CIS. The presence of sodium, which has a beneficial impact on CIS solar cells, does not lead to any discernable alteration of the mobility spectrum. Since the Cu-poor samples with and without sodium differ largely in grain size (Figure 6-4), the latter is clearly no limitation for the THz mobility in Cu-poor CIS. Hence, the reason for the inferior charge transport in Cu-poor CIS lies in the bulk properties of the crystallites. The question arises whether this can be attributed to the potential fluctuations for whose existence the PL gives strong evidence.
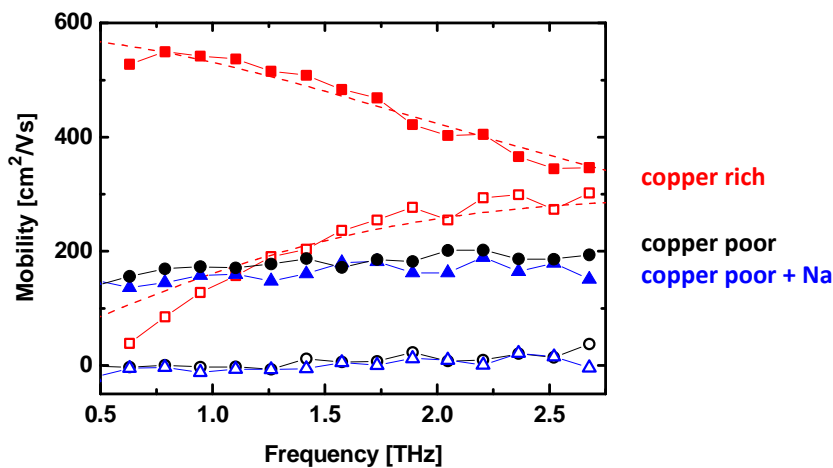
Figure 6-15 Comparison of the room temperature mobility of stoichiometric and Cu-poor CIS at a pump-probe delay of 3 ps and a pump fluence of about $3 \cdot 10^{12}$/cm^2. Dashed lines are Drude fits. Filled/open symbols denote the real/imaginary.

The mobility of a material with a spatially fluctuating potential may be of non-Drude type due to two mechanisms. First, the carriers accumulate in the deepest wells (at least at low temperatures), and charge carriers that are spatially confinement exhibit a mobility spectrum that is of non-Drude type.[110] Second, in the presence of potential fluctuations effective medium effects play

a role because the material consists of conductive carrier droplets (in the wells) which are isolated from each other by non-conducting regions. This is similar to photoexcited semiconductor nanocrystals, and it is well known that a blend of conducting and non-conducting materials can result in an effective conductivity that peaks at non-zero frequencies.[10] The impact of both effects on the mobility can be expected to decrease with increasing temperature and excitation density due to thermal excitation out of the wells respectively screening and filling of the fluctuations.

Figure 6-16 (a) demonstrates the influence of temperature and pump intensity on the mobility in Cu-poor CIS.[XX] Compared to the room temperature spectrum, the real part of the mobility has a steeper slope at a sample temperature of 100 K, rising by more than 300 % between 0.5 THz and 2.5 THz. Also, the imaginary part of the mobility becomes decidedly negative. So roughly speaking, the fingerprint of localization is increased[10] when the temperature is lowered at a constant, low excitation density (about $2 \cdot 10^{16}$ cm^{-3}). However, by increasing the excitation density[XXI] at low temperature this fingerprint can be diminished and the frequency dispersion of the mobility is similar to that at room temperature, except for an increase in amplitude.
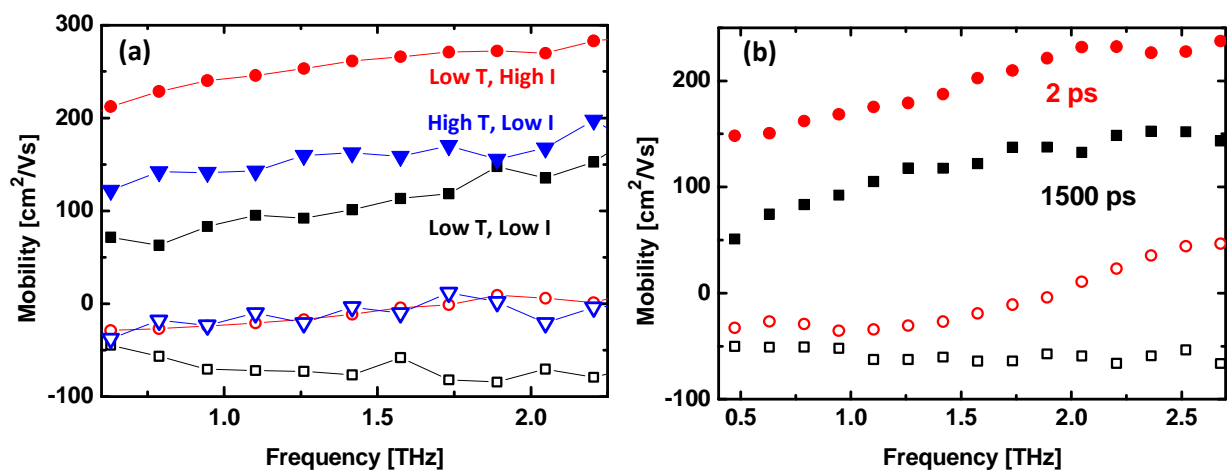
Figure 6-16 (a) Variation of the mobility with pump intensity and temperature in Cu-poor CIS. Low/high Temperature and low/high intensity correspond to 100/300 K and $3.6 \cdot 10^{11}/2.9 \cdot 10^{13}$ cm^{-2}, respectively. Filled/open symbols denote the real/imaginary part. (b) Comparison of the mobility at 2 ps with the relaxed mobility at 1.5 ns at 100K and a pump fluence of $2.4 \cdot 10^{12}$ cm^{-2}.

[XX] The mobility for Cu-poor CIS is estimated by neglecting a possible change of the charge carrier population for all pump-probe delays. This seems reasonable considering the long-lasting photoconductivity of at least several ns (cf. section 6.5.3).

[XXI] Strictly, the charge carrier density cannot be varied independently from the temperature because the pump laser heats the sample.

From the analysis of the transient photoconductivity in Cu-rich CIS it is known that the carriers need at least several tens of ps to cool to the lattice temperature (section 6.4.2-3). Figure 6-16 (b) demonstrates that the time dependent relaxation of the electronic temperature affects the mobility: The transport of hot electrons is less impeded than that of equilibrated ones.

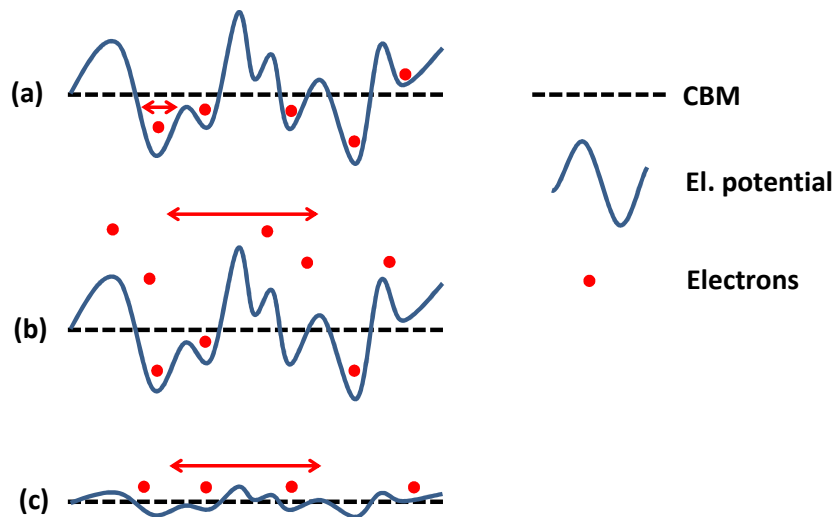Figure 6-17 Scheme of the effect of potential fluctuations on charge transport under different conditions. The vertical arrows illustrate the ability of the electrons to move. (a) Low temperature and excitation density. (b) High temperature. (c) High excitation density.

Figure 6-17 points out how the temperature, time, and intensity dependence of the mobility can be qualitatively understood with the model of a spatially fluctuating electric potential. At low temperature and low excitation density, electrons gather in the deepest potential wells (part (a)). Excitation above the barriers is unlikely and transport is limited by interbarrier tunneling. At higher temperature an increasing amount of carriers can be excited thermally above the barriers, which are then characterized by a more free charge carrier like mobility (part (b)). Raising the excitation density leads to stronger electronic screening, which reduces the amplitudes and spatial extensions of the fluctuations (part (c)) promoting better electron transport and also a more free charge carrier like mobility. Though an increase in temperature or excitation density reduces the detrimental influence of the fluctuations on the charge carrier mobility, a free carrier like mobility is not recovered. In fact, even at room temperature a positive slope of $\mu(\omega)$ can be observed up to the highest achieved electron-hole pair concentration of about $2 \cdot 10^{18}/cm^3$. One may therefore ask if there are conditions at all under which the fluctuations are not a limiting factor anymore. This is likely not the case because the material is still inhomogeneous when the fluctuations are completely screened. The reason lies in the electron density, which has to be inhomogeneous in order to screen a randomly fluctuating potential. However, the derivation of a Drude-like mo-

bility (cf. section 2.2.3) is based on a homogenous distribution function and thus not valid in non-stoichiometric CIS.

6.5.3   Recombination Mechanism

Figure 6-18 (a) exhibits the transient photoconductivity of Cu-poor CIS for injection levels differing by 3 orders of magnitude at room temperature. The dynamics is distinctively different from the mono-exponential decay in Cu-rich CIS: In just a few ps the photoconductivity rapidly decays from the initial maximum amplitude $\Delta\sigma_{max}$ by an amount of $\Delta\sigma_{ps}$ and then sustains over many ns. The relative amplitude of the initial decay $\Delta\sigma_{ps}$ increases for lower excitation density and sample temperature down to about 80 K (Figure 6-18 (b) and (c)), and it can be quenched if the excitation density is high enough. The lifetime of the photoconductivity that follows the initial relaxation cannot be determined reliably, as it is much longer than the accessible time window of 1.5 ns, which is a huge difference compared to the stoichiometric material. For the highest achievable pump intensity, the slow decay component leads to a loss of about 10 % over 1.5 ns, which correspond to a decay time constant of 11 ns. However, if the excitation density is not that high, no further decay can be ascertained at all over 1.5 ns. Below about 50 K, the charge carrier lifetime even starts to exceed the pump pulse separation of 6.7 µs (Figure 6-18 (c)).[XXII] This indicates, that the recombination mechanism in Cu-poor CIS is thermally activated as that in Cu-rich CIS.

Lowering the temperature does not lead to any qualitative changes of the photoconductivity transients, but the amplitude of the initial decay does not increase below about 80 K, instead further cooling leads to a decrease. At about the same temperature, the charge carrier lifetime starts to exceed the time separation of consecutive pump pulses. Hence, it seems reasonable to assign the trend reversal to an accumulation of charge carrier density, which effectively has the same effect as increasing the pump intensity: damping the initial fast decay (Figure 6-18 (a)).

[XXII] The maximum delay that can be realized with the delay stages in the OPTP setup for a pump and a probe pulse that stem from the same fundamental 800 nm laser pulse is about 1.5 ns. However, since the sample is excited periodically at a rate of 150 kHz, a negative pump-probe delay corresponds to a temporal difference of 6.7 µs to the preceding pump pulse.
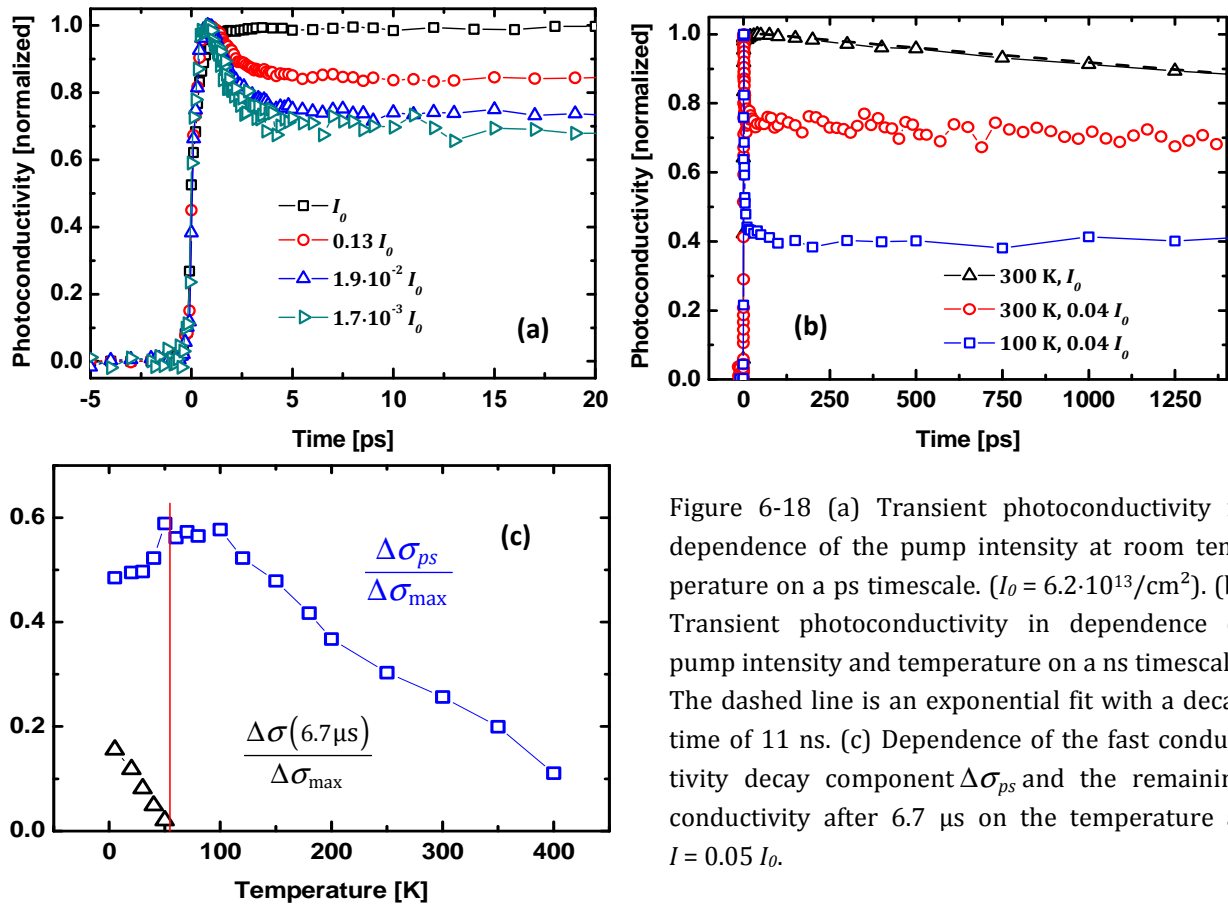
Figure 6-18 (a) Transient photoconductivity in dependence of the pump intensity at room temperature on a ps timescale. ($I_0 = 6.2 \cdot 10^{13}/cm^2$). (b) Transient photoconductivity in dependence of pump intensity and temperature on a ns timescale. The dashed line is an exponential fit with a decay time of 11 ns. (c) Dependence of the fast conductivity decay component $\Delta\sigma_{ps}$ and the remaining conductivity after 6.7 μs on the temperature at $I = 0.05\,I_0$.

Owing to the lack of a model that allows separating mobility and charge carrier density changes for Cu-poor CIS, it is not readily clear what the origin of the fast decay component is. In light of the effect of potential fluctuations on hot and relaxed electron transport (Figure 6-16 (b)), the rapid decay of the photoconductivity is attributed to a decrease of the mobility due to carrier cooling rather than recombination here. Hot electrons are just not impeded as much by the fluctuations as equilibrated ones. Hence, in comparison to the stoichiometric material the actual recombination rate is reduced by orders of magnitude in solar grade Cu-poor CIS. One reason for the tremendous lifetime enhancement may be a spatial separation of electrons and holes on a nanoscopic scale due to fluctuating electric potential. This idea is supported by the observation that increasing the pump intensity, and thus the screening of the fluctuations, reduces the photoconductivity lifetime.[XXIII] However, this effect cannot be the sole reason for the lifetime enhancement, because under high excitation conditions, where the missing initial relaxation indicates that the fluctuations are completely screened (Figure 6-18 (a)), the lifetime is still orders of magnitude higher than in Cu-rich CIS. Hence, the huge lifetime difference between Cu-rich and Cu-poor CIS

[XXIII] Unless this very small decay, if observable at all, is not caused by another mechanism such as charge carrier diffusion.

must (partly) be assigned to a different effectiveness of non-radiative recombination. In light of the compositional difference, the most straightforward explanation is that most of the recombination proceeds through an intrinsic defect that is more abundant in Cu-rich material. By intuition, one would suspect that for instance the abundance of Cu_{In} antisites correlates with the supply of copper during growth, and recent calculations show that the formation energy of Cu_{In} is considerably lower under Cu-rich than Cu-rich conditions.[187] The Cu_{In} defect can exist in differently charged states, and the formation energy of defects depends on their charge state. For defects that take up electrons from the host material, the formation energy decreases with increasing electron (quasi-) Fermi level.[250] In case of the Cu_{In} antisite, the (quasi-) Fermi level above which Cu_{In}^{2-} becomes thermodynamically more stable than Cu_{In}^{-1} is about 400 meV below the CBM.[187] Under illumination, this quasi-Fermi level can be easily reached, so that Cu_{In} can start to act as an electron trap. Hence, the Cu_{In} antisite is tentatively proposed to be the most important recombination center in CIS, leading to detrimental, short carrier lifetimes when CIS is not grown with a Cu-poor composition.

6.6 Conclusions

OPTP spectroscopy was employed to reveal the impact of stoichiometry deviations in $CuInSe_2$ on transport and recombination properties. The mobility in stoichiometric CIS thin films obeys to the Drude model, which enables the retrieval and detailed modeling of the MRT. From the temperature and time dependence of the MRT it can be deduced that the mobility is limited by acoustic deformation potential and charged impurity scattering, but grain boundaries are not observed to play a limiting role at THz frequencies. The cooling dynamics of hot photo-electrons is manifested in the change of the MRT after the excitation. By comparison with simulated cooling curves, it can be concluded that the charge carrier scattering with optical phonons is relatively weak. In Cu-poor CIS, the mobility is also limited by the bulk properties of the grains, however, in stark contrast to stoichiometric CIS, it is significantly lower in amplitude and its spectral form is not compatible with free electrons. These detrimental effects are ascribed to a spatially fluctuating electrostatic potential, which results from the abundance of charged defects, and which impedes charge transport. This model can qualitatively explain the influence of excitation density and temperature on the mobility, where an increase in both quantities results in a more Drude-like mobility.

While the transport properties are more favorable in Cu-rich CIS, the charge carrier lifetimes are much better in Cu-poor CIS, being orders of magnitude higher than the about 100 ps in Cu-rich CIS at room temperature. The recombination in stoichiometric CIS can be slowed down by increasing the excitation fluence or lowering the temperature, which is indicative of recombination through a deep defect involving a thermally activated rearrangement of the lattice at the defect

site. If the dominant recombination center in CIS is identified with the Cu_{In} antisite, the long lifetimes under copper poor conditions can be explained by a correlation of the Cu_{In} density with the abundance of Cu during growth. This is corroborated by recent theoretical results, which state that Cu_{In}^{-2} becomes thermodynamically favorable compared to $CuIn^{-1}$ if the electron (quasi-) Fermi level does not lie more than 400 meV below the CBM, which can easily be achieved under illumination. In addition, the electron lifetime in Cu-poor CIS may be enhancement by a spatial electron-hole separation due to the potential fluctuations.

7 **Summary**

In the present thesis, charge carrier dynamics was investigated in the light harvesting unit of three different thin film solar cell materials: radial hetero-junctions, dye-sensitized solar cells, and microcrystalline $CuInSe_2$ thin films. Fundamental questions regarding the charge transport in the absorber, the charge separation at the absorber/emitter interface as well as the relaxation of photo-excited charge carriers due to recombination and energy dissipation were addressed. For this purpose, an OPTP spectrometer was assembled that allowed pump-probe experiments with pump wavelengths of 400, 500 – 600 and 800 nm, and probe frequencies of 0.5 – 2.5 THz ($\sim$ 2-10 meV).

The new concept of radial hetero-junction solar cells is based on an innovative design which enables the usage of (potentially) low-cost and abundant absorber materials by drastically reducing the absorber thickness. High optical absorption is maintained due to the nano-structured, folded electrode geometry. In this thesis, the charge separation at the absorber/electrode interface following photo-excitation is examined on a model system that had previously shown relatively high conversion efficiencies.[4] It consists of wet-chemically prepared ZnO-electrode/In_2S_3-absorber core/shell nanorods. It was found that charge carriers photo-generated in In_2S_3 are rapidly captured into shallow traps within a few ps. However, it turned out that the charge carriers were preferably reemitted into the band instead of recombining with a hole. An analytical model, based on multiple trapping, yielded a quantitative description of the dynamics and suggested a very high trap density on the order of 10^{19} cm^{-3}, which is in line with the doctrine of allowing the use of mediocre quality materials. To understand the transient photoconductivity of the core/shell systems, which exhibited a complex dependence on the In_2S_3 shell thickness, the conventional Bruggemann effective medium approach was extended to take the correlation of the core and the shell into account. This approach allowed describing the dynamics in the core/shell systems as consisting of a fast ps trapping in the absorber and a subsequent hundreds of ps long dispersive transport towards the ZnO shell. It also allowed determining the relation of shell thickness and injection yield, which dropped for thicker shells. Hence, wet-chemical preparation, which introduces significant amounts of chemical impurities, and the nanograin structure of the absorber, which favors structural defects, pose a problem despite the idea that the requirements on the absorber quality can be relaxed.

In the field of dye solar cells, the combination of a nano-crystalline TiO_2 electrode and a metal-organic dye has yielded the highest efficiencies so far.[251] However, other semiconductor materials and morphologies, such as ZnO nanorods, are being explored that offer a potentially better charge transport through the electrode. Heterogeneous electron transfer (HET) from photo-excited dyes

into ZnO was observed in this thesis to proceed in a (until now) unique manner which deviated significantly from other electrode materials: The decay of excited dyes and the generation of free electrons exhibited different dynamics. Here, the HET from model dyes into ZnO was examined. The model dyes were based on a perylene chromophore, a carboxylic acid anchor, and systematically prolonged conjugated bridge units. Transient absorption (TA) revealed that the cationic versions of the dye molecules are formed within about 200 fs after photo-excitation, without any sign of exciplex formation was. The bridge length had insignificant influence on the electron transfer time, which can be explained by the formation of an intramolecular charge transfer from the chromophore onto the bridge following photoexcitation. This notion is supported by the molecular LUMOs, which extend onto the bridge and the anchor. OPTP showed that the mobile ZnO states are populated on a significantly longer time scale of 2-10 ps, and 2PPE spectroscopy indicated that the injected electrons were spatially and energetically localized at the ZnO/dye interface before moving into final ZnO bulk acceptor states. Interestingly, the free electron generation rate decreased with increasing bridge length, which is contrary to a previously published model[48] as the bridge length also increases the spatial electron-cation separation. Furthermore, it was found that the intra-rod mobility is not influenced by positively charged molecules at the surface. These results indicated that the Coulomb attraction of the cation did not impede the transferred electron from escaping into the bulk, as suggested by the above mentioned model[48]. Also, the transition to bulk states is not thermally activated, which would be expected if the electrons were trapped in a potential well. It is concluded that the most adequate explanation of the retarded free electron formation is an injection process from the dye into adsorbate induced interface states that are created because the interaction of dye and electrode poses a strong perturbation to the subsystems. Hence, contrary to current assumptions, instead of the ZnO bulk properties (permittivity, density of states) rather the ZnO/molecule interface properties play the key role in HET.

$Cu(In,Ga)Se_2$ solar cells yield high energy conversion efficiencies and are already being mass produced. Despite this technological advancement, the understanding of the transport and recombination properties is by far not complete. Here, for the first time OPTP spectroscopy was used to examine transport and recombination properties, investigating the effects of the nonstoichiometric Cu-poor composition of solar cell grade $CuInSe_2$. While stoichiometric $CuInSe_2$ thin films exhibited free electron Drude-like conduction, charge transport in Cu-poor $CuInSe_2$ showed signs of carrier localization. For the former material a MRT could be determined, which allowed concluding that charged impurity and acoustic deformation potential scattering are the limitations of charge transport. Furthermore, it was concluded that the cooling of hot electrons proceeds over several tens of picoseconds. For Cu-poor $CuInSe_2$, the mobility spectra could be explained by potential fluctuations created by the abundant and charged defects and the high degree of compensation. The potential fluctuations caused charge carrier localization and limited the charge transport, but could be overcome by screening or thermal activation induced by pump intensity and sample temperature variations. The recombination was found to be saturable and thermally

activated. Hence, it proceeds by electron and hole capture into a defect level. The charge carrier lifetime in stoichiometric $CuInSe_2$ is about 100 ps and therefore orders of magnitude lower than in Cu-poor $CuInSe_2$. This important difference in lifetimes was connected to the Cu_{In} antisite defect. As it may capture electrons[187] and is likely to be less abundant under Cu-poor growth conditions, this defect is proposed to be the reason for the short lifetimes in stoichiometric $CuInSe_2$.

8 Appendices

8.1 Symbols and Abbrevations

2PPE	Two Photon Photoemission
α	Absorption coefficient
AM1.5	Air Mass 1.5
CBM	Conduction Band Minimum
CIGS	$Cu(In,Ga)(Se,S)_2$
CIS	$CuInSe_2$
c_1	'backscattering factor' of the Drude-Smith model
DAP	Donor-Acceptor Pair
DFT	Density Functional Theory
DOS	Density of States
D(S)SC	Dye (Sensitized) Solar Cell
ϵ	Permittivity
ε	Energy
E_F	Fermi energy, chemical potential
ϵ_r	relative permittivity
EMA	Effective Medium Approach
eq(s).	Equation(s)
ETA	Extremely Thin Absorber
f_0	Fermi-Dirac distribution function
FBZ	First Brillouin Zone
HDPE	High-Density Polyethylene
HET	Heterogeneous Electron Transfer
HOMO	Highest Occupied Molecular Orbital
HZB	Helmholtz Zentrum Berlin
ILGAR	Ion Layer Gas Reaction
IR	Infrared
LEED	low energy electron diffraction
lhs	Left hand side
LUMO	Lowest Unoccupied Molecular Orbital
m^*	Effective mass
μ_r	Relative permeability
MPE	Multiple Phonon Emission
MRT	Momentum Relaxation Time
MT	Multiple Trapping
n, n_{eh}	Charge carrier density
NA	Non Adiabatic
ND	Neutral Density

NIR	Near Infrared
NOPA	Non-Collinear Optical Parametric Amplifier
OPTP	Optical-Pump Terahertz-Probe
PPC	Persistent Photoconductivity
PV	Photovoltaics
q_0	Thomas-Fermi wave vector
R	Reflectivity
Ref.	Reference
rhs	Right hand side
RTA	Relaxation Time Approximation
SEM	Scanning Electron Microscopy
SHG	Second Harmonic Generation
SNR	Signal to Noise Ratio
SSSC	Semiconductor Sensitized Solar Cell
τ	scattering time, momentum relaxation time
T	Transmission
TDFT	Time Dependent Density Functional Theory
TEM	Transmission Electron Microscopy
TRPL	Time Resolved Photoluminescence
TRMC	Transient Microwave Conductivity
UPS	Ultraviolet Photoemission Spectroscopy
VBM	Valence Band Maximum
WLC	Wight Light Continuum
XRF	X-Ray Fluorescence

8.2 Thin Film Formula

To derive the transmittance and reflectance of a thin film on a substrate the multiple reflections at each interface have to be taken into account (Figure 8-1). The reflectance and transmittance at the interfaces with the thin film can be treated coherently[I] using well-known thin film formulas. If light travelling through a medium i hits a thin film nested between medium i and a medium j, the transmission and reflection can be described using[252]

$$T_{ij} = \left| \frac{t_{i2}t_{2j}e^{i\beta}}{1 + r_{i2}r_{2j}e^{i\beta}} \right|^2 \text{ and } R_{ij} = \left| \frac{r_{i2} + r_{2j}e^{i2\beta}}{1 + r_{i2}r_{2j}e^{i2\beta}} \right|^2,$$ (8.1)

with the abbreviations (Fresnel coefficients)

$$r_{ij} = \left| \frac{n_i - n_j}{n_i + n_j} \right|^2 \text{ and } t_{ij} = \left| \frac{2n_i}{n_i + n_j} \right|^2.$$ (8.2)

[I] This means that the field amplitudes of the directly transmitted or reflected light and all the subsequent multiple reflections can be superimposed.

T_{ij} and R_{ij} have the following meaning: Let $E_i(\omega)$ be the field amplitude of the incident light and let E_t and E_r denote the field amplitude of the transmitted and reflected light. Then $|E_t \, / \, E_i|^2 = T_{ij}$ and $|E_r \, / \, E_i|^2 = R_{ij}$, whereas the intensity transmittance and reflectance are given as $|n_j \, / \, n_i|\, T_{ij}$ and R_{ij}, respectively.[252]
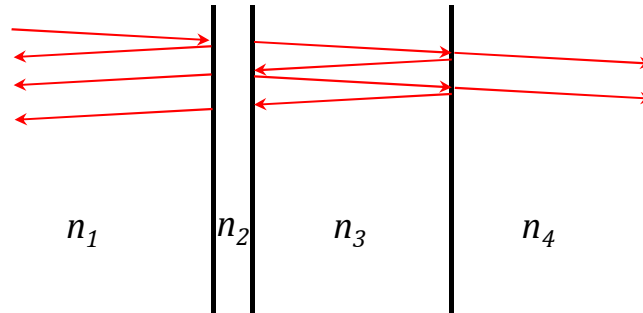

Figure 8-1 Scheme of the multiple reflections that have to be taken into account to derive the reflectance and transmittance of a thin film on a substrate. The thin film and the substrate are described by reflective indices n_2 and n_3, respectively. The media that enclose the film (air for the measurements in this thesis) have refractive indices of n_1 and n_4, respectively.

The passage of the light through the (thick) substrate cannot be treated by superimposing the field amplitudes of each reflection coherently. Instead, the intensity of each of the multiple reflections has to be summed up using of the Fresnel coefficients for the 3/4 interface and of (8.1) for the interface with the thin film. Doing so results in a geometrical series that finally yields

$$T_t = \left|\frac{n_4}{n_1}\right| \frac{T_{13}t_{34}}{1 - r_{34}R_{31}} \quad \text{and} \quad R_t = R_{13} + \frac{T_{13}r_{34}T_{31}}{1 - R_{31}r_{34}}. \tag{8.3}$$

8.3 ZnO Single Crystal Surface

An XPS overview spectrum of a sputtered and annealed ZnO single crystal $(10\bar{1}0)$ surface is shown in Figure 8-2 (a). The spectrum is essentially identical to the XPS spectrum of the ZnO nanorods in Figure 5-7 (b). A slight carbon peak can still be detected after the cleaning procedure Figure 8-2 (b) but since it is much smaller than the C1s peak of uncleaned ZnO$(10\bar{1}0)$ the cleaning procedure is rather effective.
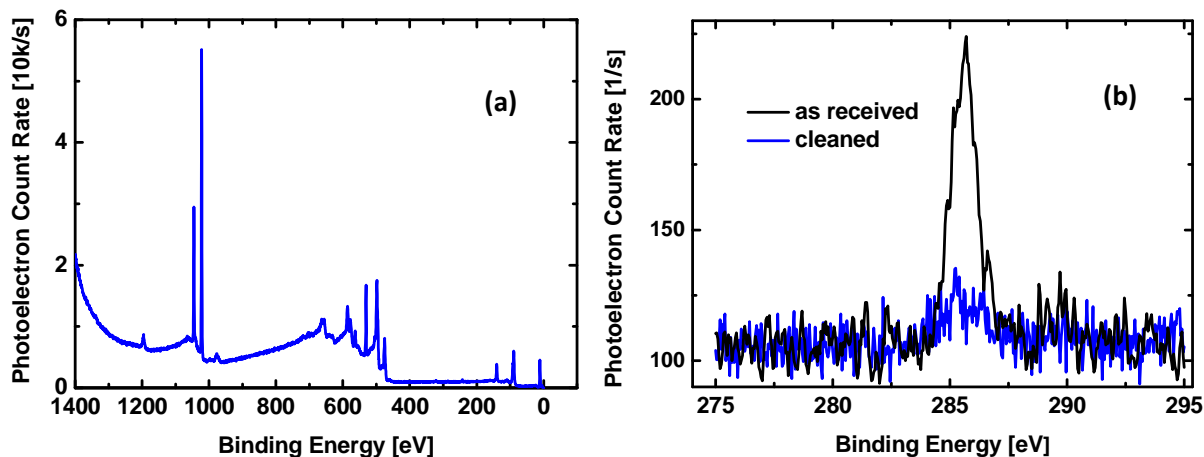
Figure 8-2 (a) XPS overview spectrum of a ZnO single crystal $(10\bar{1}0)$ surface that was cleaned by the routine described in section 5.2. (b) XPS spectrum in the region of the C 1s emission peak for as received and cleaned ZnO$(10\bar{1}0)$.

8.4 Areal Density of Adsorbed Molecules

The surface density of adsorbed molecules can be roughly estimated from a comparison of the optical absorption of ZnO/molecule hybrids and molecular solutions of known molarity. The absorbance A of a molecular solution with concentration c and thickness d is $A = 1 - 10^{-\epsilon_{abs} c \cdot d}$ (solvent and vial are transparent), where ϵ_{abs} denotes the molar absorptivity. The maximum molar absorptivity of C3, C5, C7, C9 and C11 in methanol solution is, in units of 10^{-4}M^{-1}cm^{-1}, 3.46, 3.61, 4.55, 2.81, and 4.33, respectively,[40] and the maximum absorption of the hybrids systems is (in the same order) 46, 49, 65, 66, and 48 %.

Treating the ZnO nanorod/molecule hybrids in the same way as the solutions, i.e. neglecting the strong scattering of the nanostructure that enhances the absorption, yields a molecule concentration

$$c = -\frac{\log_{10}(1-A)}{\epsilon_{abs} \cdot d},$$
(8.4)

Where d denotes the nanorod length. The concentration can also be expressed as

$$c = \frac{n_S \cdot a \cdot \eta}{a \cdot d},$$
(8.5)

using the areal density of adsorbed molecules n_S, the illuminated area a and the surface amplification factor η of the nanorods. The latter is estimated to be about 30 from SEM pictures (section 4.3). Equalizing eq. (8.4) and (8.5) yields an average value for n_S of 2/nm^2. Since the light scatter-

ing enhances the absorption this value has to be regarded as an upper limit for the surface covering.

8.5 Phonon Heating

Photoexcitation in the direct band gap semiconductor $CuInSe_2$ occurs mostly without excitation of vibrational modes, so the average excess energy per electron for excitation with 1.55 eV photons is about $(\hbar\omega - E_{gap})/2 = 0.25 \, eV$. From the dispersion relation of the conduction band,[194] it follows that the photoexcited electrons have a maximum crystal momentum of $k_{max} \approx 0.1 \cdot 2\pi / a$. The maximum momentum transfer to phonons is about $2k_{max}$, so the fraction of the phonon momentum space that is involved in scattering with the hot electrons is on the order of $(0.2)^3 \approx 1\%$.
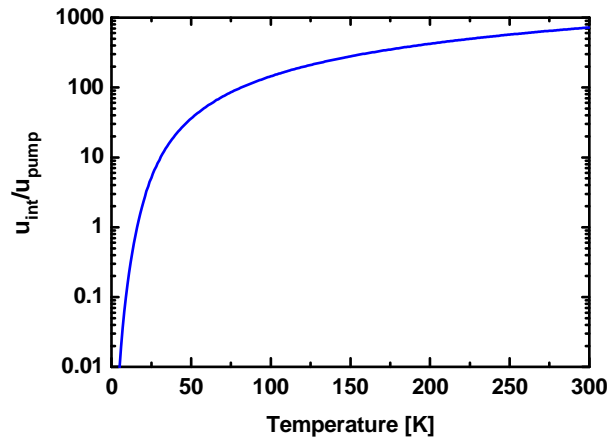

Figure 8-3 Internal energy density at constant volume[II] of the phonons in $CuInSe_2$ normalized to the 0.35 µJ/cm² energy density, which is brought into the material by the pump pulses from Figure 6-8.

By calculating the temperature dependent energy of phonons in this subspace and comparing it with the energy of a pump pulse (Figure 8-3), it can be seen that lattice temperature is increased by 10 K at 5 K, and by just 1 K at 30 K, which means that the phonon heating due to electron cooling is negligible down to at least 30 K.

[II] The internal energy is calculated by assuming a characteristic optical phonon energy of 25 meV for all optical branches except for (at least) two that have a lower phonon energy of 8 meV.[192] Longitudinal acoustic phonons are also included with linear energy-wave vector dispersion. The calculation is merely an estimate: Some of the optical branches may not be involved in the scattering at all. Then again, the internal energy at constant volume (calculation) is always smaller than the internal energy at constant pressure (experiment).[253]

8.6 Exactness of the Simple Drude Formula

Figure 8-4 (a) demonstrates that the mobility that is calculated in section 6.4.2 with eq (2.41) agrees very well with the simple Drude model (6.7). Figure 8-4 (b) shows that a fit of the Drude spectrum to the simulated mobility yields a relaxation time τ_D that is a very good estimate for $\langle\tau\rangle$, so that τ_D and $\langle\tau\rangle$ can practically be equalized for the discussion.
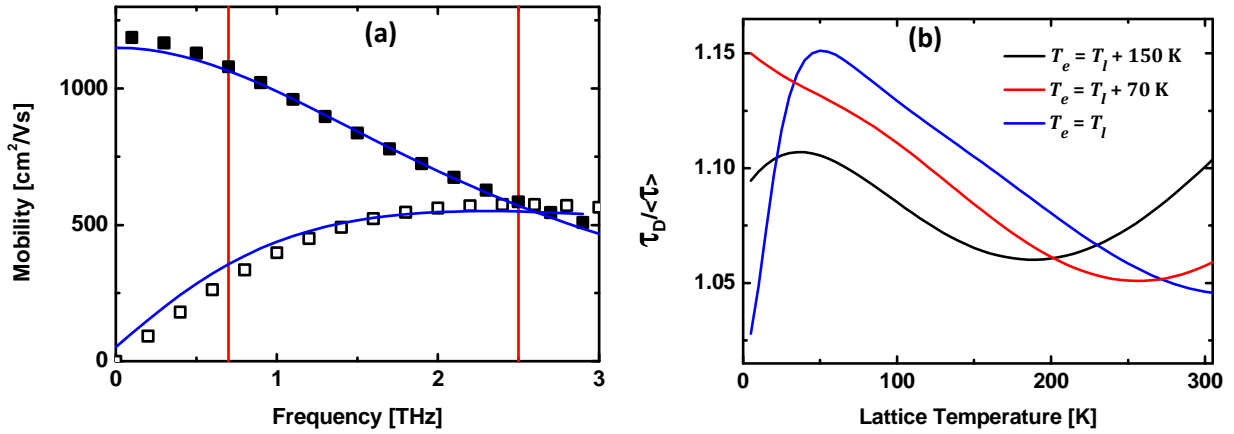

Figure 8-4 (a) Mobility spectrum calculated with eq. (2.40). Full/Open symbols denote the real/imaginary part. The solid lines are a Drude fit with eq. (6.7). The simulated mobility refers to the situation $T_e = T_l = 50\,K$ (using the parameters as in Figure 6-8 (a)) where the deviation of the simulated spectrum from a Drude spectrum is most pronounced (cf. part (b)). The lines indicate the fitting range, which was taken be the same as for the experimental data. (b) Ratio of fit parameter τ_D and the MRT $\langle\tau\rangle$ in dependence of lattice temperature and pump-probe delay.

8.7 Quantitative Aspects of the Matthiessen Rule

The magnitude of the scattering potential that reproduces a certain measured mobility depends strongly on the variety of the Matthiessen rule that is used to combine different scattering mechanisms. The Matthiessen rule is either stated in terms of the momentum relaxation time as

$$\frac{1}{\tau} = \frac{1}{\tau_{ac}} + \frac{1}{\tau_{ion}} + \frac{1}{\tau_{npo}} + \dots \tag{8.6}$$

or regarding the mobility as

$$\frac{1}{\mu} = \frac{1}{\mu_{ac}} + \frac{1}{\mu_{ion}} + \frac{1}{\mu_{npo}} + \dots \tag{8.7}$$

The former version is more meaningful than the latter because rates are additive. Nevertheless, the latter version is much more common; probably because it is more convenient to analyze the mobility in terms of the rather simple expressions for the mobilities due to each scattering mechanism(cf. section 2.2.3) instead of calculating the integral in eq. (2.40).
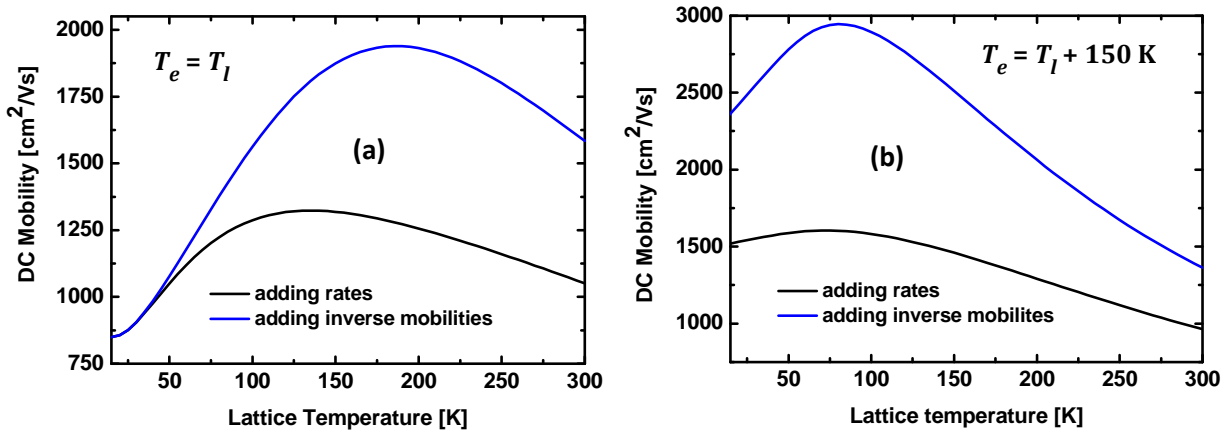

Figure 8-5 Temperature dependent DC mobility in presence of charged impurity and nonpolar optical phonon scattering for equilibrated (a) and hot electrons (b) evaluated with both variations of the Matthiessen rule: (8.6) and (8.7). The parameters of the calculation using eq. (2.40) are a charged impurity density $n_i = 4 \cdot 10^{17}$ cm^{-3}, and an electron density $n = 5.1 \cdot 10^{16}$ cm^{-3}, which corresponds to the situation in Figure 6-8. Instead of deformation potential scattering, nonpolar optical phonon scattering with $D_{op} = 3.53 \cdot 10^{11}$ eV m^{-1} is taken into account. The latter value is chosen to reproduce the room temperature mobility in Cu-rich CIS (Figure 6-8). The curve progression also demonstrates that electron-optical phonon scattering fails to reproduce the hot electron mobility in Cu-rich CIS (Figure 6-8).

Figure 8-5 demonstrates that the two versions of the Matthiessen rule generally lead to quantitatively different results. Calculating the overall mobility via eq. (8.7) results in an overestimation because at not too high temperatures the momentum relaxation time of optical phonon scattering becomes very large for electron energies $< \hbar\omega_{op}$ and accordingly so does the mobility μ_{po} or μ_{npo} if it is evaluated by (2.40). Hence, it does not contribute to the overall mobility in eq. (8.7). In contrast, the physically more meaningful treatment with eq. (8.6) still takes the finite values of the relaxation time for electron energies $> \hbar\omega_{op}$ into account.

Bibliography

1. Arrhenius, S. On the Influence of Carbonic Acid in the Air Upon the Temperature of the Ground. *Philos. Mag.* **41,** 237–276 (1896).
2. Arrhenius, S. *Worlds in the Making: The Evolution of the Universe*. (Harper, 1908).
3. Itzhaik, Y., Niitsoo, O., Page, M. & Hodes, G. Sb_2S_3-Sensitized Nanoporous TiO_2 Solar Cells. *J. Phys. Chem. C* **113,** 4254–4256 (2009).
4. Belaidi, A. *et al.* Influence of the Local Absorber Layer Thickness on the Performance of ZnO Nanorod Solar Cells. *Phys. Status Solidi R* **2,** 172–174 (2008).
5. O'Regan, B. & Grätzel, M. A Low-Cost, High-Efficiency Solar-Cell Based on Dye-Sensitized Colloidal Tio_2 Films. *Nature* **353,** 737–740 (1991).
6. Green, M. A., Emery, K., Hishikawa, Y., Warta, W. & Dunlop, E. D. Solar cell efficiency tables (version 39). *Prog. Photovoltaics* **20,** 12–20 (2012).
7. Rau, U. & Schock, H. W. Electronic Properties of $Cu(In,Ga)Se_2$ Heterojunction Solar Cells-Recent Achievements, Current Understanding, and Future Challenges. *Appl. Phys. A-Mater. Sci. Process.* **69,** 131–147 (1999).
8. Fließbach, T. *Elektrodynamik*. (Spektrum Akademischer Verlag, 2008).
9. Fließbach, T. *Mechanik*. (Spektrum Akademischer Verlag, 2009).
10. Němec, H., Kužel, P. & Sundström, V. Charge Transport in Nanostructured Materials for Solar Energy Conversion Studied by Time-Resolved Terahertz Spectroscopy. *J. Photoch. Photobio. A* **215,** 123–139 (2010).
11. Smith, N. V. Classical Generalization of the Drude Formula for the Optical Conductivity. *Phys. Rev. B* **64,** (2001).
12. Jacoboni, C. *Theory of Electron Transport in Semiconductors*. (Springer, 2010).
13. Ridley, B. K. *Quantum Processes in Semiconductors*. (Oxford University Press, USA, 2000).
14. Conwell, E. M. *High Field Transport in Semiconductors*. (Academic Press Inc, 1967).
15. Czycholl, G. *Theoretische Festkörperphysik*. (Springer DE, 2007).
16. Born, M. & Huang, K. *Dynamical Theory of Crystal Lattices*. (Clarendon Press, 1954).
17. Lundstrom, M. *Fundamentals of Carrier Transport*. (Cambridge University Press, 2000).
18. Callen, H. B. Electric Breakdown in Ionic Crystals. *Phys. Rev.* **76,** 1394–1402 (1949).
19. Ehrenreich, H. Electron Scattering in InSb. *J. Phys. Chem. Solids* **2,** 131–149 (1957).
20. Fröhlich, H. Electrons in Lattice Fields. *Adv. Phys.* **3,** 325 (1954).
21. Fröhlich, H. Theory of Electrical Breakdown in Ionic Crystals. *Proc. R. Soc. Lond. A* **160,** 230–241 (1937).
22. Chattopadhyay, D. & Queisser, H. J. Electron-Scattering by Ionized Impurities in Semiconductors. *Rev. Mod. Phys.* **53,** 745–768 (1981).
23. Born, M. & Oppenheimer, R. Zur Quantentheorie der Molekeln. *Ann. Phys.* **389,** 457–484 (1927).
24. Prezhdo, O. V., Duncan, W. R. & Prezhdo, V. V. Photoinduced Electron Dynamics at the Chromophore-Semiconductor Interface: A Time-Domain Ab Initio Perspective. *Prog. Surf. Sci.* **84,** 30–68 (2009).
25. May, V. & Kühn, O. *Charge and Energy Transfer Dynamics in Molecular Systems*. (Wiley-VCH, 2004).

26.   Pati, R. & Karna, S. P. Length-Dependence of Intramolecular Electron Transfer in Σ-Bonded Rigid Molecular Rods: An Ab Initio Molecular Orbital Study. *Chem. Phys. Lett.* **351,** 302–310 (2002).

27.   Zimmermann, C. *et al.* Experimental Fingerprints of Vibrational Wave-Packet Motion during Ultrafast Heterogeneous Electron Transfer. *J. Phys. Chem. B* **105,** 9245–9253 (2001).

28.   Nahata, A., Weling, A. & Heinz, T. A Wideband Coherent Terahertz Spectroscopy System Using Optical Rectification and Electro-Optic Sampling. *Appl. Phys. Lett* **69,** 2321–2323 (1996).

29.   Winnewisser, C. Elektrooptische Detektion von ultrakurzen elektromagnetischen Pulsen, Dissertation. (1999).

30.   Von Volkmann, K. Ultraschnelle Relaxationsdynamik über Phononen-Wechselwirkung in Festkörpersystemen, Dissertation. (2009).

31.   Piel, J., Riedle, E., Gundlach, L., Ernstorfer, R. & Eichberger, R. Sub-20 Fs Visible Pulses with 750 NJ Energy from a 100 kHz Noncollinear Optical Parametric Amplifier. *Opt. Lett.* **31,** 1289–1291 (2006).

32.   Ernstorfer, R. Spectroscopic Investigation of Photoinduced Heterogeneous Electron Transfer, Phd Thesis. (2004).

33.   Gundlach, L. Surface Electron Transfer Dynamics in the Presence of Organic Chromophores, PhD thesis. (2005).

34.   Němec, H., Kadlec, F. & Kužel, P. Methodology of an Optical Pump-Terahertz Probe Experiment: An Analytical Frequency-Domain Approach. *J. Chem. Phys.* **117,** 8454 (2002).

35.   Kužel, P., Kadlec, F. & Němec, H. Propagation of Terahertz Pulses in Photoexcited Media: Analytical Theory for Layered Systems. *J. Chem. Phys.* **127,** 024506 (2007).

36.   Nienhuys, H.-K. & Sundström, V. Intrinsic Complications in the Analysis of Optical-Pump, Terahertz Probe Experiments. *Phys. Rev. B* **71,** 235110 (2005).

37.   Němec, H., Kadlec, F., Kadlec, C., Kužel, P. & Jungwirth, P. Ultrafast Far-Infrared Dynamics Probed by Terahertz Pulses: A Frequency-Domain Approach. Ii. Applications. *J. Chem. Phys.* **122,** 104504 (2005).

38.   Beard, M. C., Turner, G. M. & Schmuttenmaer, C. A. Transient Photoconductivity in GaAs as Measured by Time-Resolved Terahertz Spectroscopy. *Phys. Rev. B* **62,** 15764–15777 (2000).

39.   Bitzer, A., Walther, M., Kern, A., Gorenflo, S. & Helm, H. Examination of the Spatial and Temporal Field Distributions of Single-Cycle Terahertz Pulses at a Beam Focus. *Appl. Phys. Lett.* **90,** 071112 (2007).

40.   Neubauer, A. Untersuchung der ultraschnellen Elektronentransferdynamik an organisch/anorganischen Grenzflächen unter Einsatz von Femtosekunden-Spektroskopie im Ultrahochvakuum, Dissertation. (2009).

41.   Ishii, H., Sugiyama, K., Ito, E. & Seki, K. Energy Level Alignment and Interfacial Electronic Structures at Organic/Metal and Organic/Organic Interfaces. *Adv. Mater.* **11,** 972–972 (1999).

42.   Töben, L. Untersuchung zur Energetik und Dynamik von Elektronen an MOCVD-gewachsenen III-V-Halbleiter Oberflächen. Dissertation, Technische Universität Berlin. (2002).

43.   Göppert-Mayer, M. Über Elementarakte mit zwei Quantensprüngen. *Ann. Phys.* **401,** 273–294 (1931).

44.   Gundlach, L., Ernstorfer, R., Riedle, E., Eichberger, R. & Willig, F. Femtosecond Two-Photon Photoemission at 150 kHz Utilizing Two Noncollinear Optical Parametric Amplifiers for Measuring Ultrafast Electron Dynamics. *Appl. Phys. B-Lasers O.* **80,** 727–731 (2005).

45.   Ernst, K., Belaidi, A. & Könenkamp, R. Solar Cell with Extremely Thin Absorber on Highly Structured Substrate. *Semicond. Sci. Technol.* **18,** 475–479 (2003).

46.   Anderson, N. A. & Lian, T. Ultrafast Electron Transfer at the Molecule-Semiconductor Nanoparticle Interface. *Annu. Rev. Phys. Chem.* **56,** 491–519 (2005).

47.   Tiwana, P., Parkinson, P., Johnston, M., Snaith, H. & Herz, L. Ultrafast Terahertz Conductivity Dynamics in Mesoporous TiO_2: Influence of Dye Sensitization and Surface Treatment in Solid-State Dye-Sensitized Solar Cells. *J. Phys. Chem. C* **114,** 1365–1371 (2010).

48.   Němec, H. *et al.* Influence of the Electron-Cation Interaction on Electron Mobility in Dye-Sensitized ZnO and TiO_2 Nanocrystals: A Study Using Ultrafast Terahertz Spectroscopy. *Phys. Rev. Lett.* **104,** 197401 (2010).

49.   Pijpers, J. J. H., Ulbricht, R., Derossi, S., Reek, J. N. H. & Bonn, M. Picosecond Electron Injection Dynamics in Dye-Sensitized Oxides in the Presence of Electrolyte. *J. Phys. Chem. C* **115,** 2578–2584 (2011).

50.   Tiwana, P., Docampo, P., Johnston, M. B., Snaith, H. J. & Herz, L. M. Electron Mobility and Injection Dynamics in Mesoporous ZnO, SnO_2, and TiO_2 Films Used in Dye-Sensitized Solar Cells. *ACS Nano* **5,** 5158–5166 (2011).

51.   Žídek, K. *et al.* Electron Transfer in Quantum-Dot-Sensitized ZnO Nanowires: Ultrafast Time-Resolved Absorption and Terahertz Study. *J. Am. Chem. Soc.* **134,** 12110–12117 (2012).

52.   Liu, C. P. *et al.* Enhanced Performance by Incorporation of Zinc Oxide Nanowire Array for Organic-Inorganic Hybrid Solar Cells. *Appl. Phys. Lett.* **100,** (2012).

53.   Yao, C.-Z. *et al.* Controllable Electrochemical Synthesis and Photovoltaic Performance of Zno/Cds Core-Shell Nanorod Arrays on Fluorine-Doped Tin Oxide. *J. Power Sources* **207,** 222–228 (2012).

54.   Krunks, M. *et al.* Extremely Thin Absorber Layer Solar Cells on Zinc Oxide Nanorods by Chemical Spray. *Sol. Energy Mater. Sol. Cells* **94,** 1191–1195 (2010).

55.   Zhang, J., Que, W., Shen, F. & Liao, L. $CuInSe_2$ Nanocrystals/Cds Quantum Dots/Zno Nanowire Arrays Heterojunction for Photovoltaic Applications. *Sol. Energy Mater. Sol. Cells* **103,** 30–34 (2012).

56.   Tena-Zaera, R. *et al.* Fabrication and Characterization of Zno Nanowires/CdSe/CuSCN ETA-Solar Cell. *C. R. Chim.* **9,** 717–729 (2006).

57.   Tena-Zaera, R. *et al.* Zno/CdTe/CuSCN, a Promising Heterostructure to Act as Inorganic ETA-Solar Cell. *Thin Solid Films* **483,** 372–377 (2005).

58.   Kuang, Y., van der Werf, K. H. M., Houweling, Z. S. & Schropp, R. E. I. Nanorod Solar Cell with an Ultrathin a-Si:H Absorber Layer. *Appl. Phys. Lett.* **98,** 113111–113111–3 (2011).

59.   Tornow, J. *et al.* Charge Separation and Recombination in Radial Zno/In_2S_3/CuSCN Heterojunction Structures. *J. Appl. Phys.* **108,** (2010).

60.   Dittrich, T. *et al.* Formation of the Charge Selective Contact in Solar Cells with Extremely Thin Absorber Based on ZnO-Nanorod/In_2S_3/CuSCN. *J. Appl. Phys.* **105,** 034509 (2009).

61.   Janotti, A. & Van de Walle, C. G. Fundamentals of Zinc Oxide as a Semiconductor. *Rep. Prog. Phys.* **72,** (2009).

62.   Özgür, U. *et al.* A Comprehensive Review of Zno Materials and Devices. *J. Appl. Phys.* **98,** (2005).

63.   McCluskey, M. D. & Jokela, S. J. Defects in ZnO. *J. Appl. Phys.* **106,** (2009).

64.   Wöll, C. The Chemistry and Physics of Zinc Oxide Surfaces. *Prog. Surf. Sci.* **82,** 55–120 (2007).

65.   Srikant, V. & Clarke, D. On the Optical Band Gap of Zinc Oxide. *J. Appl. Phys.* **83,** 5447–5451 (1998).

66.   Bates, C. H., White, W. B. & Roy, R. New High-Pressure Polymorph of Zinc Oxide. *Science* **137,** 993–993 (1962).

67.   Kisi, E. & Elcombe, M. u-Parameters for the Wurtzite Structure of ZnS and ZnS Using Powder Neutron-Diffraction. *Acta Crystallogr. Sect. C-Cryst. Struct. Commun.* **45,** 1867–1870 (1989).

68.   Janotti, A. & Van de Walle, C. G. Native Point Defects in Zno. *Phys. Rev. B* **76,** 165202 (2007).

69.   Ozawa, K. & Mase, K. Angle-Resolved Photoelectron Spectroscopy Study of Hydrogen Adsorption on ZnO(10-10). *Phys. Status Solidi A-Appl. Mat.* **207,** 277–281 (2010).

70.   Ozawa, K. & Mase, K. Metallization of Zno(10-10) by Adsorption of Hydrogen, Methanol, and Water: Angle-Resolved Photoelectron Spectroscopy. *Phys. Rev. B* **81,** (2010).

71.   Ozawa, K. & Mase, K. Comparison of the Surface Electronic Structures of H-Adsorbed Zno Surfaces: An Angle-Resolved Photoelectron Spectroscopy Study. *Phys. Rev. B* **83,** 125406 (2011).

72.   Eger, D., Many, A. & Goldstein, Y. Quantum Properties of Strong Accumulation Layers on ZnO Surfaces. *Surf. Sci.* **58,** 18–24 (1976).

73.   Eger, D. & Goldstein, Y. Quantization Effects in ZnO Accumulation Layers in Contact with an Electrolyte. *Phys. Rev. B* **19,** 1089–1097 (1979).

74.   Hullavarad, S., Hullavarad, N., Look, D. & Claflin, B. Persistent Photoconductivity Studies in Nanostructured ZnO UV Sensors. *Nanoscale Res. Lett.* **4,** 1421–1427 (2009).

75.   Collins, R. J. & Thomas, D. G. Photoconduction and Surface Effects with Zinc Oxide Crystals. *Phys. Rev.* **112,** 388–395 (1958).

76.   Heiland, G. Die elektrische Leitfähigkeit an der Oberflache von Zinkoxidkristallen. *Z. Phys.* **142,** 415–432 (1955).

77.   Bao, J. *et al.* Photoinduced Oxygen Release and Persistent Photoconductivity in ZnO Nanowires. *Nanoscale Res. Lett.* **6,** (2011).

78.   Claflin, B., Look, D. C., Park, S. J. & Cantwell, G. Persistent N-Type Photoconductivity in P-Type ZnO. *J. Cryst. Growth* **287,** 16–22 (2006).

79.   Laiho, R., Stepanov, Y. P., Vlasenko, M. P. & Vlasenko, L. S. Persistent Photoconductivity of ZnO. *Physica B* **404,** 4787–4790 (2009).

80.   Moazzami, K., Murphy, T. E., Phillips, J. D., Cheung, M. C.-K. & Cartwright, A. N. Sub-Bandgap Photoconductivity in ZnO Epilayers and Extraction of Trap Density Spectra. *Semicond. Sci. Technol.* **21,** 717–723 (2006).

81.   Reemts, J. & Kittel, A. Persistent Photoconductivity in Highly Porous ZnO Films. *J. Appl. Phys.* **101,** (2007).

82.   Kuriyama, K., Matsumoto, K., Suzuki, Y., Kushida, K. & Xu, Q. Persistent Photoconductivity and Thermally Stimulated Current Related to Electron-Irradiation Induced Defects in Single Crystal ZnO Bulk. *Solid State Commun.* **149,** 1347–1350 (2009).

83.   Claflin, B. & Look, D. C. UV Light-Induced Changes to the Surface Conduction in Hydrothermal ZnO. *J. Vac. Sci. Technol. B* **27,** 1722–1725 (2009).

84.   Cunningham, J., Finn, E. & Samman, N. Photo-Assisted Surface-Reactions Studied by Dynamic Mass-Spectrometry. *Faraday Discuss.* **58,** 160–174 (1974).

85.   Shapira, Y., Cox, S. & Lichtman, D. Chemisorption, Photodesorption and Conductivity Measurements on ZnO Surfaces. *Surf. Sci.* **54,** 43–59 (1976).

86.   Naghavi, N. *et al.* Buffer Layers and Transparent Conducting Oxides for Chalcopyrite Cu(In,Ga)(S,Se)$_2$ Based Thin Film Photovoltaics: Present Status and Current Developments. *Prog. Photovoltaics* **18,** 411–433 (2010).

87.   Rehwald, W. & Harbeke, G. On the Conduction Mechanism in Single Crystal β-Indium Sulfide In$_2$S$_3$. *J. Phys. Chem. Solids* **26,** 1309–1318, IN7, IN8, 1319–1324 (1965).

88.   Paulraj, M. *et al.* Characterisation of In$_2$S$_3$ and ZnO Thin Films for Photovoltaic Application Using Photothermal Deflection Technique. *J. Phys. IV* **125,** 469–472 (2005).

89.   Harbecke, B. Coherent and Incoherent Reflection and Transmission of Multilayer Structures. *Appl. Phys. B-Photo.* **39,** 165–170 (1986).

90.   Kim, W.-T. & Kim, C.-D. Optical Energy Gaps of β-In$_2$S$_3$ Thin Films Grown by Spray Pyrolysis. *J. Appl. Phys.* **60,** 2631 (1986).

91.   Zhao, Z. *et al.* Band-Edge Electronic Structure of β-In$_2$S$_3$: The Role of s or p Orbitals of Atoms at Different Lattice Positions. *ChemPhysChem* **13,** 1551–1556 (2012).

92.   Rooymans, C. A New Type of Cation-Vacancy Ordering in the Spinel Lattice of In$_2$S$_3$. *J. Inorg. Nucl. Chem.* **11,** 78–79 (1959).

93.   Steigmann, G. A., Sutherland, H. H. & Goodyear, J. Crystal Structure of β-In$_2$S$_3$. *Acta Crystallogr.* **19,** 967 (1965).

94.   Peterson, R. B., Fields, C. L. & Gregg, B. A. Epitaxial Chemical Deposition of ZnO Nanocolumns from NaOH Solutions. *Langmuir* **20,** 5114–5118 (2004).

95.   Tornow, J. Trennung und Rekombination von Ladungsträgern in Solarzellen mit nanostrukturierter ZnO-Elektrode, Dissertation, Christian Albrechts Universität zu Kiel. (2010).

96.   Allsop, N. A. *et al.* Indium Sulfide Thin Films Deposited by the Spray Ion Layer Gas Reaction Technique. *Thin Solid Films* **513,** 52–56 (2006).

97.   Xi, J. Q. *et al.* Optical Thin-Film Materials with Low Refractive Index for Broadband Elimination of Fresnel Reflection. *Nat. Photonics* **1,** 176–179 (2007).

98.   Yu, P. Y. & Cardona, M. *Fundamentals of Semiconductors.* (Springer, 2010).

99.   Wang, J. *et al.* Oxygen Vacancy Induced Band-Gap Narrowing and Enhanced Visible Light Photocatalytic Activity of ZnO. *ACS Appl. Mater. Interfaces* **4,** 4024–4030 (2012).

100.   Pankove, J. I. *Optical Processes in Semiconductors.* (Dover, 1975).

101.   Bruggeman, D. A. G. Berechnung verschiedener physikalischer Konstanten von heterogenen Substanzen. I. Dielektrizitätskonstanten und Leitfähigkeiten der Mischkörper aus isotropen Substanzen. *Ann. Phys.* **416,** 636–664 (1935).

102.   Garnett, J. C. M. Colours in Metal Glasses and in Metallic Films. *Philos. T. R. Soc. Lond.* **203,** 385 –420 (1904).

103.   Wood, D. M. & Ashcroft, N. W. Effective Medium Theory of Optical Properties of Small Particle Composites. *Philos. Mag.* **35,** 269–280 (1977).

104.   Nicorovici, N. A., McPhedran, R. C. & Milton, G. W. Optical and Dielectric Properties of Partially Resonant Composites. *Phys. Rev. B* **49,** 8479–8482 (1994).

105.   Azad, A. K., Han, J. & Zhang, W. Terahertz Dielectric Properties of High-Resistivity Single-Crystal Zno. *Appl. Phys. Lett.* **88,** 021103 (2006).

106.   Baxter, J. B. & Schmuttenmaer, C. A. Carrier Dynamics in Bulk ZnO. II. Transient Photoconductivity Measured by Time-Resolved Terahertz Spectroscopy. *Phys. Rev. B* **80,** 235206 (2009).

107.   Hendry, E., Koeberg, M. & Bonn, M. Exciton and Electron-Hole Plasma Formation Dynamics in ZnO. *Phys. Rev. B* **76,** 045214 (2007).

108.   Zhang, X. H. *et al.* Terahertz Dielectric Response and Optical Conductivity of N-Type Single-Crystal ZnO Epilayers Grown by Metalorganic Chemical Vapor Deposition. *J. Appl. Phys.* **107,** 033101 (2010).

109.   Baxter, J. B. & Schmuttenmaer, C. A. Conductivity of ZnO Nanowires, Nanoparticles, and Thin Films Using Time-Resolved Terahertz Spectroscopy. *J. Phys. Chem. B* **110,** 25229–25239 (2006).

110.   Němec, H., Kužel, P. & Sundström, V. Far-Infrared Response of Free Charge Carriers Localized in Semiconductor Nanoparticles. *Phys. Rev. B* **79,** 115309 (2009).

111.   Lloyd-Hughes, J. & Jeon, T.-I. A Review of the Terahertz Conductivity of Bulk and Nano-Materials. *J. Infrared Millim. Terahertz Waves* **33,** 871–925 (2012).

112.   Mics, Z. *et al.* Charge Transport and Localization in Nanocrystalline CdS Films: A Time-Resolved Terahertz Spectroscopy Study. *Phys. Rev. B* **83,** 155326 (2011).

113.   Baer, W. S. Faraday Rotation in ZnO: Determination of the Electron Effective Mass. *Phys. Rev.* **154,** 785–789 (1967).

114.   Yan, Q. *et al.* Strain Effects and Band Parameters in MgO, ZnO, and CdO. *Appl. Phys. Lett.* **101,** 152105–152105–4 (2012).

115.   Shockley, W. & Read, W. Statistics of the Recombinations of Holes and Electrons. *Phys. Rev.* **87,** 835–842 (1952).

116.   Seto, J. Electrical Properties of Polycrystalline Silicon Films. *J. Appl. Phys.* **46,** 5247–5254 (1975).

117.   Shklovskii, B. I., Shklovskiĭ, B. I. & Ėfros, A. L. *Electronic Properties of Doped Semiconductors.* (Springer-Verlag, 1984).

118.   Orenstein, J. & Kastner, M. Photocurrent Transient Spectroscopy - Measurement of the Density of Localized States in α-As$_2$Se$_3$. *Phys. Rev. Lett.* **46,** 1421–1424 (1981).

119.   Tiedje, T. & Rose, A. A Physical Interpretation of Dispersive Transport in Disordered Semiconductors. *Sol. Stat. Comm.* **37,** 49–52 (1981).

120.   Mott, N. The Mobility Edge Since 1967. *J. Phys. C Solid State* **20,** 3075–3102 (1987).

121.   Monroe, D. Hopping in Exponential Band Tails. *Phys. Rev. Lett.* **54,** 146–149 (1985).

122.   Garlick, G. F. J., Springford, M. & Checinska, H. The Infrared Emission of Indium Sesquisulphide. *Proc. Phys. Soc.* **82,** 16–22 (1963).

123.   Piris, J. *et al.* Efficient Photoinduced Charge Injection from Chemical Bath Deposited CdS into Mesoporous TiO$_2$ Probed with Time-Resolved Microwave Conductivity. *J. Phys. Chem. C* **112,** 7742–7749 (2008).

124.   Furube, A. *et al.* Ultrafast Stepwise Electron Injection from Photoexcited Ru-Complex into Nanocrystalline ZnO Film via Intermediates at the Surface. *J. Phys. Chem. B* **107,** 4162–4166 (2003).

125.   Furube, A. *et al.* Ultrafast Direct and Indirect Electron-Injection Processes in a Photoexcited Dye-Sensitized Nanocrystalline Zinc Oxide Film: The Importance of Exciplex Intermediates at the Surface. *J. Phys. Chem. B* **108,** 12583–12592 (2004).

126.   Stockwell, D. *et al.* Comparison of Electron-Transfer Dynamics from Coumarin 343 to TiO$_2$, SnO$_2$, and ZnO Nanocrystalline Thin Films: Role of Interface-Bound Charge-Separated Pairs. *J. Phys. Chem. C* **114,** 6560–6566 (2010).

127.   Huber, R., Spörlein, S., Moser, J. E., Grätzel, M. & Wachtveitl, J. The Role of Surface States in the Ultrafast Photoinduced Electron Transfer from Sensitizing Dye Molecules to Semiconductor Colloids. *J. Phys. Chem. B* **104,** 8995–9003 (2000).

128.   Wiberg, J. *et al.* Effect of Anchoring Group on Electron Injection and Recombination Dynamics in Organic Dye-Sensitized Solar Cells. *J. Phys. Chem. C* **113,** 3881–3886 (2009).

129.   Gundlach, L., Letzig, T. & Willig, F. Test of Theoretical Models for Ultrafast Heterogeneous Electron Transfer with Femtosecond Two-Photon Photoemission Data. *J. Chem. Sci.* **121,** 561–574 (2009).

130.   Gundlach, L., Ernstorfer, R. & Willig, F. Ultrafast Interfacial Electron Transfer from the Excited State of Anchored Molecules into a Semiconductor. *Prog. Surf. Sci.* **82,** 355–377 (2007).

131.   Gundlach, L., Ernstorfer, R. & Willig, F. Dynamics of Photoinduced Electron Transfer from Adsorbed Molecules into Solids. *Appl. Phys. A-Mater.* **88,** 481–495 (2007).

132.   Gundlach, L., Ernstorfer, R. & Willig, F. Escape Dynamics of Photoexcited Electrons at Catechol: TiO$_2$(110). *Phys. Rev. B* **74,** (2006).

133.   Hannappel, T., Burfeindt, B., Storck, W. & Willig, F. Measurement of Ultrafast Photoinduced Electron Transfer from Chemically Anchored Ru-Dye Molecules into Empty Electronic States in a Colloidal Anatase TiO$_2$ Film. *J. Phys. Chem. B* **101,** 6799–6802 (1997).

134.	Diebold, U., Koplitz, L. V. & Dulub, O. Atomic-Scale Properties of Low-Index ZnO Surfaces. *Appl. Surf. Sci.* **237,** 336–342 (2004).

135.	Vayssieres, L., Keis, K., Hagfeldt, A. & Lindquist, S.-E. Three-Dimensional Array of Highly Oriented Crystalline ZnO Microtubes. *Chem. Mater.* **13,** 4395–4398 (2001).

136.	Mahrt, J. *Angeregte Dimere und Excimere des Perylens, PhD Thesis, Technical University Berlin.* (1995).

137.	Neubauer, A., Szarko, J. M., Bartelt, A. F., Eichberger, R. & Hannappel, T. Photophysical Study of Perylene/TiO$_2$ and Perylene/ZnO Varying Interfacial Couplings and the Chemical Environment. *J. Phys. Chem. C* **115,** 5683–5691 (2011).

138.	Bartelt, A. F., Schütz, R., Neubauer, A., Hannappel, T. & Eichberger, R. Influence of TiO$_2$/Perylene Interface Modifications on Electron Injection and Recombination Dynamics. *J. Phys. Chem. C* **113,** 21233–21241 (2009).

139.	Szarko, J. M. *et al.* The Ultrafast Temporal and Spectral Characterization of Electron Injection from Perylene Derivatives into ZnO and TiO$_2$ Colloidal Films. *J. Phys. Chem. C* **112,** 10542–10552 (2008).

140.	De Angelis, F. Direct vs. Indirect Injection Mechanisms in Perylene Dye-Sensitized Solar Cells: A DFT/TDDFT Investigation. *Chem. Phys. Lett* **493,** 323–327 (2010).

141.	Persson, P. & Ojamae, L. Periodic Hartree-Fock Study of the Adsorption of Formic Acid on ZnO(10-10). *Chem. Phys. Lett.* **321,** 302–308 (2000).

142.	Persson, P., Lunell, S. & Ojamae, L. Quantum Chemical Prediction of the Adsorption Conformations and Dynamics at HCOOH-Covered Zno(10-10) Surfaces. *Int. J. Quantum Chem.* **89,** 172–180 (2002).

143.	Tian, X., Xu, J. & Xie, W. Controllable Modulation of the Electronic Structure of ZnO(10-10) Surface by Carboxylic Acids. *J. Phys. Chem. C* **114,** 3973–3980 (2010).

144.	Moreira, N., da Rosa, A. & Frauenheim, T. Covalent Functionalization of ZnO Surfaces: A Density Functional Tight Binding Study. *Appl. Phys. Lett.* **94,** (2009).

145.	Amat, A. & De Angelis, F. Challenges in the Simulation of Dye-Sensitized ZnO Solar Cells: Quantum Confinement, Alignment of Energy Levels and Excited State Nature at the Dye/Semiconductor Interface. *Phys. Chem. Chem. Phys.* **14,** 10662–10668 (2012).

146.	De Angelis, F. Private Communcation of Unbublished DFT Calculations. (2012).

147.	Wang, Y. *et al.* Hydrogen Induced Metallicity on the ZnO(10-10) Surface. *Phys. Rev. Lett.* **95,** (2005).

148.	Jia, J., Shi, D., Zhao, J. & Wang, B. Metallization of ZnO Nanowires from Partial Hydrogen Adsorption. *Nanotechnology* **18,** (2007).

149.	Tisdale, W. A., Muntwiler, M., Norris, D. J., Aydil, E. S. & Zhu, X.-Y. Electron Dynamics at the ZnO (10-10) Surface. *J. Phys. Chem. C* **112,** 14682–14692 (2008).

150.	Ernstorfer, R. *et al.* Role of Molecular Anchor Groups in Molecule-to-Semiconductor Electron Transfer. *J. Phys. Chem. B* **110,** 25383–25391 (2006).

151.	Ramakrishna, S., Seideman, T., Willig, F. & May, V. Theory of Coherent Molecule to Surface Electron Injection: An Analytical Model. *J. Chem. Sci.* **121,** 589–594 (2009).

152.	Lorenc, M. *et al.* Artifacts in Femtosecond Transient Absorption Spectroscopy. *Appl. Phys. B-Lasers O.* **74,** 19–27 (2002).

153.	Sato, K. & Adachi, S. Optical Properties of ZnTe. *J. Appl. Phys.* **73,** 926 (1993).

154.	Maroncelli, M. & Fleming, G. R. Picosecond Solvation Dynamics of Coumarin 153: The Importance of Molecular Aspects of Solvation. *J. Chem. Phys.* **86,** 6221–6239 (1987).

155.	Allen, M. W. *et al.* Bulk transport measurements in ZnO: The effect of surface electron layers. *Phys. Rev. B* **81,** 075211 (2010).

156.   Moreira, N., Aradi, B., da Rosa, A. & Frauenheim, T. Native Defects in ZnO Nanowires: Atomic Relaxations, Relative Stability, and Defect Healing with Organic Acids. *J. Phys. Chem. C* **114,** 18860–18865 (2010).

157.   Zhukov, V. P., Echenique, P. M. & Chulkov, E. V. Two Types of Excited Electron Dynamics in Zinc Oxide. *Phys. Rev. B* **82,** (2010).

158.   Kim, Y., Ahn, J., Kim, B. G. & Yee, D.-S. Terahertz Birefringence in Zinc Oxide. *Jpn. J. Appl. Phys.* **50,** 030203 (2011).

159.   Gonzalez, R. J., Zallen, R. & Berger, H. Infrared Reflectivity and Lattice Fundamentals in Anatase TiO_2. *Phys. Rev. B* **55,** 7014–7017 (1997).

160.   Van Daal, H. J. The Static Dielectric Constant of SnO_2. *J. Appl. Phys.* **39,** 4467–4469 (1968).

161.   Nemec, H. *et al.* Influence of the Electron-Cation Interaction on Electron Mobility in Dye-Sensitized ZnO and TiO2 Nanocrystals: A Study Using Ultrafast Terahertz Spectroscopy. *Physical Review Letters* **104,** (2010).

162.   Anderson, N., Ai, X. & Lian, T. Electron Injection Dynamics from Ru Polypyridyl Complexes to ZnO Nanocrystalline Thin Films. *J. Phys. Chem. B* **107,** 14414–14421 (2003).

163.   Huang, J., Stockwell, D., Boulesbaa, A., Guo, J. & Lian, T. Comparison of Electron Injection Dynamics from Rhodamine B to In_2O_3, SnO_2, and Zno Nanocrystalline Thin Films. *J. Phys. Chem. C* **112,** 5203–5212 (2008).

164.   AbuShama, J., Noufi, R., Johnston, S., Ward, S. & Wu, X. in *IEEE Phot. Spec. Conf.* 299–302 (2005).

165.   Hanna, G., Jasenek, A., Rau, U. & Schock, H. w. Open Circuit Voltage Limitations in $CuIn_{1-x}Ga_xSe_2$ Thin-Film Solar Cells – Dependence on Alloy Composition. *Phys. Status Solidi A* **179,** R7–R8 (2000).

166.   Balboul, M. *et al.* Correlation of Structure Parameters of Absorber Layer with Efficiency of $Cu(In,Ga)Se_2$ Solar Cell. *Appl. Phys. A-Mater. Sci. Process.* **92,** 557–563 (2008).

167.   Jackson, P. *et al.* New World Record Efficiency for $Cu(In,Ga)Se_2$ Thin-Film Solar Cells Beyond 20%. *Prog. Photovoltaics* **19,** 894–897 (2011).

168.   Siebentritt, S., Papathanasiou, N. & Lux-Steiner, M. C. Potential Fluctuations in Compensated Chalcopyrites. *Physica B* **376–377,** 831–833 (2006).

169.   Dirnstorfer, I. *et al.* Characterization of $CuIn(Ga)Se_2$ Thin Films - II. In-Rich Layers. *Phys. Status Solidi A* **168,** 163–175 (1998).

170.   Krustok, J., Collan, H., Yakushev, M. & Hjelt, K. The Role of Spatial Potential Fluctuations in the Shape of the PL Bands of Multinary Semiconductor Compounds. *Phys. Scr.* **T79,** 179–182 (1999).

171.   Bauknecht, A., Siebentritt, S., Albert, J. & Lux-Steiner, M. C. Radiative Recombination via Intrinsic Defects in $Cu_xGa_ySe_2$. *J. Appl. Phys.* **89,** 4391–4400 (2001).

172.   Bacewicz, R., Zuk, P. & Trykozko, R. Photoluminescence Study of $ZnO/CdS/Cu(In,Ga)Se_2$ Solar Cells. *Opto-Electron. Rev.* **11,** 277–280 (2003).

173.   Dirnstorfer, I. *et al.* Postgrowth Thermal Treatment of $CuIn(Ga)Se_2$: Characterization of Doping Levels in in-Rich Thin Films. *J. Appl. Phys.* **85,** 1423–1428 (1999).

174.   Jagomägi, A. *et al.* Photoluminescence Studies of Heavily Doped $CuInTe_2$ Crystals. *Physica B* **337,** 369–374 (2003).

175.   Krustok, J., Raudoja, J., Yakushev, M., Pilkington, R. D. & Collan, H. On the Shape of the Close-to-Band-Edge Photoluminescent Emission Spectrum in Compensated $CuGaSe_2$. *Phys. Status Solidi A* **173,** 483–490 (1999).

176.   Liao, Y.-K. *et al.* Observation of Unusual Optical Transitions in Thin-Film $Cu(In,Ga)Se_2$ Solar Cells. *Opt. Express* **20,** A836–A842 (2012).

177. Romero, M. J. *et al. A Comparative Study of the Defect Point Physics and Luminescence of the Kesterites Cu_2ZnSnS_4 and $Cu_2ZnSnSe_4$ and Chalcopyrite Cu(In,Ga)Se₂*. (IEEE, 2012).

178. Schumacher, S. A., Botha, J. R. & Alberts, V. Photoluminescence Study of Potential Fluctuations in Thin Layers of $Cu(In_{0.75}Ga_{0.25})(S_ySe_{1-y})_2$. *J. Appl. Phys.* **99,** 063508–063508–8 (2006).

179. Siebentritt, S., Papathanasiou, N. & Lux-Steiner, M. Photoluminescence Excitation Spectroscopy of Highly Compensated $CuGaSe_2$. *Phys. Status Solidi B* **242,** 2627–2632 (2005).

180. Keyes, B. M., Dippo, P., Metzger, W. K., AbuShama, J. & Noufi, R. Changes in the Dominant Recombination Mechanisms of Polycrystalline Cu(In,Ga)Se₂ Occurring During Growth. *J. Appl. Phys.* **94,** 5584–5591 (2003).

181. Turcu, M., Pakma, O. & Rau, U. Interdependence of Absorber Composition and Recombination Mechanism in $Cu(In,Ga)(Se,S)_2$ Heterojunction Solar Cells. *Applied Physics Letters* **80,** 2598–2600 (2002).

182. Gütay, L. *et al.* Influence of Copper Excess on the Absorber Quality of $CuInSe_2$. *Appl. Phys. Lett.* **99,** 151912–151912–3 (2011).

183. Kistaiah, P., Venudhar, Y. C., Murthy, K. S., Iyengar, L. & Rao, K. V. K. Temperature Dependence of Tetragonal Distortion and Thermal Expansion of Copper Indium Selenide. *J. Phys. D Appl. Phys.* **14,** 1311–1316 (1981).

184. Stephan, C., Schorr, S., Tovar, M. & Schock, H.-W. Comprehensive Insights into Point Defect and Defect Cluster Formation in $CuInSe_2$. *Appl. Phys. Lett.* **98,** (2011).

185. Zunger, A., Zhang, S. B. & Wei, S.-H. Revisiting the Defect Physics in $CuInSe_2$ and $CuGaSe_2$. in *IEEE Phot. Spec. Conf.* 313 –318 (1997).

186. Wei, S. H. & Zhang, S. B. Defect Properties of $CuInSe_2$ and $CuGaSe_2$. *J. Phys. Chem. Solids* **66,** 1994–1999 (2005).

187. Pohl, J., Unold, T. & Albe, K. Antisite Traps and Metastable Defects in Cu(In,Ga)Se₂ Thin-Film Solar Cells Studied by Screened-Exchange Hybrid Density Functional Theory. *arXiv:1205.2556* (2012). at <http://arxiv.org/abs/1205.2556>

188. Yakushev, M. V. *et al.* Excited States of the A and B Free Excitons in $CuInSe_2$. *Jpn. J. Appl. Phys.* **50,** (2011).

189. Chattopadhyay, K., Sanyal, I., Chaudhuri, S. & Pal, A. Burstein-Moss Shift in CuInSe₂ Films. *Vacuum* **42,** 915–918 (1991).

190. Fernández, B. & Wasim, S. M. Sound Velocities and Elastic Moduli in $CuInTe_2$ and $CuInSe_2$. *Phys. Status Solidi A* **122,** 235–242 (1990).

191. Quintero, M., Rincon, C., Tovar, R. & Woolley, J. C. Optical energy gap values and deformation potentials in four $Cu-III-VI_2$ chalcopyrite compounds. *J. Phys. Condens. Mat.* **4,** 1281–1289 (1992).

192. Neumann, H. Lattice Vibrational, Thermal and Mechanical Properties of $CuInSe_2$. *Solar Cells* **16,** 399–418 (1986).

193. Alonso, M., Wakita, K., Pascual, J., Garriga, M. & Yamamoto, N. Optical Functions and Electronic Structure of $CuInSe_2$, $CuGaSe_2$, $CuInS_2$, and $CuGaS_2$. *Phys. Rev. B* **63,** (2001).

194. Chen, R. & Persson, C. Parameterization of $CuIn_{1-x}Ga_xSe_2$ (x = 0, 0.5, and 1) Energy Bands. *Thin Solid Films* **519,** 7503–7507 (2011).

195. Persson, C. Anisotropic Hole-Mass Tensor of $CuIn_{1-x}Ga_xSe_2$: Presence of Free Carriers Narrows the Energy Gap. *Appl. Phys. Lett.* **93,** 072106–072106–3 (2008).

196. Weinert, H., Neumann, H., Höbler, H.-J., Kühn, G. & van Nam, N. Infrared Faraday Effect in n-Type $CuInSe_2$. *Phys. Status Solidi A* **81,** K59–K61 (1977).

197. Arushanov, E. *et al.* Shubnikov–de Haas Oscillations in n-$CuInSe_2$. *Appl. Phys. Lett.* **61,** 958–960 (1992).

198.   Wasim, S. M. *et al.* Density of States Effective Mass of N-Type CuInSe$_2$ from the Temperature Dependence of Hall Coefficient in the Activation Regime. *J. Phys. Chem. Solids* **66,** 1887–1890 (2005).

199.   Neumann, H., Kissinger, W., Sobotta, H., Riede, V. & Kühn, G. Hole Effective Masses in CuInSe$_2$. *Phys. Status Solidi A* **108,** 483–487 (1981).

200.   Wasim, S. M. Transport Properties of CuInSe$_2$. *Solar Cells* **16,** 289–316 (1986).

201.   Gorley, P. *et al.* Electron Properties of n- and p-CuInSe$_2$. *Solar Energy* **82,** 100–105 (2008).

202.   Essaleh, L., Wasim, S. M. & Galibert, J. Effect of Impurity Band Conduction on the Electrical Characteristics of N-Type CuInSe$_2$. *J. Appl. Phys.* **90,** 3993–3997 (2001).

203.   Wasim, S. M. & Noguera, A. Transport Properties of N-type CuInSe$_2$. *Phys. Status Solidi A* **82,** 553–559 (1984).

204.   Irie, T., Endo, S. & Kimura, S. Electrical Properties of P- and N-Type CuInSe$_2$ Single Crystals. *Japanese Journal of Applied Physics* **18,** 1303–1310 (1979).

205.   Essaleh, L., Wasim, S. M. & Galibert, J. Hall Coefficient and Hall Mobility in the Variable Range Hopping Conduction Regime in N-Type CuInSe$_2$. *Mater. Lett.* **60,** 1947–1949 (2006).

206.   Essaleh, L. *et al.* Hopping Conduction in Copper Indium Diselenide. *Philos. Mag.* **65,** 843–848 (1992).

207.   Persson, C. & Zunger, A. Compositionally Induced Valence-Band Offset at the Grain Boundary of Polycrystalline Chalcopyrites Creates a Hole Barrier. *Appl. Phys. Lett.* **87,** (2005).

208.   Persson, C. & Zunger, A. Anomalous Grain Boundary Physics in Polycrystalline CuInSe$_2$: The Existence of a Hole Barrier. *Phys. Rev. Lett.* **91,** (2003).

209.   Siebentritt, S. *et al.* Evidence for a Neutral Grain-Boundary Barrier in Chalcopyrites. *Phys. Rev. Lett.* **97,** (2006).

210.   Hasan, S. M. F., Subhan, M. A. & Mannan, K. M. The Optical and Electrical Properties of Copper Indium Di-Selenide Thin Films. *Opt. Mater.* **14,** 329–336 (2000).

211.   Sanyal, I., Chattopadhyay, K. K., Chaudhuri, S. & Pal, A. K. Grain Boundary Scattering in CuInSe$_2$ Films. *J. Appl. Phys.* **70,** 841 (1991).

212.   Tang, Y., Braunstein, R. & von Roedern, B. Determination of Drift Mobility and Lifetime for Dominant Charge Carriers in Polycrystalline CuInSe$_2$ by Photomixing. *Appl. Phys. Lett.* **63,** 2393 (1993).

213.   Pal, R., Chattopadhyay, K., Chaudhuri, S. & Pal, A. Photoconductivity in CuInSe$_2$ Films. *Sol. Energy Mater. Sol. Cells* **33,** 241–251 (1994).

214.   Abo El Soud, A. M., Zayed, H. A. & Soliman, L. I. Transport Properties of CuInS$_2$, CuInSe$_2$ and CuInTe$_2$ thin films. *Thin Solid Films* **229,** 232–236 (1993).

215.   Dinca, S. A. *et al.* Hole Drift Mobility Measurements in Polycrystalline CuIn$_{1-x}$Ga$_x$Se$_2$. *Phys. Rev. B* **80,** 235201 (2009).

216.   Dinca, S. A. *et al.* Electron Drift-Mobility Measurements in Polycrystalline CuIn$_{1-x}$Ga$_x$Se$_2$ Solar Cells. *Appl. Phys. Lett.* **100,** 103901–103901–3 (2012).

217.   Anderson, P. W. Absence of Diffusion in Certain Random Lattices. *Phys. Rev.* **109,** 1492–1505 (1958).

218.   Lagendijk, A., van Tiggelen, B. & Wiersma, D. S. Fifty Years of Anderson Localization. *Phys. Today* **62,** 24–29 (2009).

219.   Shklovskii, B. I. Hopping Conduction in Heavily Doped Semiconductors. *Sov. Phys. Semicond+* **7,** 77–80 (1973).

220.   Levanyuk, A. P. & Osipov, V. V. Theory of Luminescence of Heavily Doped Compensated Nondegenerate Semiconductors. *Sov. Phys. Semicond+* **7,** 727–733 (1973).

221.   Metzger, W. *et al.* Recombination Kinetics and Stability in Polycrystalline Cu(In,Ga)Se$_2$ Solar Cells. *Thin Solid Films* **517,** 2360–2364 (2009).

222. Metzger, W. K., Repins, I. L. & Contreras, M. A. Long Lifetimes in High-Efficiency Cu(In,Ga)Se$_2$ Solar Cells. *Appl. Phys. Lett.* **93,** 022110–022110–3 (2008).
223. Eisenbarth, T. Identifikation von Defekten und Metastabilitäten in Cu(In,Ga)Se$_2$-Dünnschichtsolarzellen, Dissertation, FU Berlin. (2010).
224. Klenk, R., Menner, R., Cahen, D. & Schock, H. Improvement of Cu(In,Ga)Se$_2$ Based Solar-Cells by Etching the Absorber. *IEEE Phot. Spec. Conf.* 481–486 (1990).
225. In-Su Lehmann, J. Oberflächenpräparation zur Untersuchung von elektronischen Korngrenzeneigenschaften in Cu(In,Ga)Se$_2$, Diplomarbeit, FU Berlin. (2010).
226. Stolt, L. *et al.* ZnO/CdS/CuInSe$_2$ Thin-Film Solar Cells with Improved Performance. *Appl. Phys. Lett.* **62,** 597–599 (1993).
227. Amatuni, A. N. & Shevchenko, E. B. Linear Thermal Expansion of Monocrystalline Quartz and Aluminum Oxide. *Meas. Tech.+* 1256–& (1966).
228. Mi-Tang, W. & Jin-shu, C. Viscosity and Thermal Expansion of Rare Earth Containing Soda–Lime–Silicate Glass. *J. Alloy Compd.* **504,** 273–276 (2010).
229. Ohnesorge, B. *et al.* Minority-Carrier Lifetime and Efficiency of Cu(In,Ga)Se$_2$ Solar Cells. *Appl. Phys. Lett.* **73,** 1224–1226 (1998).
230. Wagner, M. *et al.* Characterization of CuIn(Ga)Se$_2$ Thin Films - I. Cu-Rich Layers. *Phys. Status Solidi A* **167,** 131–142 (1998).
231. Niki, S. *et al.* Sharp Optical-Emission from CuInSe$_2$ Thin-Films Grown by Molecular-Beam Epitaxy. *Jpn. J. Appl. Phys. Part 2 - Lett.* **33,** L500–L502 (1994).
232. Mudryi, A. V. *et al.* Optical Characterisation of High-Quality CuInSe$_2$ Thin Films Synthesised by Two-Stage Selenisation Process. *Thin Solid Films* **431–432,** 193–196 (2003).
233. Zott, S., Leo, K., Ruckh, M. & Schock, H.-W. Radiative Recombination inCuInSe$_2$ Thin Films. *J. Appl. Phys.* **82,** 356–367 (1997).
234. Schön, J. H., Alberts, V. & Bucher, E. Sharp Optical Emissions from Cu-Rich, Polycrystalline CuInSe$_2$ Thin Films. *J. Appl. Phys.* **81,** 2799–2802 (1997).
235. Siebentritt, S., Rega, N., Zajogin, A. & Lux-Steiner, M. C. Do We Really Need Another PL Study of CuInSe$_2$? *Phys. Status Solidi C* (2004).
236. Siebentritt, S. & Rau, U. *Wide-Gap Chalcopyrites*. (Springer, 2006).
237. Gil, B., Felbacq, D. & Chichibu, S. F. Exciton Binding Energies in Chalcopyrite Semiconductors. *Phys. Rev. B* **85,** 075205 (2012).
238. Lampert, M. A. Mobile and Immobile Effective-Mass-Particle Complexes in Nonmetallic Solids. *Phys. Rev. Lett.* **1,** 450–453 (1958).
239. Haynes, J. R. Experimental Proof of the Existence of a New Electronic Complex in Silicon. *Phys. Rev. Lett.* **4,** 361–363 (1960).
240. Rincón, C., Hernández, E., Wasim, S. M. & Molina, I. Temperature Dependence of the Fundamental Absorption Edge in P-Type CuInSe$_2$. *J. Phys. Chem. Solids* **59,** 1015–1019 (1998).
241. Fan, H. Y. Temperature Dependence of the Energy Gap in Semiconductors. *Phys. Rev.* **82,** 900–905 (1951).
242. Shah, J. *Ultrafast Spectroscopy of Semiconductors and Semiconductor Nanostructures*. (Springer, 1999).
243. Lax, M. Cascade Capture of Electrons in Solids. *Phys. Rev.* **119,** 1502–1523 (1960).
244. Henry, C. H. & Lang, D. V. Nonradiative Capture and Recombination by Multiphonon Emission in GaAs and GaP. *Phys. Rev. B* **15,** 989–1016 (1977).
245. Lang, D. V. & Logan, R. A. Large-Lattice-Relaxation Model for Persistent Photoconductivity in Compound Semiconductors. *Phys. Rev. Lett.* **39,** 635–639 (1977).
246. Cojocaru-Mirédin, O., Choi, P., Wuerz, R. & Raabe, D. Atomic-Scale Distribution of Impurities in CuInSe$_2$-Based Thin-Film Solar Cells. *Ultramicroscopy* **111,** 552–556 (2011).

247.   Zunger, A. New Insights on Chalcopyrites from Solid-State Theory. *Thin Solid Films* **515,** 6160–6162 (2007).

248.   Fekete, L. *et al.* Ultrafast Carrier Dynamics in Microcrystalline Silicon Probed by Time-Resolved Terahertz Spectroscopy. *Phys. Rev. B* **79,** (2009).

249.   Kadlec, F., Kadlec, C. & Kužel, P. Contrast in Terahertz Conductivity of Phase-Change Materials. *Sol. Stat. Comm.* **152,** 852–855 (2012).

250.   Zhang, S. B. & Northrup, J. E. Chemical Potential Dependence of Defect Formation Energies in GaAs: Application to Ga Self-Diffusion. *Phys. Rev. Lett.* **67,** 2339–2342 (1991).

251.   Yella, A. *et al.* Porphyrin-Sensitized Solar Cells with Cobalt (II/III)–Based Redox Electrolyte Exceed 12 Percent Efficiency. *Science* **334,** 629–634 (2011).

252.   Born, M. & Wolf, E. *Principles of Optics.* (Cambridge University Press, 2002).

253.   Fließbach, T. *Statistische Physik.* (Spektrum Akademischer Verlag, 2010).

Abstract

This work investigates the charge carrier dynamics in three different technological approaches within the class of thin film solar cells: radial heterojunctions, the dye solar cell, and microcrystalline $CuInSe_2$, focusing on charge transport and separation at the electrode, and the relaxation of photogenerated charge carriers due to recombination and energy dissipation to the phonon system. This work relies mostly on optical-pump terahertz-probe (OPTP) spectroscopy, followed by transient absorption (TA) and two-photon photoemission (2PPE).

The charge separation in ZnO-electrode/In_2S_3-absorber core/shell nanorods, which represent a model system of a radial heterojunction, is analyzed by OPTP. It is concluded, that the dynamics in the absorber are determined by multiple trapping, which leads to a dispersive charge transport to the electrode that lasts over hundreds of picoseconds. The high trap density on the order of $10^{19}/cm^3$ is detrimental for the injection yield, which exhibits a decrease with increasing shell thickness.

The heterogeneous electron transfer from a series of model dyes into ZnO proceeds on a timescale of 200 fs. However, the photoconductivity builds up just on a 2-10 ps timescale, and 2PPE reveals that injected electrons are meanwhile localized spatially and energetically at the interface. It is concluded that the injection proceeds through adsorbate induced interface states. This is an important result because the back reaction from long lived interface states can be expected to be much faster than from bulk states.

While the charge transport in stoichiometric $CuInSe_2$ thin films is indicative of free charge carriers, $CuInSe_2$ with a solar cell grade composition (Cu-poor) exhibits signs of carrier localization. This detrimental effect is attributed to a high density of charged defects and a high degree of compensation, which together create a spatially fluctuating potential that inhibits charge transport. On the other hand, the charge carrier lifetime in Cu-poor CIS is orders of magnitude higher as in stoichiometric CIS. This is explained by assuming that the Cu_{In} antisite is the most effective recombination center.

Kurz-Zusammenfassung

In dieser Arbeit wird die Ladungsträgerdynamik in drei verschiedenen technologischen Ansätzen aus der Klasse der Dünnschicht-Solarzellen untersucht: Radiale Heteroverbindungen, die Farbstoffsolarzelle und mikrokristallines $CuInSe_2$. Der Fokus liegt dabei auf Ladungsträger-Transport und –Trennung an der Elektrode, sowie der Relaxierung von photogenerierten Ladungsträgern aufgrund von Rekombination und Energieabgabe an die Phononen. Die Arbeit basiert hauptsächlich auf ‚Optical-Pump Terahertz-Probe' (OPTP) Spektroskopie, gefolgt von transienter Absorption (TA) und Zwei-Photonen Photoemission (2PPE).

Die Ladungstrennung in ZnO-Elektrode/In_2S_3-Absorber Kern/Mantel Nanostäben, ein Modellsystem für radiale Heteroverbindungen, wird mittels OPTP analysiert. Es stellt sich heraus, dass die Dynamik im Absorber durch ‚multiple trapping' und dispersiven Ladungstransport zur Elektrode über Hunderte von Pikosekunden bestimmt wird. Die hohe Dichte von flachen Defektzuständen in der Größenordnung von $10^{19}/cm^3$ ist nachteilig für die Injektionsausbeute, die einen Abfall mit ansteigender Manteldicke zeigt.

Der heterogene Elektronentransfer von einer Reihe von Modellfarbstoffen nach ZnO geschieht auf einer Zeitskala von 200 fs. Jedoch bildet sich die Photoleitfähigkeit nur auf einer Zeitskala von 2-10 ps aus und 2PPE zeigt, dass injizierte Elektronen zwischenzeitlich räumlich und zeitlich an der Grenzfläche lokalisiert sind. Daraus lässt sich schließen, dass die Injektion über einen Adsorbat-induzierten Grenzflächenzustand geschieht. Dies ist ein wichtiges Ergebnis im Hinblick auf den Entwurf von Farbstoff-Solarzellen, da zu erwarten ist, dass die Rückreaktion aus langlebigen Grenzflächenzuständen deutlich schneller ist als die aus Volumenzuständen.

Während der Ladungstransport in stöchiometrischen $CuInSe_2$ Dünnschichten durch freie Ladungsträger bestimmt wird, zeigt $CuInSe_2$ mit einer Solarzell-typischen Zusammensetzung Anzeichen von Ladungsträger-Lokalisierung. Dieser nachteilige Effekt wird einer hohen Dichte von geladenen Defekten bei gleichzeitig hoher Kompensierung zugeschrieben, was ein räumlich flukturierendes elektrisches Potential hervorruft, das den Ladungstransport behindert. Demgegenüber ist die Ladungsträgerlebensdauer in Cu-armen CIS um Größenordnungen höher als die in stöchiometrischen CIS. Das wird dadurch erklärt, dass der Cu_{In} Substitutionsdefekt das effektivste Rekombinationszentrum ist.

Publications

Publications that contain parts of the present thesis

C. Strothkämper, K. Schwarzburg, R. Schütz, R. Eichberger, and A. Bartelt *Multiple-Trapping Governed Electron Transport and Charge Separation in ZnO/In2S3 Core/Shell Nanorod Heterojunctions* Journal of Physical Chemistry C **116**, 1165 (2011).

C. Strothkämper, A. Bartelt, P. Sippel, T. Hannappel, R. Schütz, and Rainer Eichberger *Delayed Electron Transfer through Interface States in Hybrid ZnO/Organic-Dye Nano-Structures* submitted to Journal of Physical Chemistry C.

C. Strothkämper, T. Unold, R. Eichberger, C. Kaufmann, and A. Bartelt *Influence of Stoichiometry on Charge Transport and Recombination in CuInSe$_2$* in preparation.

C. Strothkämper, A. Bartelt, R. Eichberger, C. Kaufmann, and T. Unold *Energy and Momentum Relaxation in CuInSe$_2$* in preparation.

Other publications

A. Bartelt, C. Strothkämper, W. Schindler, K. Fostiropoulos, and R. Eichberger *Morphology effects on charge generation and recombination dynamics at ZnPc:C$_{60}$ bulk hetero-junctions using time-resolved terahertz spectroscopy* Applied Physics Letters **99**, 143304 (2011).

R. Eichberger, C. Strothkämper, I. Thomas, T. Hannappel, K. Schwarzburg, C. Fasting, A. Bartelt, and R. Schütz *Charge separation dynamics at inorganic/organic nanostructured hybrid photovoltaic interfaces* Journal of Photonics for Energy **2**, 021003 (2012).

Curriculum Vitae

Der Lebenslauf ist in der Online-Version aus Gründen des Datenschutzes nicht enthalten.

Erklärung zur Dissertation

Ich habe diese Arbeit selbstständig verfasst und nach bestem Wissen alle Hilfen angegeben (vgl. Danksagung). Die Arbeit wurde nicht schon einmal in einem früheren Promotionsverfahren angenommen oder als ungenügend bewertet.

Acknowledgement